

Part II

Proton-proton data at 2.2GeV

In this part of this thesis the analysis procedure of the proton-proton data, and the discussion of obtained results are presented.

The first proton-proton production run was taken in January 2004. During this run a proton beam of 2.2 GeV kinetic energy with an intensity of around 10^7 particles per second was hitting the liquid hydrogen target of 5cm length. The main goal of the experiment was to investigate η meson production and its decay via two electromagnetic decay channels, $\eta \rightarrow \pi^+\pi^-\pi^0$ and $\eta \rightarrow e^+e^-\gamma$, the branching ratios of which are well known. It was also foreseen to collect data on elastic proton-proton scattering in order to investigate the spectrometer in terms of reconstruction resolution and alignment of different detector systems.

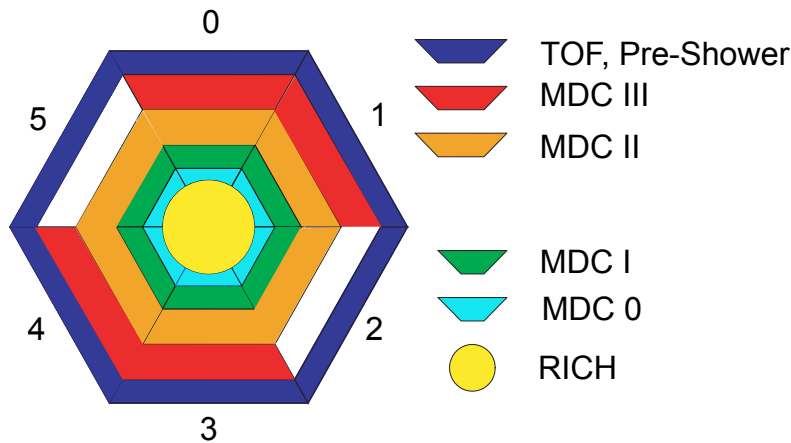


Figure 3.12: Schematic view of participating detector parts during the run. The parts with full colors correspond to operational detectors (some of them are not fully operational, for details see text), while white boxes show the missing detectors.

It was the first time when the spectrometer was fully set up in four sectors out of six. In the remaining two sectors there was one missing MDC chamber. Furthermore there were non-operational layers of the existing MDCs as well due to some problems with high voltage; two out of six layers were switched off in MDC0 sector0¹⁸, in MDC0 sector2 one layer was switched off. In sectors 2 and 5 there were only 3 MDCs existing (0,I,II). Furthermore in MDCII sector 2 two layers were switched off. Therefore the reconstruction of outer segments in this sector were made using information only from four layers which led to not fitted segments from this sector (See section 3.4). Hence the reconstruction resolution from this sector is much worse (As it is shown in the next chapter) and the background contribution is higher. In addition, during the experimental run there were several broken motherboards of MDCs which also affected the reconstruction resolution.

¹⁸In this thesis, the counting of detector parts starts from 0 in accordance with the analysis software.

The schematic picture of participating detectors during this run is shown in Figure 3.12. All the operational sub detectors are indicated with full color, while the missing parts are indicated with white boxes.

In order to enhance the reaction of interest, several 1 level trigger schemes were used for proton-proton elastic and the η decay processes. The main feature for enhancing the events from elastic scattering was the condition coming from kinematics of this process, namely the fact that outgoing protons should be in one plane (complanarity condition). Thus the condition was to require at least two charged particles in the META detectors from opposite sectors.

The first condition for the η meson was to require at least four charged particles in the META detectors, the trigger being called the MULT4 trigger. Additional conditions were set based on simulated data. Simulations show that protons are focused at small polar angles going mainly to the TOFINO detector. So, an additional condition of at least two hits in the TOFINO detector can be applied. The difference in azimuthal angles between the two outgoing protons for both decay channels of the η meson peaks at 180° showing, like in the elastic scattering channel, that the outgoing protons hit mostly opposite sectors. This additional condition on opposite sectors of the META detectors has been used. Summarizing, the 1 level trigger for the η meson reconstruction was based on at least four charged particles in the META detector, two of them being in the TOFINO region, and in addition, the opposite sector condition was required in the META detectors, called MULT4SMART trigger.

To enhance the Dalitz decay of the η meson the second level trigger (LVL2) has been used which selects the events with at least one lepton candidate according to the information from the Image Processing Units.

Not all MULT4SMART triggered events were written to the files. The triggered events were sent to the matching unit board where the decision was taken separately by two different systems which operate independently; the downscaling box and the second level trigger. All second level triggered events were written to file with the corresponding flag stored in the event header. The downscaling box scaled down the events regardless whether they contained lepton pair or not, which are called downscaled events according to the value of downscaling factor which corresponds to the number of events to be discarded between two accepted events. Later in the analysis, according to the information stored in the event header, it was possible to check whether the event was downscaled or not with a corresponding downscaling factor. The analyzed events have to be corrected for this factor in the analysis. More detailed information about downscaling and triggers is given in section 2.5.

This part of the thesis consists of three chapters:

In the first chapter the results from the elastic scattering channel will be presented. At the same time the comparison of different reconstruction methods will be shown as well, using the elastic scattering channel.

In the second chapter the results on exclusive η meson reconstruction from its two

electromagnetic decay channels, $\eta \rightarrow \pi^+\pi^-\pi^0$ and $\eta \rightarrow e^+e^-\gamma$, will be shown. The main emphasis of this analysis will be put on the estimation of the dilepton identification efficiency of the HADES spectrometer, on the investigation of η meson production and on a test of the Vector meson Dominance Model for describing the decays of the mesons.

The third chapter is devoted to the discussions of the results obtained.

Chapter 4

Elastic scattering channel

4.1 Introduction

In general, two body reactions, where two initial particles (a_{01} and a_{02}) do a transition into two final states (a_1 and a_2), are fully described by the 4-momenta of the corresponding particles (p_{01}, p_{02}, p_1, p_2), and the probability of transition can only depend on those momenta.

$$a_{01} + a_{02} \rightarrow a_1 + a_2 \quad (4.1)$$

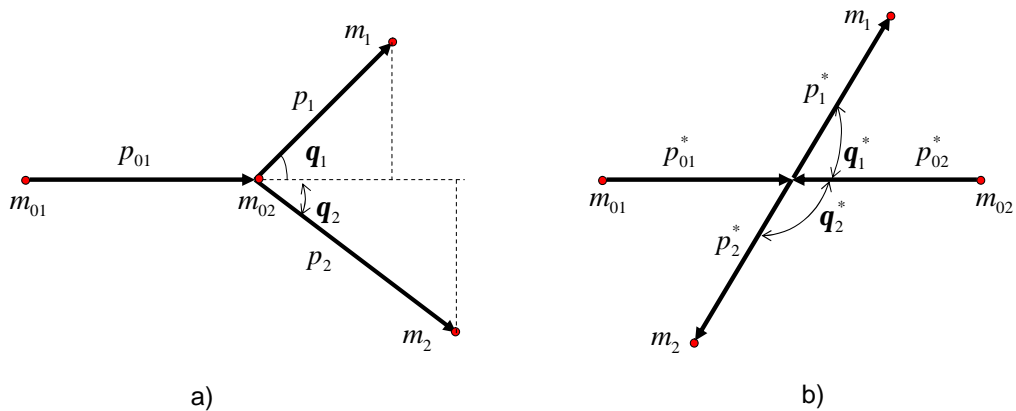


Figure 4.1: Kinematics of elastic scattering in (a) LAB system and (b) center-of-mass system of protons.

Since a transition probability is itself an invariant quantity we should take only invariant combinations made of the above-mentioned 4 momenta. From four 4-momenta one can construct 10 invariant quantities; four of them being squares of the momenta which can be

fixed as they are just masses of the particles. The remaining six parameters are reduced to two by imposing four energy-momentum conservation laws, therefore two body processes are fully described by two independent variables. One can choose these variables to be e.g. the momentum of the incoming particle and the polar angle of one of the outgoing particles.

Using kinematics of elastic scattering (see appendix B) one can obtain a tracking resolution from experimental data and test the alignment of the detector systems.

One should mention that in kinematic calculations sometimes it is convenient to represent the reaction 4.1 as going in two steps; creation and later decay of some compound particle a_0 :

$$a_{01} + a_{02} \rightarrow a_0 \rightarrow a_1 + a_2 \quad (4.2)$$

It is clear that a compound particle is at rest in the CM frame with its mass being equal to \sqrt{s} . The advantage of this notation is that it describes both the two-body decays (in this case $\sqrt{s} = E_{CM} = M$ is the total energy in the CM frame or effective mass) and the decay of unstable particle or a resonance into two particles (in this case $\sqrt{s} = m^0$ is the mass of a decaying particle with γ_{cm} being its Lorentz factor).

4.2 Results from elastic scattering

The analysis of the elastic scattering channel is started with a reaction selection based on the kinematics of the elastic scattering which imposes a restriction on polar and azimuthal angles of the outgoing protons ¹; as it is shown in Appendix B, in order to fulfill the momentum conservation, the momentum vectors of two outgoing protons should be in the same plane. Thus the distribution of the absolute value of the azimuthal angle differences should be centered at 180° as shown in Figure 4.2(a) (integrated over all sectors). As a first selection criterium the 3 sigma cut around this peak, which is fitted with a Gauss distribution, is applied. Another restriction on the polar angles can also be extracted from the kinematics of elastic scattering; the product of tangents of the polar angles of two outgoing protons should be equal to the inverse squared γ_{cm} of the center-of-mass system with respect to the laboratory system.

$$\tan \theta_1 * \tan \theta_2 = \frac{1}{\gamma_{cm}^2} \quad (4.3)$$

where γ_{cm} is the Lorentz factor of the center-of-mass system with respect to the laboratory system defined as:

$$\gamma_{cm} = \sqrt{\frac{E_{01} + m}{2m}} \quad (4.4)$$

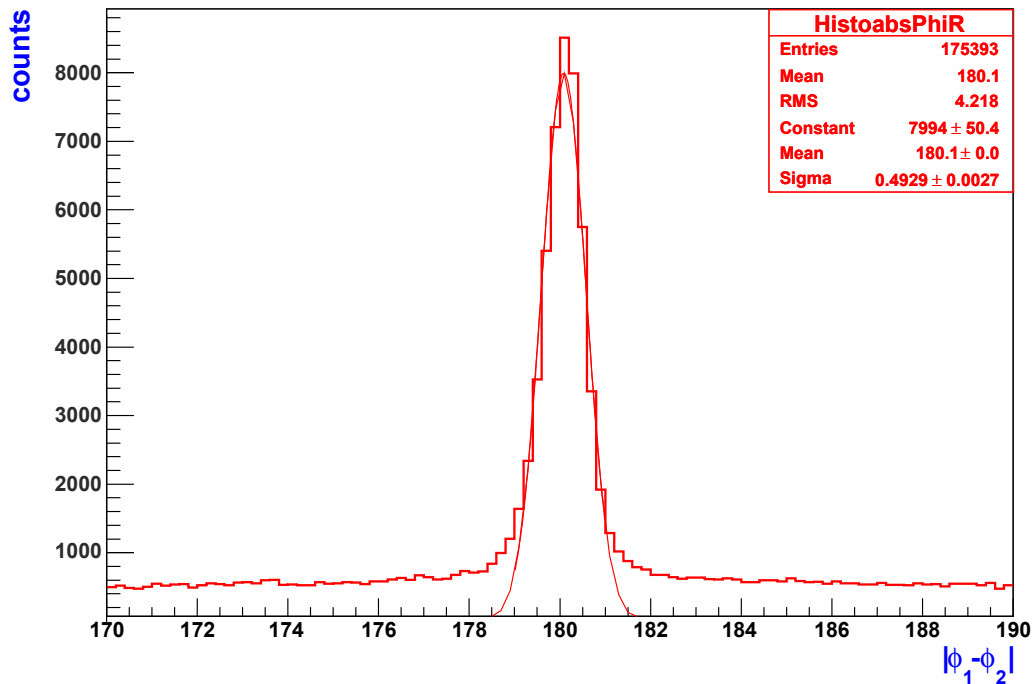
¹Only the events with opposite sector trigger have been used for elastic analysis.

with E_{01} being the total energy of the incoming proton and m stands for its mass.

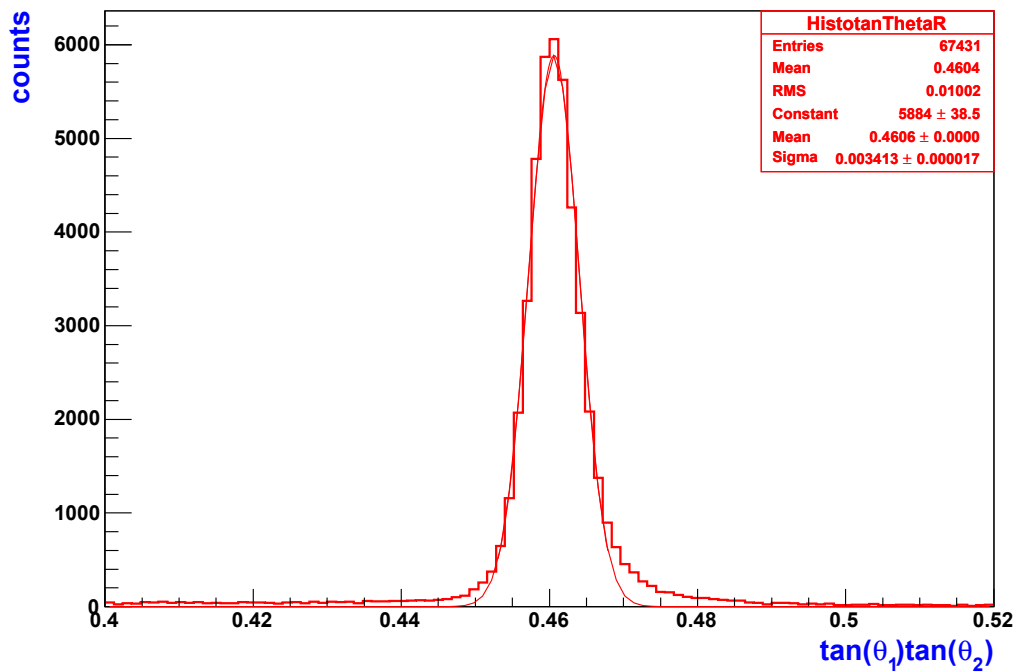
Having the beam kinetic energy of 2.2 GeV the γ_{cm} calculated with formula 4.4 equals 1.4739; therefore $1/\gamma_{cm}^2=0.4603$. The distribution of tangent product of two outgoing protons integrated over all sectors is shown in Figure 4.2(b) which is centered at the calculated value of $1/\gamma_{cm}^2$.² In order to look on how the applied cuts select the elastic scattering channel, the distribution of azimuthal angle of one proton as a function of the azimuthal angle of the second proton is plotted in Figure 4.3(a) after applying the cuts discussed before, while Figure 4.3(b) shows the reconstructed energy of one of the protons in the center-of-mass system of two protons as a function of the center-of-mass energy of the second proton. Both distributions show that the selection of elastic scattering channel is quite good. The value of the center-of-mass energy of each proton should be equal to half of the total center-of-mass energy of two protons, which is just the invariant mass of two protons being equal to 2765.83 MeV, at beam kinetic energy of 2.2 GeV.

In order to investigate possible systematics due to a misalignment of the MDC chambers, the distributions of polar and azimuthal angles are plotted for each pairs of sectors separately in Figures 4.4 and 4.5, where the green distribution is obtained using directly the values from track fitting, while the red distributions are obtained after applying the Runge Kutta algorithm for momentum reconstruction which modifies the angles as well. Systematic deviations can be seen in all pairs of sectors, both for the track fitting and after application of the Runge Kutta method, but in all sectors there is an improvement of widths with respect to the track fitting after application of the Runge Kutta method. The main discrepancy between track fitting and Runge Kutta method is for sector pairs 0-3, as is seen from Figures 4.4 and 4.5, which is mainly connected to the fact that in this sectors there were several not-operational layers of MDCs. In sectors 1-4 the distributions are systematically shifted, both for Runge Kutta and track fitting, while the widths of the distributions are improved for the Runge Kutta case.

²note that this distribution is plotted after applying a cut of 3 sigma around the peak in the distribution of the differences of absolute values of the azimuthal angles of the two protons.

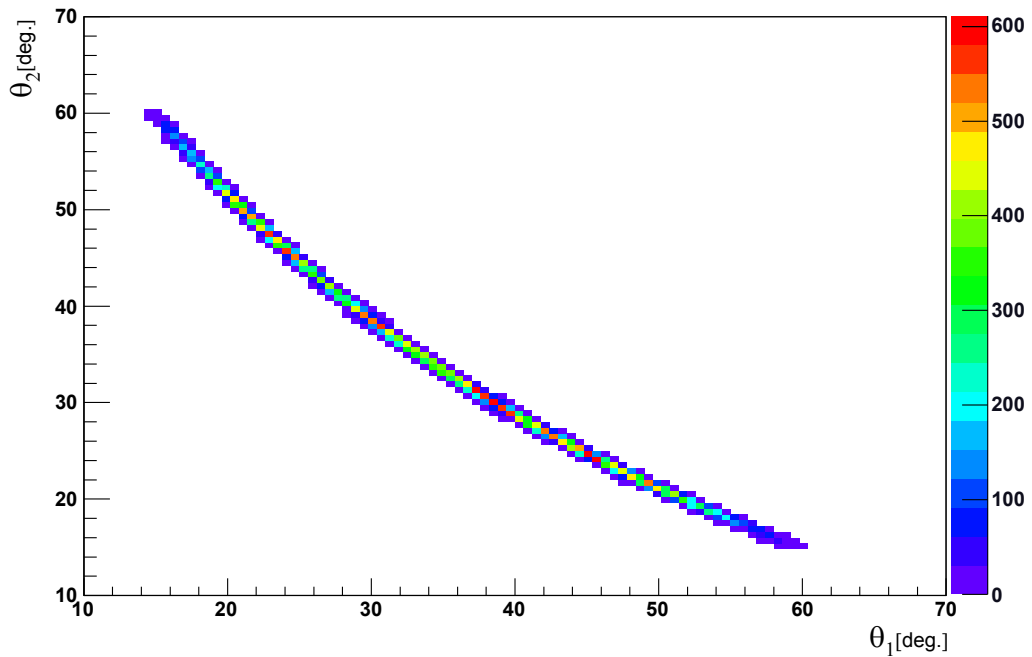


(a) Distribution of the absolute value of azimuthal angle differences of the outgoing protons

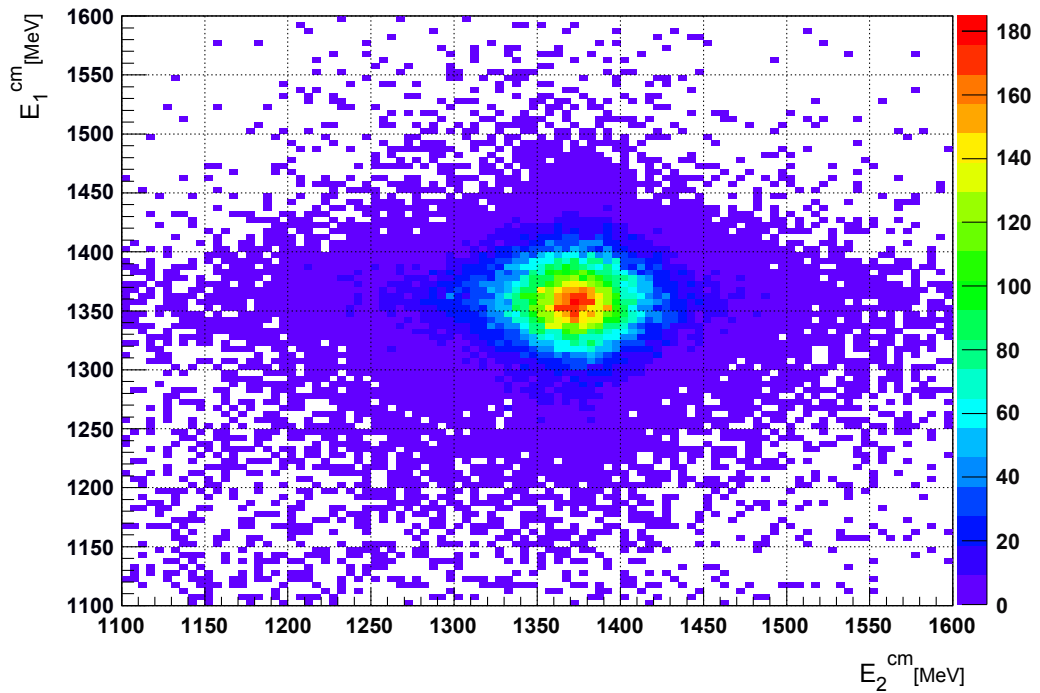


(b) the distribution of products of tangents of polar angles of two outgoing protons

Figure 4.2: The distributions used to select the elastic scattering channel. $3 * \sigma$ cuts around peaks in (a) and (b) have been used.



(a) The polar angle of one of the outgoing protons as a function of another one



(b) Center of mass energy of one of the outgoing protons as a function of another one. Both protons should have the same values of the energy being equal to the half of the total center of mass energy

Figure 4.3: The distributions showing the quality of elastic channel selection.

For the sectors with 3 MDC chambers (2-5) there is no improvement after application of the Runge Kutta method and both distributions are systematically shifted (See Figure 4.5).

The width and the systematic shift of angular distributions will affect the momentum resolution as well; as the spline method uses the angular information from the track fitter, the systematic shifts as well as the broad width of the angular distributions from track fitting will affect the reconstructed momentum in terms of resolution and systematic shifts as well.

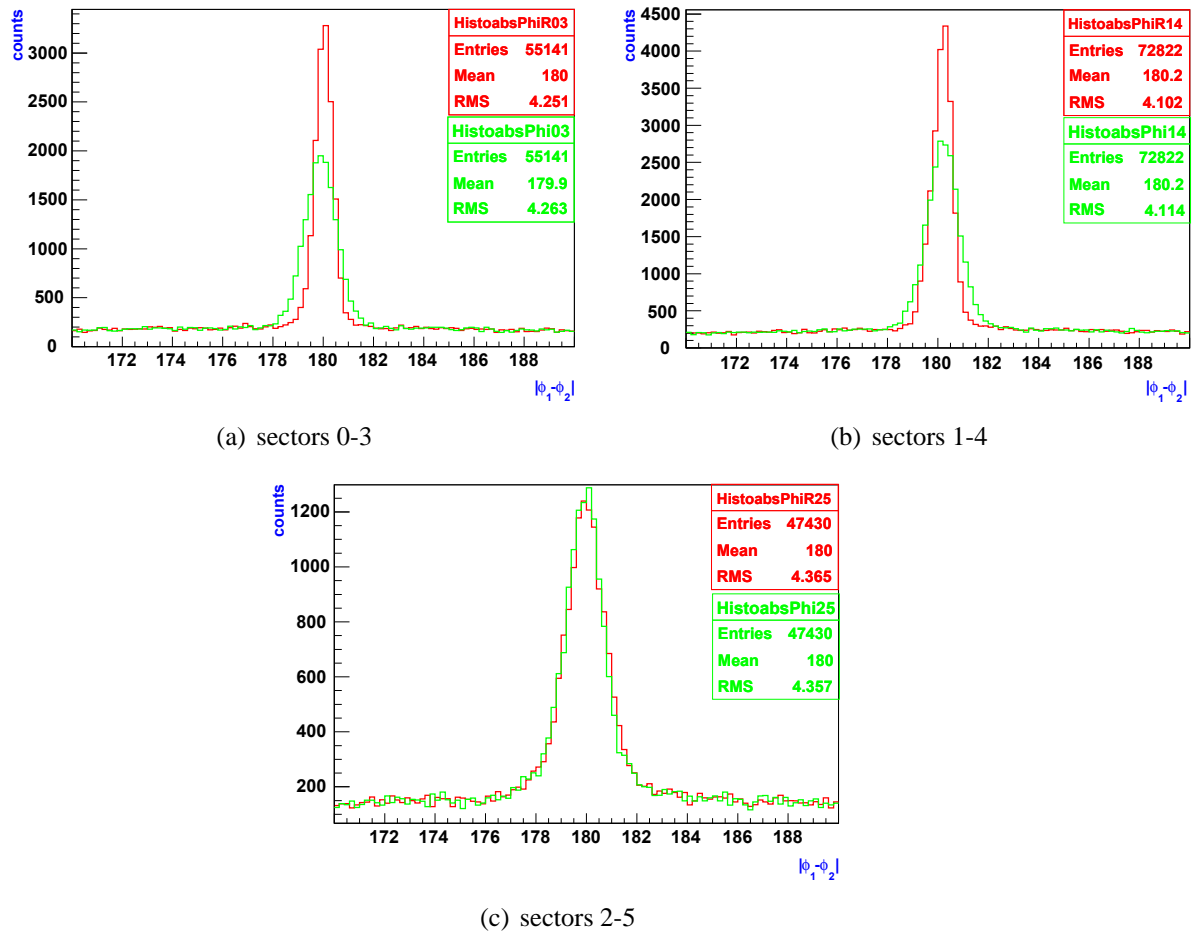


Figure 4.4: Distribution of the absolute value of azimuthal angle differences of protons for each pair of opposite sectors.

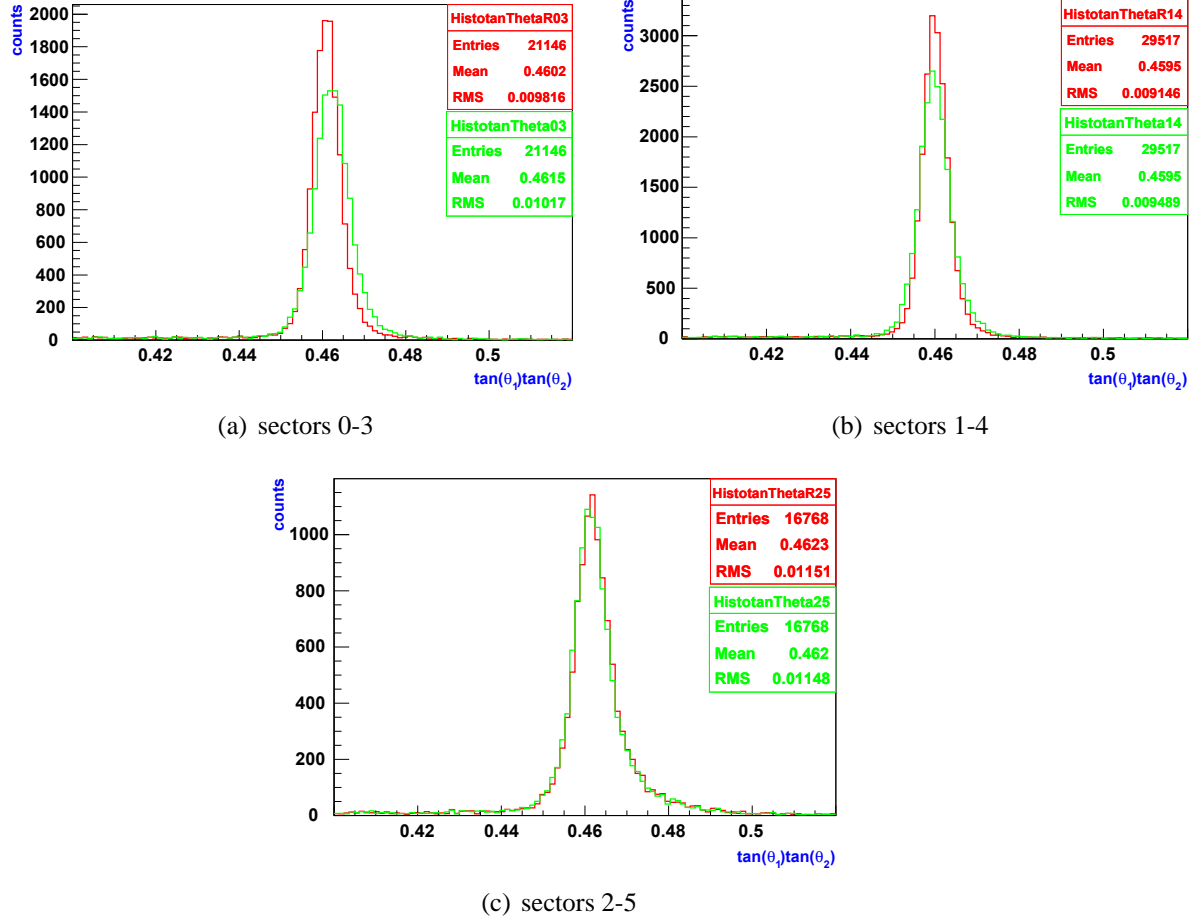


Figure 4.5: Distribution of polar angle products of two protons for each pair of opposite sectors.

The momentum of the track in elastic scattering can be calculated by measuring the polar angle of the track by:

$$p_{\text{calculated}} = \frac{p_{\text{beam}}}{\cos(\theta) [1 + \tan^2(\theta) \gamma_{cm}^2]} \quad (4.5)$$

with γ_{cm} defined in formula 4.4

Figure 4.6 shows the resolution of the momentum reconstruction for each sector defined as:

$$\text{resolution} = \frac{\frac{1}{p_{\text{reconstructed}}} - \frac{1}{p_{\text{calculated}}}}{\frac{1}{p_{\text{calculated}}}} \quad (4.6)$$

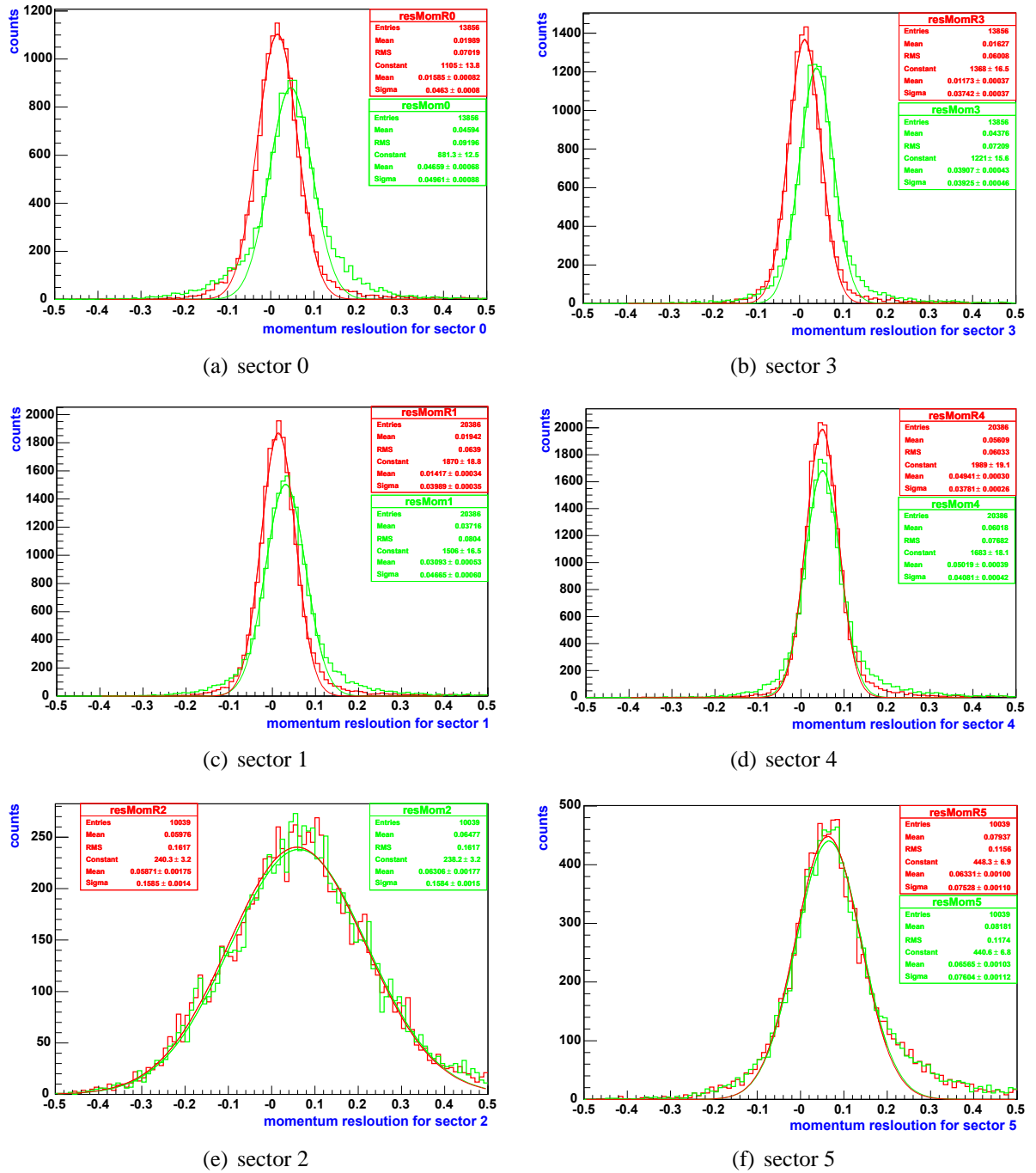


Figure 4.6: The momentum resolution obtained for each sector using elastic scattering for spline(green) and Runge Kutta (red) methods. The resolution is defined as

$$\frac{\frac{1}{P_{\text{reconstructed}}} - \frac{1}{P_{\text{calculated}}}}{\frac{1}{P_{\text{calculated}}}}$$

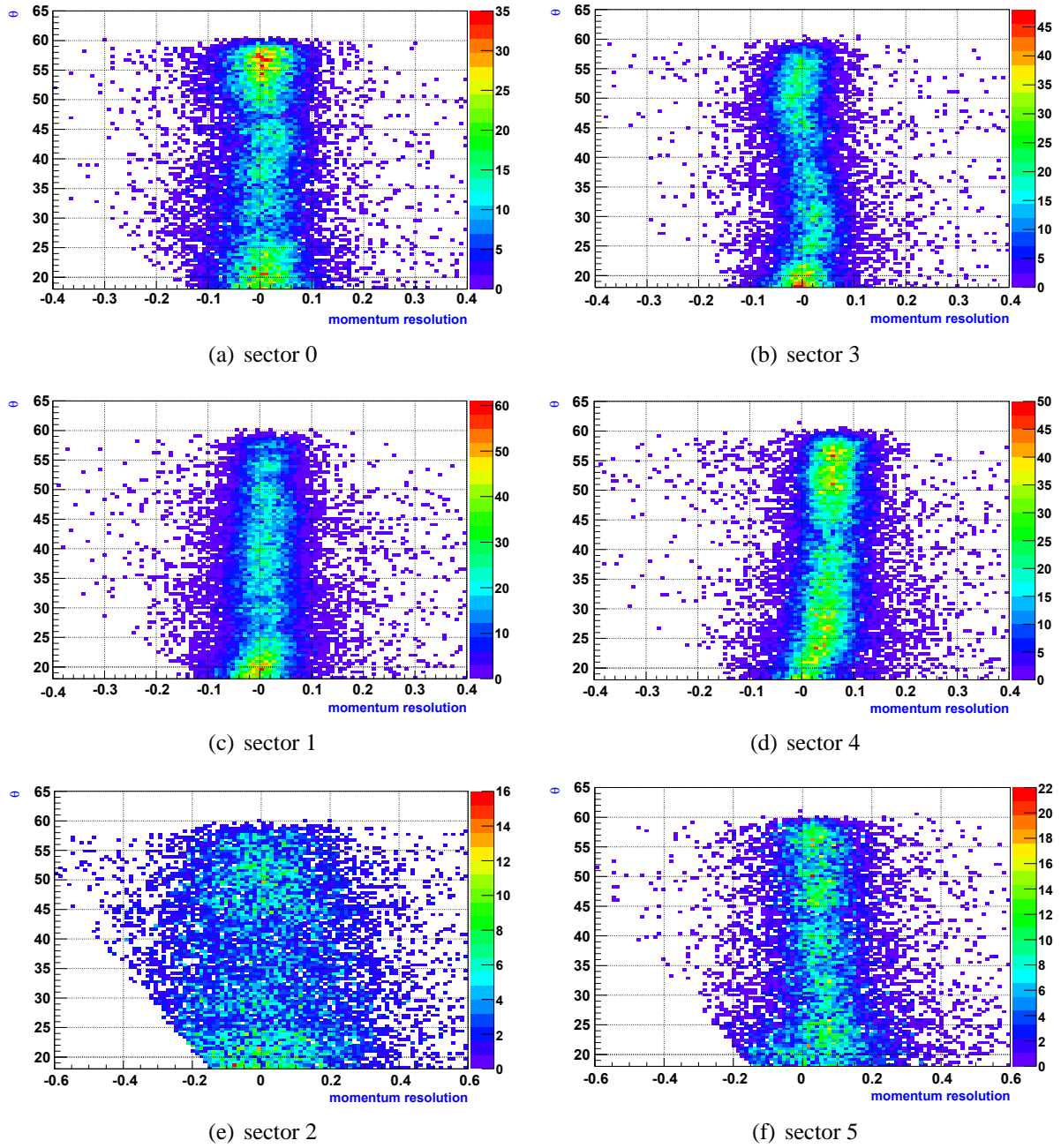


Figure 4.7: The momentum resolution as a function of polar angle obtained for each sector using elastic scattering for the Runge Kutta method. The resolution is defined as

$$\frac{1}{p_{\text{calculated}}} \frac{p_{\text{preconstructed}} - p_{\text{calculated}}}{p_{\text{calculated}}}$$

Tables 4.1 and 4.2 summarizes the obtained momentum reconstruction resolutions and systematic shifts from the spline and Runge Kutta methods ³.

momentum reconstruction resolutions σ [%]						
	sector 0	sector 1	sector 2	sector 3	sector 4	sector 5
spline	5	4.7	16	3.9	4	7.6
Runge Kutta	4.6	4	16	3.7	3.8	7.6

Table 4.1: Momentum resolution from spline and Runge Kutta, obtained for each sector using elastic scattering.

systematic shifts in momentum reconstructions [%]						
	sector 0	sector 1	sector 2	sector 3	sector 4	sector 5
spline	4.6	3	6.3	3.9	5	6.5
Runge Kutta	1.6	1.4	6.3	1.1	5	6.5

Table 4.2: Systematic shifts in momentum reconstruction for spline and Runge Kutta for each sector.

The observed large systematic shift for the spline is connected to the systematic shift for angles plotted in Figures 4.4 and 4.5. In sector 4 there is a systematic shift of 5%, both for spline and Runge Kutta methods correlated with the systematic shifts of angles which is not improved for Runge Kutta method as well (Figures 4.4 and 4.5).

For the sectors with 3 MDC chambers there is no improvement after applying a Runge Kutta method. The overall systematic shift of the momentum resolution is partly connected with the fact that the reconstructed momenta are not corrected for energy loss. It is clear that the obtained resolution is not pure momentum resolution but is affected with angular resolution as well since the theoretical momentum is calculated by measuring a polar angle.

Figure 4.7 shows the momentum resolution as a function of polar angles for each sector.

As it is seen from the distributions for momentum resolutions (Figures 4.6 and 4.7) there are still some problems connected to probably with misalignment, as it depends on sectors.

³It should be noted that all momentum resolutions are plotted for the momentum regions below 2.5 GeV because of systematic shift in this region of momentum as well as its broadening due to the problems with low polar angles as for the high momentum protons in elastic scattering the corresponding polar angles are small. In general the momentum resolution should be estimated as a function of momentum.

Chapter 5

Exclusive η meson reconstruction

5.0.1 Introduction

In the quark model all mesons are bound states of quark and anti- quark [54, 55, 56]. When we combine two particles with isospin $I = \frac{1}{2}$, we obtain an iso-triplet ¹

$$\begin{aligned} |1 \ 1\rangle &= -u\bar{d} \\ |1 \ 0\rangle &= (u\bar{u} - d\bar{d}) / \sqrt{2} \\ |1 \ -1\rangle &= d\bar{u} \end{aligned} \quad (5.1)$$

and iso-singlet.

$$|00\rangle = (u\bar{u} + d\bar{d}) / \sqrt{2} \quad (5.2)$$

In the language of group theory we can say that u and d quarks form the fundamental representation of SU(2) isospin symmetry [54]. It is a mathematical copy of spin in that the isospin generators satisfy the same algebra like spin. The triplet 5.1 and singlet 5.2 decomposition in this language can be written us:

$$2 \otimes \bar{2} = 3 \oplus 1 \quad (5.3)$$

In case of pseudoscalar mesons (when quarks spins are anti- parallel) the triplet is the pion; for vector mesons (spins are parallel) it is the ρ meson. By combining a third quark s (therefore introducing the second additive quantum number S, in addition to I_3) it was natural to enlarge isospin symmetry to a larger group, namely, a SU(3) group (with rank 2). With the analogy to 5.3 we can decompose now the product of fundamental representation and a conjugate one of SU(3) as a sum of octet and singlet representations [56, 57]:

¹We use a "ket" notation where $|I \ I_3\rangle$ means that the particle is in a state with isospin I and its third component is equal to I_3 . In general the product of two states $|j_1 \ m_1\rangle \times |j_2 \ m_2\rangle$ can be constructed according to $|JM\rangle = \sum \langle j_1 m_1 j_2 m_2 | JM \rangle |j_1 m_1\rangle |j_2 m_2\rangle$ where $\langle j_1 m_1 j_2 m_2 | JM \rangle$ are called Clebsch-Gordan coefficients.

$$3 \otimes \bar{3} = 8 \oplus 1 \quad (5.4)$$

The illustration of the pseudoscalar nonet (an octet plus a singlet) is shown in Figure 5.1

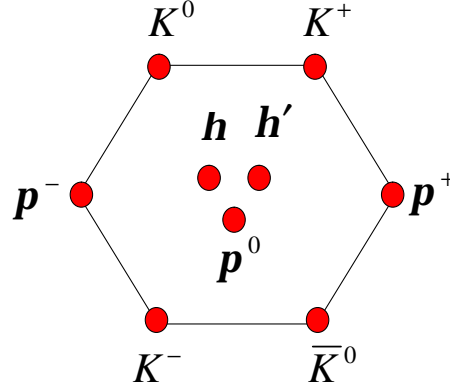


Figure 5.1: A nonet of pseudoscalar mesons.

As we have two isospin 0 states, the iso-singlet combination 5.2 and the $s\bar{s}$, their superposition should correspond to an η_8 and η_0 (or φ_8 and φ_0):

$$\begin{aligned} \eta_8 &= \frac{u\bar{u} + d\bar{d} - 2s\bar{s}}{\sqrt{6}} \\ \eta_0 &= \frac{u\bar{u} + d\bar{d} + s\bar{s}}{\sqrt{3}} \end{aligned} \quad (5.5)$$

where η_8 and η_0 are octet and singlet states.

From the last equation it can be seen that η_0 treats u, d, and s quarks symmetrically and is unaffected under SU(3) transformations while the η_8 transforms as a part of the SU(3) octet whose other members are pions and kaons. As these two states have the same quantum numbers, in practice they tend to mix. In fact the observed pseudoscalar mesons η and η' are linear combinations of the octet and the singlet pseudoscalar η_0 and η_8 states.

$$\begin{aligned} \eta &= \cos(\Theta)\eta_8 - \sin(\Theta)\eta_0 \\ \eta' &= \sin(\Theta)\eta_8 + \cos(\Theta)\eta_0 \end{aligned} \quad (5.6)$$

where the Θ is the mixing angle.

The mixing angle can be calculated using the Gell-Mann-Okubo mass formula for the pseudoscalar meson multiplet [56]

$$m_\eta^2 = \frac{4}{3}m_K^2 - \frac{1}{3}m_\pi^2 \quad (5.7)$$

together with 5.6 which gives $\theta = -11^\circ$. However there are other approaches for calculating this angle giving slightly different values [58, 59, 60]. Consequently the mixing angle is known with low precision and ranges between -10° and -23° .

One should mention that in case of ideal mixing the η meson would consist of non strange quarks only and η' would just be the $s\bar{s}$ combination.²

The η meson has only electromagnetic decay channels, and even not all of them are possible [1]³⁴.

In this chapter the reconstruction procedure of the η meson from its two decay channels $\eta \rightarrow \pi^+\pi^-\pi^0$ and $\eta \rightarrow e^+e^-\gamma$, the branching ratios of which are well known, will be presented.⁵

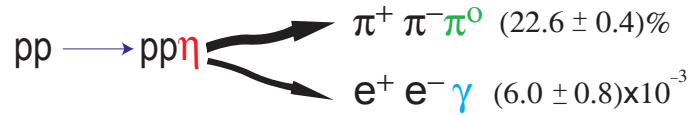


Figure 5.2: Decay channels of the η meson with well known branching ratios studied in this work.

This investigation can schematically be divided into several steps [61]:

- Estimation of the dilepton identification efficiency of the HADES spectrometer.
- Study of the η meson production.

²In case of vector mesons the mixing angle is known more precisely and it is close to ideal mixing, therefore the observed ϕ and ω states are just $s\bar{s}$ and $(u\bar{u}+d\bar{d})/\sqrt{2}$ combinations correspondingly.

³The electromagnetic channel $\eta \rightarrow \pi^0 e^+ e^- (\pi^0 \gamma)$ is forbidden by C parity.

⁴The decay channel $\eta \rightarrow \pi^+\pi^-\pi^0$ could look like strong decay, but it is forbidden by G parity conservation.

⁵Decay modes of the η [$I^G (J^{PC}) = 0^+ (0^{-+})$] meson

decay mode	$\frac{\Gamma_i}{\Gamma}$
2γ	$(39.43 \pm 0.26)\%$
$3 \pi^0$	$(32.51 \pm 0.29)\%$
$\pi^0 2\gamma$	$(7.2 \pm 1.4) \times 10^{-4}$
$\pi^+\pi^-\pi^0$	$(22.6 \pm 0.4)\%$
$\pi^+\pi^-\gamma$	$(4.68 \pm 0.11)\%$
$e^+e^-\gamma$	$(6.0 \pm 0.8) \times 10^{-3}$
$\mu^+\mu^-\gamma$	$(3.1 \pm 0.4) \times 10^{-4}$
e^+e^-	$< 7.7 \times 10^{-5}$
$\mu^+\mu^-$	$(5.8 \pm 0.8) \times 10^{-6}$
$e^+e^-e^+e^-$	$< 6.9 \times 10^{-5}$
$\pi^+\pi^-e^+e^-$	$(4.0_{-2.7}^{+14.0}) \times 10^{-4}$
$\pi^+\pi^-2\gamma$	$< 2.0 \times 10^{-3}$
$\pi^+\pi^-\pi^0\gamma$	$< 5. \times 10^{-4}$
$\pi^0\mu^+\mu^-\gamma$	$< 3. \times 10^{-6}$

- Test of the Vector meson Dominance Model for meson decays.

For the dilepton identification efficiency the following procedure is used:

1. Reconstruction of η mesons from the 3-pion and the Dalitz decays for simulation and experiment, respectively, thus obtaining the numbers: N_{had}^{sim} , N_{Dalitz}^{sim} , N_{had}^{exp} , N_{Dalitz}^{exp} .
2. Having done the first step we can now calculate

$$Ratio = \frac{R_{Exp}}{R_{Sim}} \quad (5.8)$$

where

$$R_{Exp} = \frac{N_{had}^{Exp}}{N_{Dalitz}^{Exp}} \quad (5.9)$$

$$R_{Sim} = \frac{N_{had}^{Sim}}{N_{Dalitz}^{Sim}}$$

are the ratios of reconstructed η mesons from the 3-pion and Dalitz decays correspondingly for experimental data and simulation.

3. From equation 5.8 we can estimate the dilepton identification efficiency of the HADES spectrometer.

Note that we can not directly compare the obtained ratio from experimental data R_{Exp} (Equation 5.9) to the known relative branching ratios. The reason for this is that the branching ratios are obtained in full phase space. Because the two decay channels have a different phase space distribution, they will be cut in different ways inside the HADES acceptance, consequently the relative branching ratios will be different from those listed in Figure 5.2.

In order to investigate the production mechanism of the η meson the reconstructed experimental angular distributions will be compared with those obtained from simulation.

For testing of the Vector meson Dominance Model the reconstructed invariant mass of e^+e^- pairs from the η Dalitz decay will be compared with that obtained from model calculations.

5.1 Meson production in NN collisions

There is a general consensus in theory that in NN collisions the η meson is produced in a two step process, where, in the first stage, pseudoscalar or vector mesons exchanged between the colliding nucleons excites them.

Excited states of the nucleon are called nucleon resonances. States with isospin $I = 3/2$ are called Δ resonances, states with isospin $I = 1/2$ are called N^* states.

The states are characterized in the following nomenclature: $L_{2I2J}(W)$ where L is the orbital angular momentum of the nucleon-pion (or other pseudoscalar meson) pair from the decay of the resonance in spectroscopical notation. I and J are isospin and total angular momentum of the resonance and W stands for its pole mass.

All nucleon resonances can decay to the nucleon ground state via the strong interaction by emission of mesons. The usual spin-isospin selection rules apply, so e.g. the Δ resonance ($I = 3/2$) can decay to the nucleon ground state ($I = 1/2$) via the emission of pions ($I = 1$), but not via the emission of η mesons ($I=0$), while both decays are possible for the S_{11} ($I=1/2$) state.

In the framework of the constituent quark model the simplest excitations of the nucleon are described by a spin-flip or an orbital excitation of one quark. The wave functions are composed of space, spin, flavor and color parts. In the simplest model, the constituent quarks are put in a harmonic oscillator potential with additional spin-spin and spin-orbital dependent interactions. Figure 5.3 shows the ground state of the nucleon in such a model.

The $P_{33}(1232)$ is produced via the parallel alignment of all three quark spins as shown in Figure 5.4(a). This state would be degenerate with the nucleon ground state if only the oscillator potential is considered but the two states are split by the spin-spin interaction. The other resonances arise from the excitation of one quark into the $L = 1$, p shell, as shown in Figure 5.4(b).

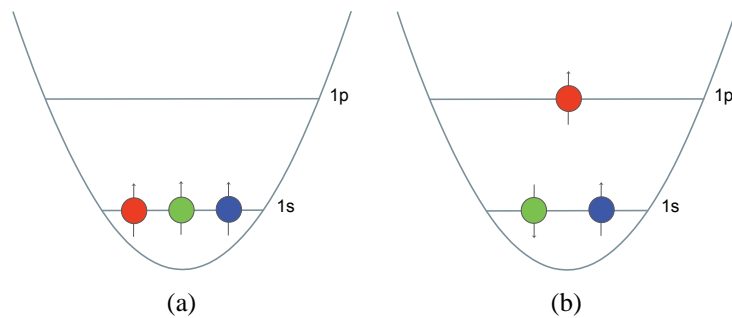


Figure 5.3: Ground state of a nucleon.

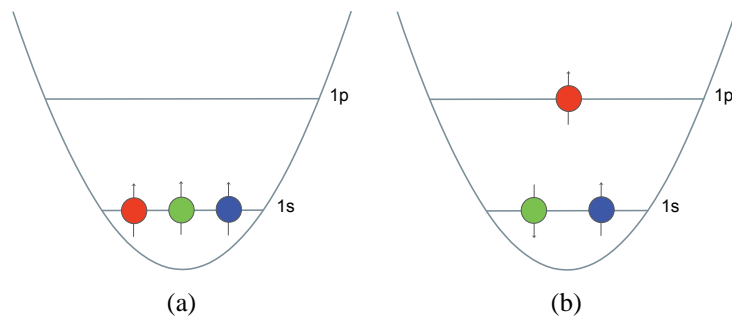


Figure 5.4: Excited state of a nucleon, via spin flip (a) corresponding to P_{33} and orbital excitation (b) corresponding to S_{11} or D_{13} .

The $S_{11}(1535)$ resonance seems to play an important role as an intermediate state for the $pp \rightarrow pp\eta$ reaction [62]. This behavior is not yet understood and gave rise to many discussions about the structure of this state. Apart from the resonance currents, different models take into account the production via other mechanisms like nucleonic currents [63, 64], direct production [65, 66] or mesonic currents [64] (See Figure 5.5).

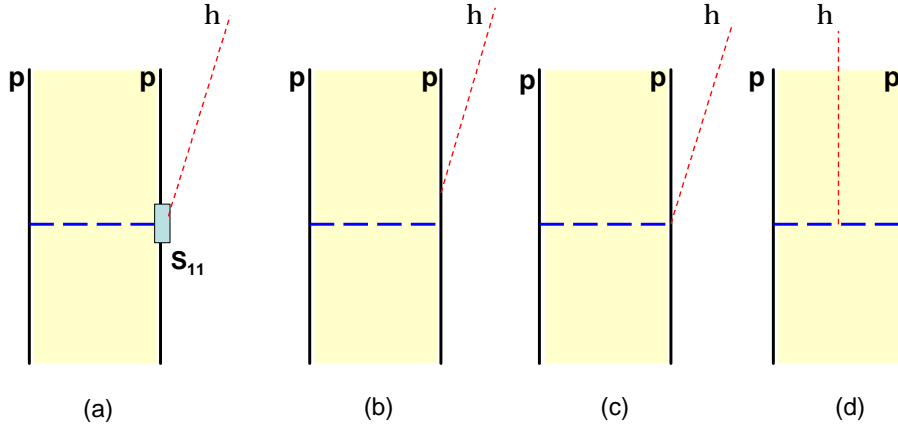


Figure 5.5: Production mechanisms of η mesons in NN collisions a)resonance decay b)hadronic current c)direct decay d)mesonic fusion.

However, there are some ambiguities regarding the particular contribution from the individual mesons. While in the references [67, 68] the largest contribution is due to a virtual ρ meson exchange, the authors of [69] predict the highest amplitude for the π meson exchange.

5.2 Simulation

As was mentioned at the beginning of this chapter, in order to estimate the dilepton identification efficiency of the HADES spectrometer and investigate the production and decay mechanisms of the η mesons we need a simulation. Different types of simulated data have been generated: a full cocktail simulation and simulations containing only η mesons with its subsequent 3-pion or Dalitz decay.

Simulations are an integral part of experimental programs associated with scattering experiments and particle accelerators. Such studies are required both in order to understand the properties of experimental setups, as well as to gain insight into the processes of interest, so that relevant experiments may be optimized and experimental spectra may be interpreted. The simulation procedure starts with an event generation. For proton-proton simulations a full cocktail was generated according to most of the known physical processes using the PLUTO software [70, 71]. PLUTO is a collection of C++ classes, added up to the framework of a simulation package for hadronic-physics reactions. The output can be analyzed online or further processed with HGEANT [72]. The package includes models for resonance and Dalitz decays. A decay-manager interface enables multi-step (cocktail) calculations. The branching ratios and decay channels are set by the user, according to values known from experiment or from theoretical calculations. Table 5.1 shows the processes included for proton proton simulations.

reaction	cross section [μb]
$pp \rightarrow pp$ (elastic)	18.0
$pp \rightarrow n\Delta^{++}$	10.8
$pp \rightarrow p\Delta^+$	3.6
$pp \rightarrow pN(1440)$	2.8
$pp \rightarrow pp\pi^0$	0.15
$pp \rightarrow pn\pi^+$	1.0
$pp \rightarrow p\Delta^+\pi^0$	0.48
$pp \rightarrow n\Delta^{++}\pi^0$	2.0
$pp \rightarrow pN(1440)\pi^0$	2.36
$pp \rightarrow pp\pi^0\pi^0\pi^0$	0.15
$pp \rightarrow p\pi^+\pi^-\pi^0$	0.33
$pp \rightarrow pn\pi^+\pi^+\pi^-$	0.6
$pp \rightarrow pN^*(1535)$ (inclusive)	0.31

Table 5.1: Processes included in cocktail simulation.

For the 3-pion decay of the η meson only phase space production was assumed, while for the Dalitz decay the Vector Dominance Model was used. The production of the η meson was assumed through nucleon excitation to the $N^*(1535)$ state and its subsequent decay to the nucleon with emission of the η meson. For pure η simulations the matrix element of η production measured by the DISTO experiment was taken [10, 11].

After event generation the events are read by the HGeant [72] package based upon the GEANT [73] program from CERN, which tracks the particles through the spectrometer. It is possible to describe the experimental setup by a structure of geometrical volumes and the corresponding material composition. This is implemented in HGeant, which in turn uses it to simulate the different effects affecting particles passing through detector volumes. In the next step Geant hits are digitized i.e. hit positions are converted into observables similar to what is obtained in experimental runs. The hit digitization consists of several algorithms which simulate the electronic response of each detector component, by taking into account resolution smearing, electronic noise, and most of the effects which play a role in the analogue-to-digital conversion procedure. The digitizer's output looks exactly like a calibrated signals from the detector which can be analyzed with the standard algorithms used to analyze experimental data.

5.2.1 Reaction parametrization

In general for the full description of the three particle system after particle identification and four momentum conservation we are left with 5 parameters ($12-4-3=5$). The square of invariant masses of the proton- η system $p_1\eta$ and $p_2\eta$, respectively, (the Dalitz parameters) constitute a natural choice for the study of the interaction within the $pp\eta$ system. This is

because by investigating the population of the surface defined by these two variables one can study the interaction mechanism between those particles.

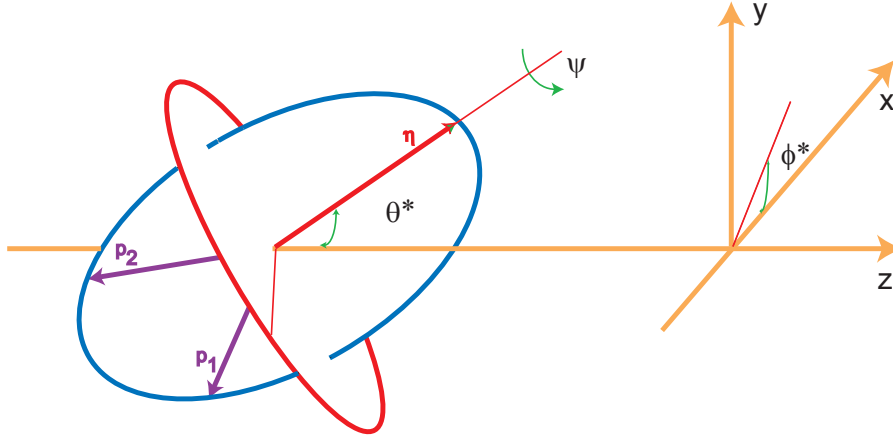


Figure 5.6: Parameters describing η meson production.

Due to the momentum conservation law, the momentum vectors of the particles are lying in one plane, as shown in Figure 5.6, often referred to as the emission, reaction or decay plane. The remaining 3 parameters must define an absolute orientation of the emission plane. This may be realized for example by defining the orientation (θ^*, ϕ^*) for the momentum of the arbitrarily chosen particle in the center-of-mass frame e.g. the η meson and the angle which describes the rotation ψ around the direction fixed by that particle as shown in Figure 5.6.

For our purpose the angles have been chosen as polar and azimuthal angles of the η meson in the center-of-mass frame of protons as shown in Figure 5.6, while the third angle was chosen in a different way describing the orientation of the two proton plane θ_p in the center-off-mass frame of two outgoing protons. Taking into account rotational symmetry of the beam axis one can integrate over the ϕ^* angle and be left with only two angles. It has been checked with simulation that the remaining two angles are almost independent, thus allowing us to compare 1 dimensional distributions without having to create a multi-dimensional acceptance correction.

5.3 Analysis Strategy

The usual way of resonance identification consists of several steps [74]:

- Identification of background events.
- Reconstruction of invariant mass of decay products after excluding the background events.

Because of the fact that we are unable to detect all decay products (there are neutral particles among them) we will follow the indirect way of resonance identification based on the missing-mass distributions.

The reaction channels studied here contained at most one unmeasured particle in the final state, thus measured events with four tracks were kinematically complete. The reconstruction procedure consists of the following steps:

1. Event selection and particle identification.
2. Removal of fake tracks.
3. Reaction selection.

5.3.1 Event selection and particle identification

As a first selection criterium only the events with at least one negative and three positive tracks were taken. In this step every track is marked with the corresponding flags according to a fake removal strategy described in the next section.

The negative particle was assumed to be an e^- if there was a matching with the signal from the *RICH* detector or π^- in the other case. As we do not know beforehand which of the positively charged tracks corresponds to a proton and a π^+ or e^+ , we create different candidates taking each time one of the positively charged tracks to be a π^+ or e^+ as shown in Figure 5.7. In this Figure each row is taken as a candidate for the next analysis steps. The combinations presented in Figure 5.7 correspond to the case when there are exactly three positive and one negative particles. In general, there can be of course more tracks coming from physics processes and fake tracks as well.

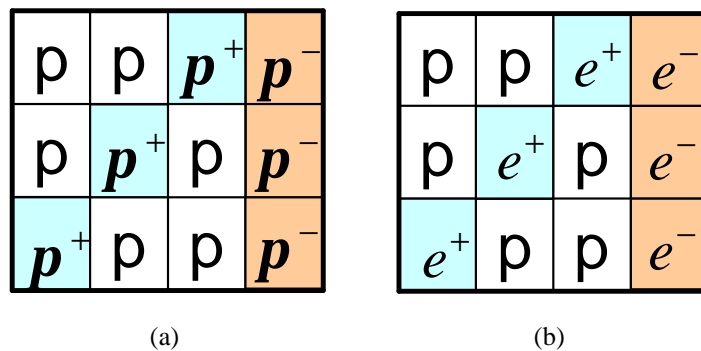


Figure 5.7: Candidates created from an event in the case of exactly 3 positive and one negative particles (a) for the 3 pion final state (negative particle is assumed to be π^-) and (b) for the Dalitz decay (the negative particle is assumed to be e^-).

As it is seen from Figure 5.7, we have created 3 candidates corresponding to each row. Obviously only one of them is correct where the assumption made on particles corresponds to reality. In other words, in order to remove two of the three combinations we need a particle identification.

For hadron identification the correlation between momentum and β of the track was used. The left side of Figure 5.8 shows the momentum times polarity as a function of velocity of a particle in experimental data, for events where the start time was reconstructed from a negative pion ⁶, while the right side shows the same correlation with the negative particle being identified as an electron this time. Each combination created above should fulfill the condition based on graphical cut as shown in Figure 5.8, e.g. for the first candidate from Figure 5.7 the protons and pions should be inside the corresponding graphical cut presented in Figure 5.8, otherwise that candidate is removed from the list. The used cuts are taken quite broad in order not to lose statistics and furthermore the lepton identification was done without imposing conditions on the ring quality in the *RICH* detector and without detecting electromagnetic showers in the *SHOWER* detector. Most of the misidentified particles will be removed by a kinematic condition applied afterwards.

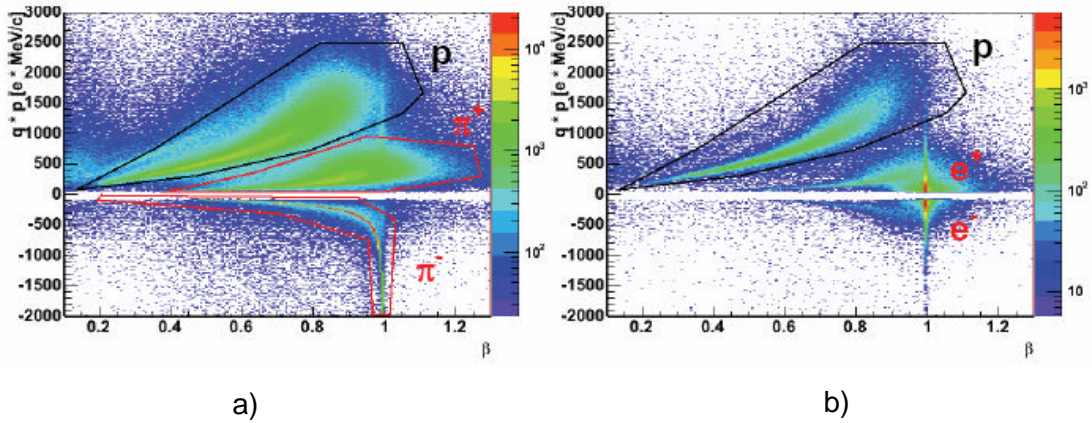


Figure 5.8: Graphical cuts used for particle identification: a) for 3 pion final state and b) for the Dalitz decay of the η meson.

⁶As this data was taken without start detector, the start time of the reaction was reconstructed using an algorithm based on assigning a theoretically calculated time of flight to the identified particle (See Section 2.1).

5.3.2 Removal of fake tracks

Due to the broad matching windows fake tracks can contribute to the list of created tracks which are schematically shown in Figure 5.9.

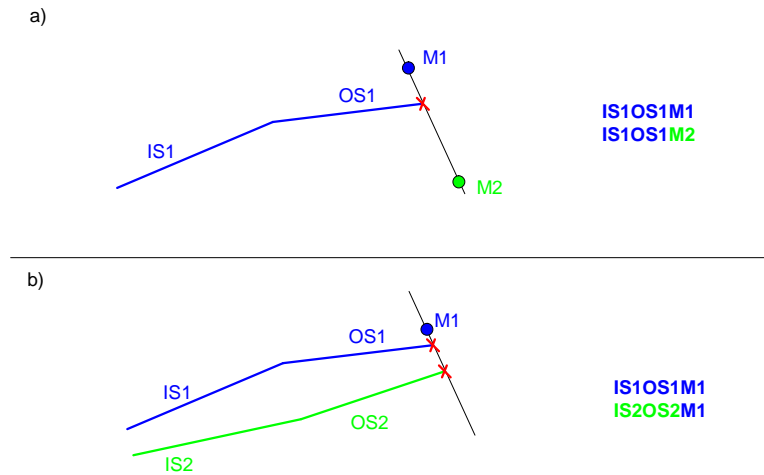


Figure 5.9: Strategy for removing fake META candidates when (a) one track candidate is matched with two different META hits and (b) two track candidates are matched with the same META hit (See text for details).

Examples of the fake candidates:

- a) The same track candidate is matched with two different *META* hits. The blue and green circles are reconstructed *META* hits while the red crossing is the intersection point of the outer track segment with the *META* detector. In this case we have 2 fully reconstructed tracks, denoted as IS1OS1M1 and IS1OS1M2 instead of one. The track which has a minimum matching quality parameter (See section 3.6) is marked as a "good" one, while the other is marked as a "meta fake".
- b) Two different track candidates are matched with the same *META* hit. Like in case (a) the track with the minimum value of the matching quality parameter is marked as a "good" one, while the other is kept with a "meta fake" flag.

Apart from the "meta fakes" described above, there can also be fake tracks coming from mismatching between inner and outer tracks reconstructed in the corresponding MDCs before and after the *MAGNET*. Figure 5.10 schematically shows this phenomenon. These fakes we call "track fakes" and the procedure of selecting the "good" tracks is based on quality parameters, as in case of "meta fakes", describing the corresponding matching.

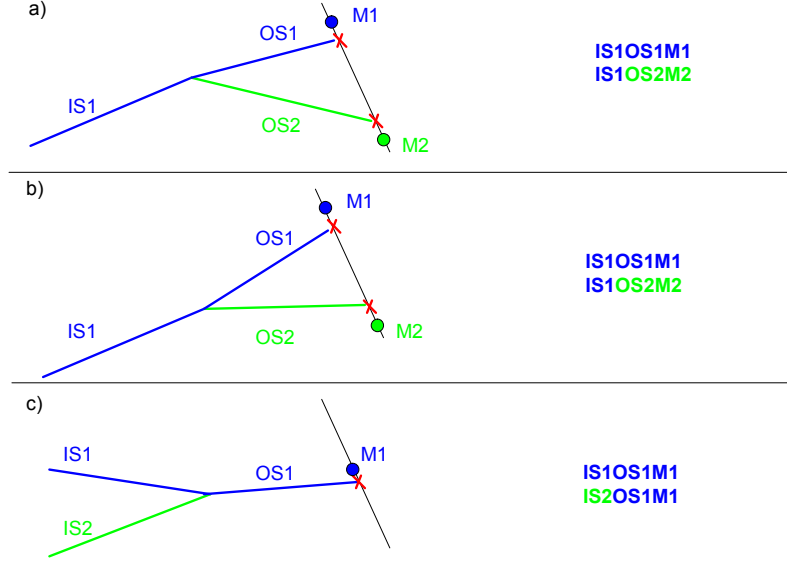


Figure 5.10: Strategy for removing fake track candidates when (a) one inner segment is matched with two outer ones, (b) like in case (a), but tracks have different polarity and (c) two inner segments are matched with one outer segment.

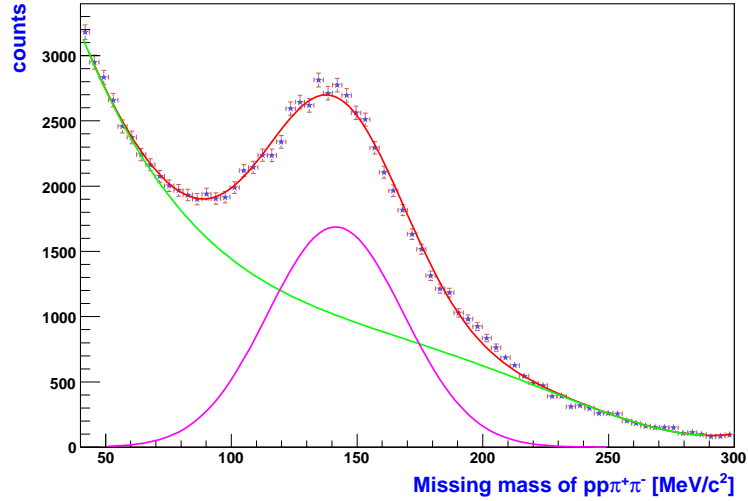
5.3.3 Reaction selection

After the first step of particle identification there is still one unidentified particle: the neutral pion in the 3-pion final state decay and the photon in the Dalitz decay. Missing-mass analysis was used to determine the rest mass of an unobserved particle. In the LAB system, the missing mass (M_{miss}) is given by the following formula:

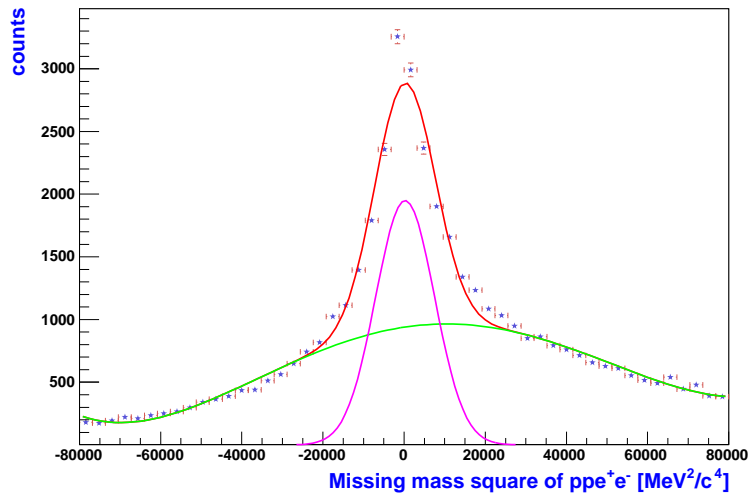
$$(M_{miss})^2 c^4 = \left(E_{beam} + M_p c^2 - \sum E_i \right)^2 - c^2 \left(\vec{p}_{beam} - \sum \vec{p}_i \right)^2 \quad (5.10)$$

where the index i runs over all observed particles in the exit channel, E_{beam} is the total energy of the incoming proton, M_p is the mass of the proton, and p_{beam} is the momentum of the incoming proton.

The missing-mass distribution of four particles ($pp\pi^+\pi^-$), from 3-pion decay of the η meson is shown in Figure 5.11(a). The distribution shows a prominent peak around π^0 mass which is fitted with Gauss function plus a polynomial fit for the background. By putting a cut around the peak one can select the events with missing π^0 (we have used a quite large window between $50 MeV/c^2 - 250 MeV/c^2$ which corresponds to more than 3σ cut in order not to lose statistics).



(a) 3-pion decay



(b) The Dalitz decay

Figure 5.11: Missing-mass distributions of (a) $pp\pi^+\pi^-$ and (b) ppe^+e^- . Both (a) and (b) are fitted with Gaussian for a signal plus polynomial for background. 3.5σ cut around signal peak is used in order to select the reactions with missing π^0 and missing γ , correspondingly.

There is a big contribution from events with no missing particle ($pp \rightarrow pp\pi^+\pi^-$), which gives a peak around zero in the missing-mass distribution of four particles (see Figure 5.11(a)), in which we are not interested. This contribution is less pronounced in the simulation due to the much better track resolution.

Figure 5.11(b) shows the corresponding missing-mass distribution of four particles, $pp e^+ e^-$, for the Dalitz decay of the η meson with the prominent missing γ peak centered at zero. Like in the case of 3-pion final state the peak is fitted with the Gauss distribution plus a polynomial fit for the background. Only the events corresponding to the 3σ cut around the peak were selected.

5.4 η meson reconstruction

The main idea of doing the analysis steps described in the previous sections were to select reactions with missing π^0 corresponding to the decay of η meson into 3-pion final state ($\eta \rightarrow \pi^+\pi^-\pi^0$) and with missing γ corresponding to the Dalitz decay of the η meson ($\eta \rightarrow e^+e^-\gamma$).

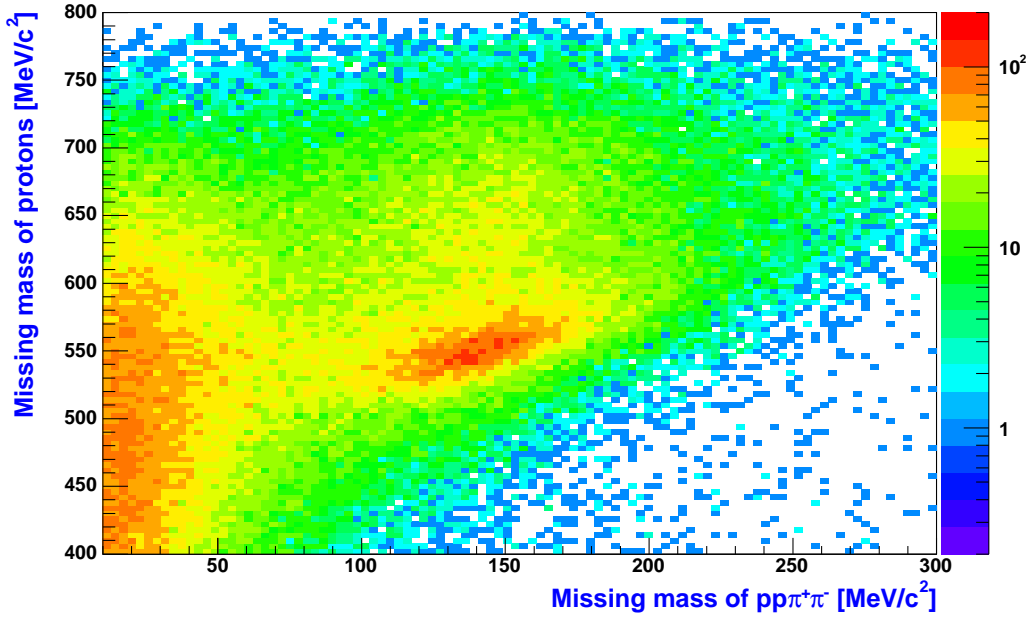


Figure 5.12: Missing mass distribution of $pp\pi^+\pi^-$ as a function of missing mass distribution of two protons for the experimental data, the η peak is seen in the region where the missing mass of four particles is located near the missing pion mass.

Figure 5.12 shows two-dimensional distribution of missing masses of four particles as a function of missing masses of two particles for the 3-pion final state for the experimental

data. One can easily see the η peak corresponding to the events where the missing mass of four particles is centered around the π^0 peak. Figure 5.13 shows similar distribution for the Dalitz decay where the evident peak of the η meson is seen for the missing mass of four particles centered at zero (γ peak).

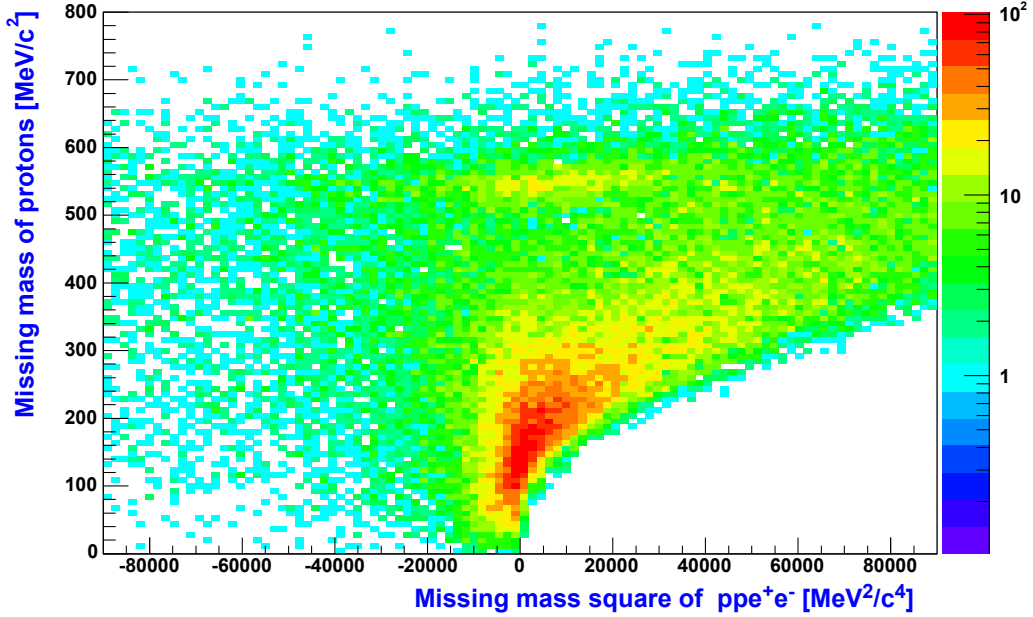


Figure 5.13: Square of missing mass distribution of ppe^+e^- as a function of missing mass distribution of two protons for the experimental data, the η peak is seen in the region where the missing mass of four particles is located at zero (γ peak).

We can reconstruct now η mesons from its 3-pion decay channel by plotting a missing-mass distributions of two protons by imposing a cut around π^0 peak in the missing mass distribution of four particles ($pp\pi^+\pi^-$). In the same way we can plot the missing mass of two protons by imposing a cut around zero on the missing mass distributions of ppe^+e^- . It is also possible to reconstruct missing momentum of π^0 (γ) and plot an invariant mass of $\pi^+\pi^-\pi^0$ ($e^+e^-\gamma$).

By putting a cut around the π^0 peak we get rid of the events where no missing particles appear ($pp \rightarrow pp\pi^+\pi^-$), giving a peak in the distribution of four particle missing masses around zero. There are background events as well where missing π^0 comes not only from the decay of η mesons (pions coming from Δ resonances and non resonant pion production).

Below we present the analysis results, both for simulation and experimental data. The applied selection cuts described in the previous sections are the same for both data samples.

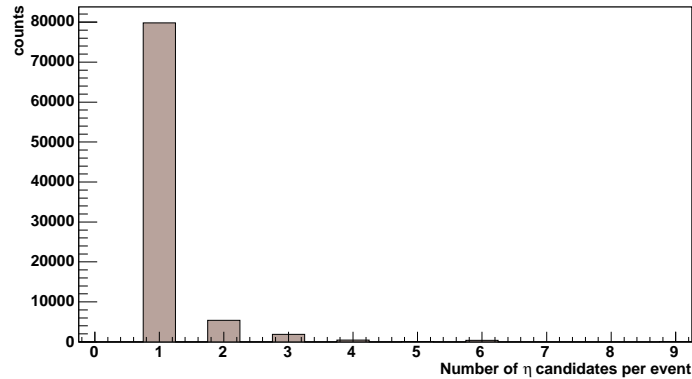


Figure 5.14: Multiplicity of η candidates per event left after all applied cuts. Only the events with one η candidate have been kept.

In order to prevent double counting of the η mesons per event, which can happen due to the fact that there was no cut applied on the number of tracks contributing to the event, the multiplicity cut was applied as well. Figure 5.14 shows the remaining eta candidates per event after performing all previously described cuts. Only the events which have one η meson candidate are selected for the next steps of the analysis.

Table 5.2 shows the number of events analyzed in experimental data and simulation after each condition on the multiplicity of the tracks per event or the events with a given multiplicity of corresponding particles.

Condition	Experiment	simulation
All	309.614.399	
MULT4 triggered	225.727.469	155.745.031
At least three positive and one negative	11.250.690	4.668.294
Three positive and one negative	6.999.624	3.169.480
At least two protons and one dilepton	241.690	89.208
Two protons and one dilepton	134.451	59.138
At least two protons and two pions	3.132.557	2.115.663
Two protons and two pions	2.303.219	1.631.337

Table 5.2: Number of events left under corresponding conditions.

5.4.1 Results for the simulation

The numbers of analyzed events are shown in Table 5.2. The η meson was produced through $N^*(1535)$ (isotropic angular distributions) while a phase space production for the case of the 3- pion final state decay and the Vector Dominance Model for the Dalitz decay have been used.

In this step of the analysis only the tracks with a "meta fake" marks have been removed from the sample, keeping all "track fakes" and using the not fitted tracks as well. The idea was to have a spectrum without imposing an opening angle cut on the pairs.⁷

Figure 5.15 shows the missing-mass distribution of two protons after selecting the events with missing π^0 by imposing a cut around the π^0 peak in the missing-mass distribution of four particles (See Figure 5.11(a)).

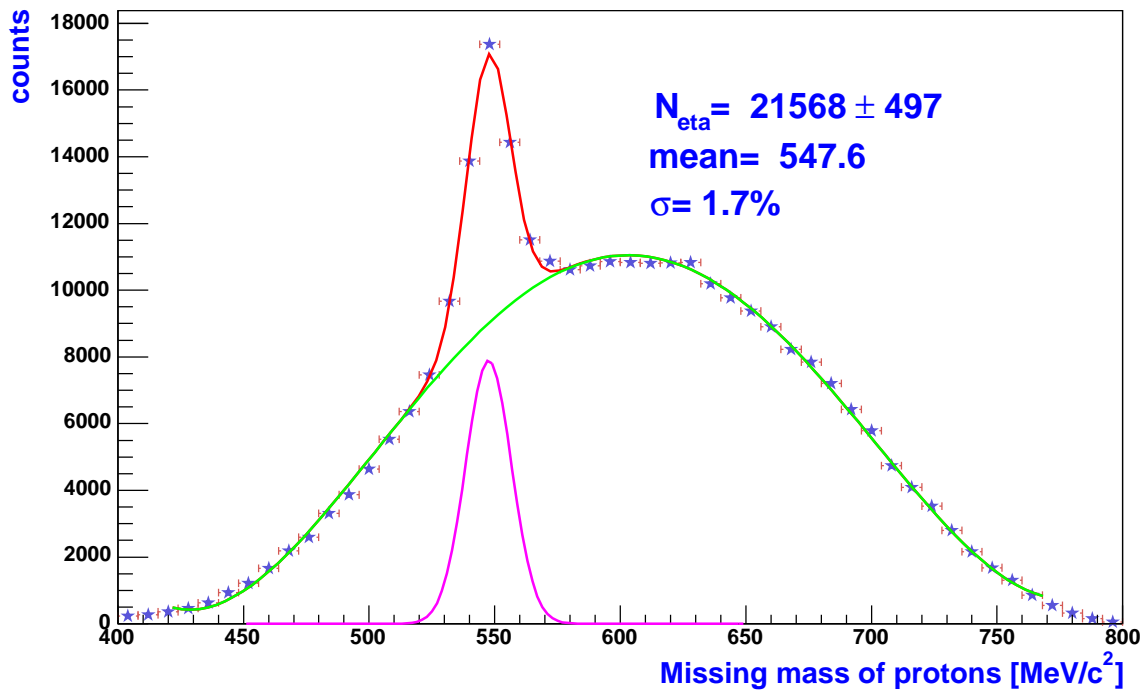


Figure 5.15: Missing-mass distribution of two protons after selecting the events with missing π^0 ; the distribution is fitted with a Gaussian for the signal plus a polynomial for background.

There is an evident peak at the pole mass of the η meson. The peak is fitted with a Gauss distribution plus a polynomial fit for the background. In order to extract the yield we have integrated the signal distribution in the Figure in the mass range between $500 \text{ MeV}/c^2$ and

⁷While removing the "track fakes" one indirectly applies an opening-angle cut between pairs as well.

$600 \text{ MeV}/c^2$. The number of reconstructed η mesons is equal to 21568 ± 497 . The errors on the yield were estimated by error propagation method using the parameters and errors of the fitting Gauss function. The signal is centered at $547 \text{ MeV}/c^2$ with the resolution 1.7%.

Figure 5.16 shows a missing-mass distribution of two protons by imposing a cut around the gamma peak in the distribution of the four-particle missing mass (See Figure 5.11(b)). The evident peak around the η meson mass corresponds to the reconstructed η mesons. As in the previous case the η signal is fitted with a Gauss distribution plus a polynomial fit for the background which is coming from multi-pion production. Besides of the Dalitz decay of the η meson, its 2γ decay is also contributing to the η peak. One of the photons from $\eta \rightarrow \gamma\gamma$ can convert into e^+e^- pairs by hitting some detector parts, thus giving a nice candidate of $e^+e^-\gamma$ which will also contribute to the η peak in the missing-mass distribution of two protons (See section 5.4.4).

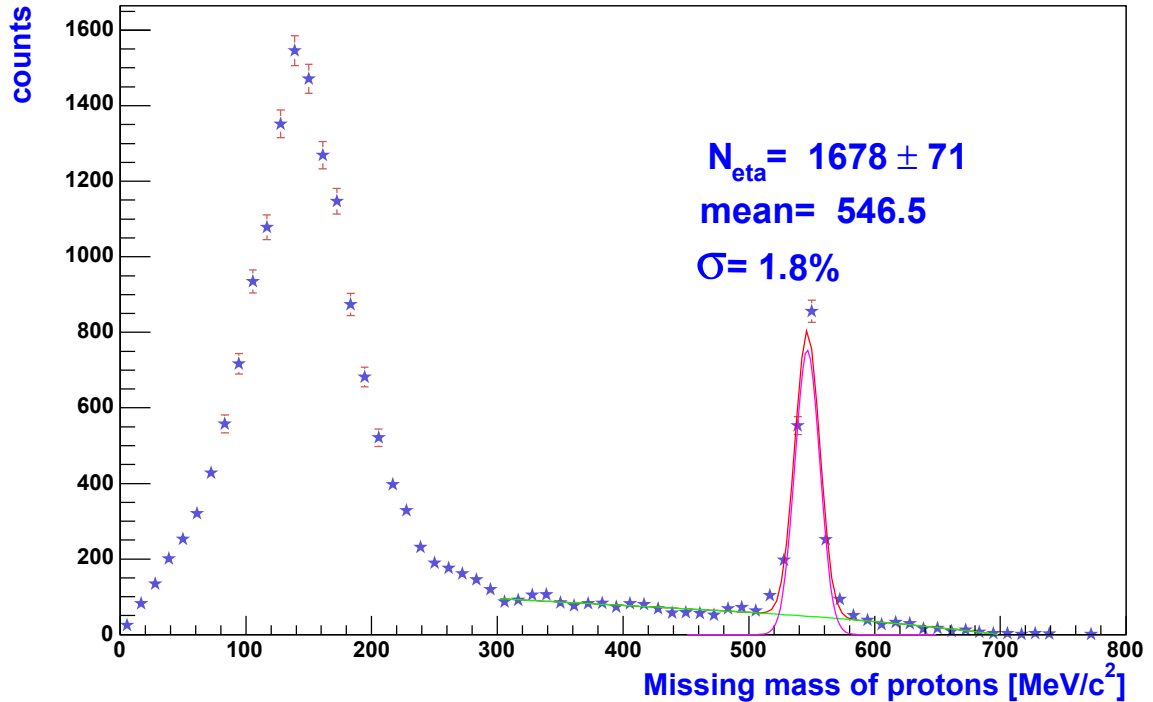


Figure 5.16: Missing-mass distribution of two protons after selecting events with missing γ ; the distribution is fitted with a Gaussian for the signal plus a polynomial for background.

One can also see the peak around the π^0 mass corresponding to the reconstructed pions. The number of reconstructed η mesons obtained in similar way as for 3-pion final state is equal to 1678 ± 71 . From these numbers one can calculate the ratio of reconstructed η mesons between the two decay channels.

5.4.2 Results for experimental data

The number of analyzed events in the experimental data, together with the events left after applying different conditions, are shown in Table 5.2.

Figure 5.17 shows the missing-mass distribution of two protons for the 3-pion final state (The procedure of plotting this picture is in detail explained in the previous section). The η peak has been fitted like for the simulation with a Gauss distribution plus a polynomial fit for the background.

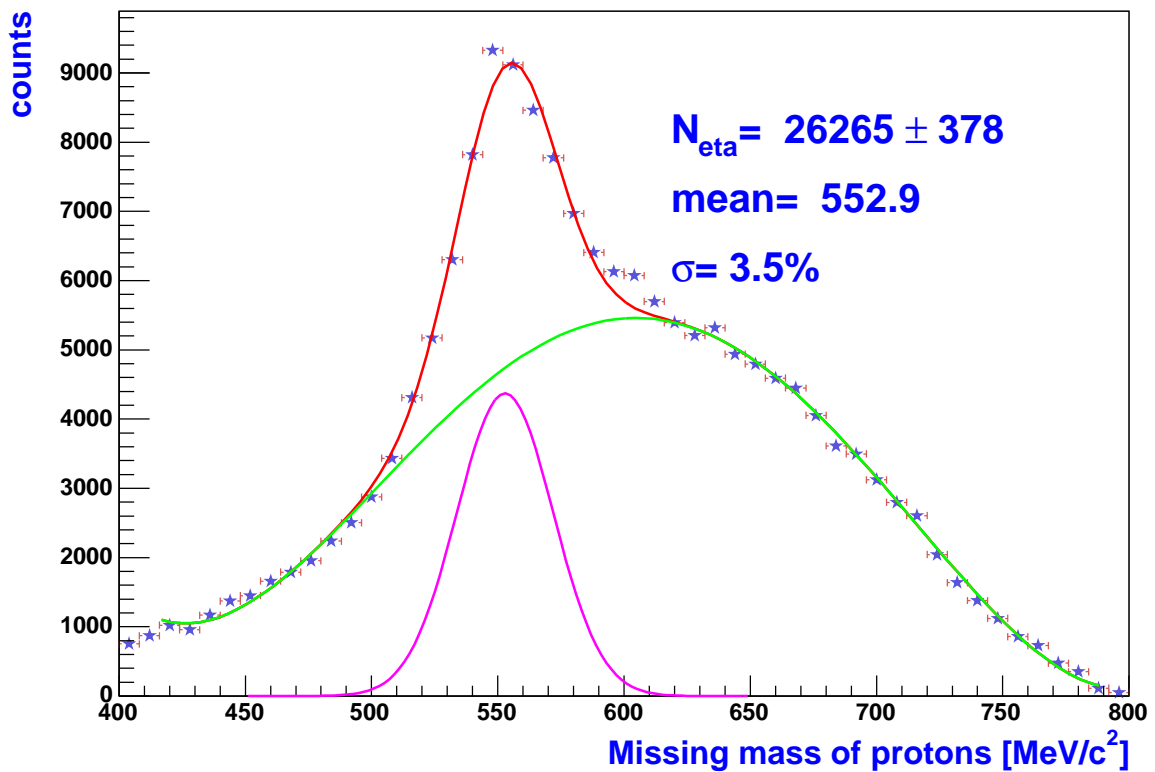


Figure 5.17: Missing-mass distribution of two protons after selecting events with missing π^0 ; the distribution is fitted with a Gaussian for the signal plus a polynomial for background. The yield was calculated by counting the histogram entries above the background due to small structure in the signal.

There is a small structure in the peak as it is shown in Figure 5.17 which is related to the fact that the spectrometer was not fully built during this run. Therefore in the sectors with 3 MDC chambers the resolution of the track reconstruction are worse. As a consequence one Gaussian fit does not describe the peak. Because of this fact, the number of the reconstructed η mesons were calculated by not integrating the signal peak, like in

case of simulation, but just counting the histogram entries above the background, thus taking into account the structure as well. The number of reconstructed η mesons is equal to 26265 ± 378 . The mass of the reconstructed η mesons are located at $553 \text{ MeV}/c^2$ with the width of $18 \text{ MeV}/c^2$ corresponding to 3.5% resolution in mass. In the lower mass region one can also see the contribution from $pp \rightarrow pp\pi^+\pi^-$.

The missing-mass distribution of two protons from η Dalitz decay is shown in Figure 5.18. In this case the reconstructed pion mass is shifted even more than in the simulation and furthermore the background coming from multi-pion production is shifted as well, therefore the calculated number of η mesons is overestimated (Because of the wrong approximation of the background).

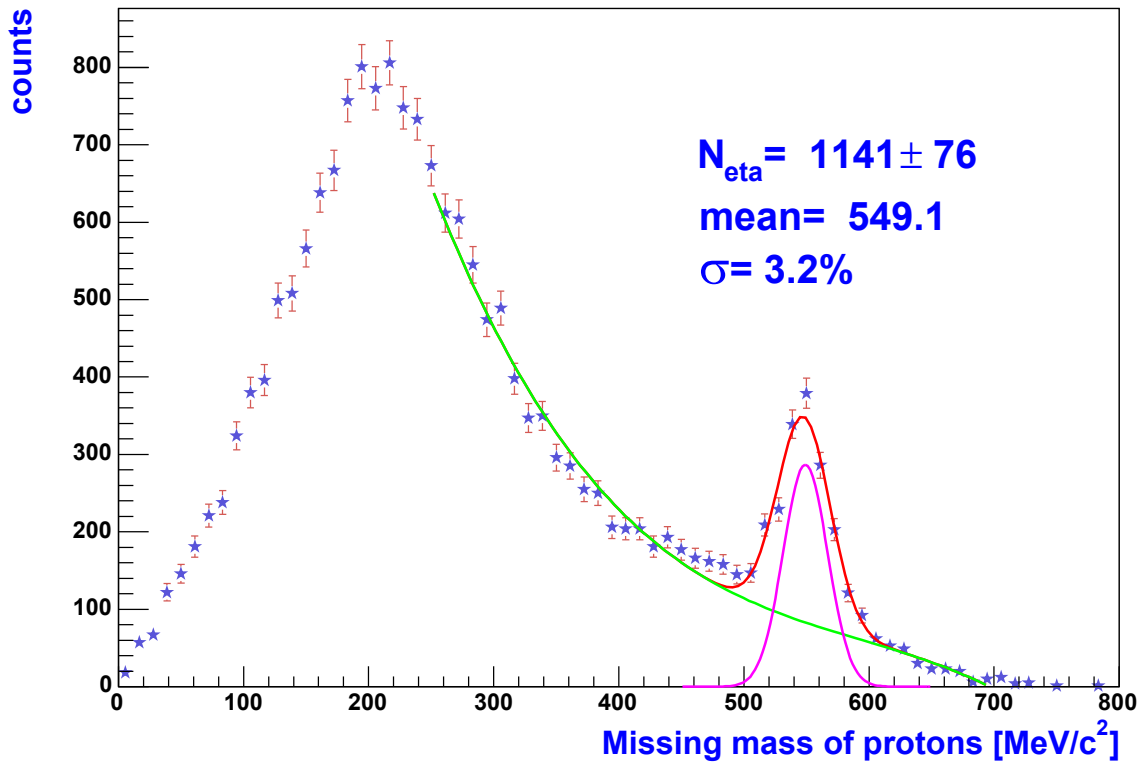


Figure 5.18: Missing-mass distribution of two protons after selecting events with missing γ ; the distribution is fitted with a Gaussian for the signal plus a polynomial for background.

5.4.3 Kinematic fit

Kinematic fit is a mathematical procedure that uses physical constraints, such as energy-momentum conservation, to improve measurements [75]. In general, one uses constraints

to impose "external knowledge" of a physical process to govern the behavior of the fit, thereby forcing the fit to conform to physical principles which are not known by the internal variables of the fit. When constraints are applied, the effective number of unknowns (degrees of freedom) in the fit is reduced by the number of constraints. The constraints are imposed using the well known Lagrange multiplier technique. It is important to choose "proper" track parametrization for kinematic fit. The word "proper" means, the parameters should have physical meaning and be kinematically complete, the errors of parameters should be close to gaussian. The following track parametrization was used for the algorithm:

$$\alpha_i = \begin{pmatrix} \frac{1}{p_i} \\ \theta_i \\ \phi_i \end{pmatrix} \quad (5.11)$$

where the index i runs over all 4 tracks.

From a mathematical point of view the procedure means finding a minimum of the function (For details see Appendix C):

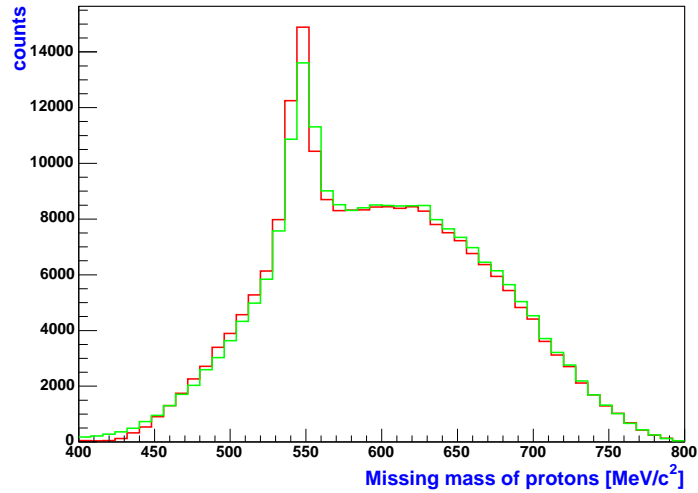
$$F = (\alpha - \tilde{\alpha})^T W^{-1} (\alpha - \tilde{\alpha}) + 2\lambda^T H(\tilde{\alpha}) \quad (5.12)$$

where λ is a matrix of Lagrange multipliers, H is a matrix of constrains, α is a matrix of track parameters, and $\tilde{\alpha}$ is a matrix of modified track parameters. The factor 2 before the Lagrange multipliers is introduced in order to simplify the calculations. The quality parameter for the fitting is the first part of 5.12, which approaches the well known χ^2 distribution with the degrees of freedom being equal to the number of constraints used.

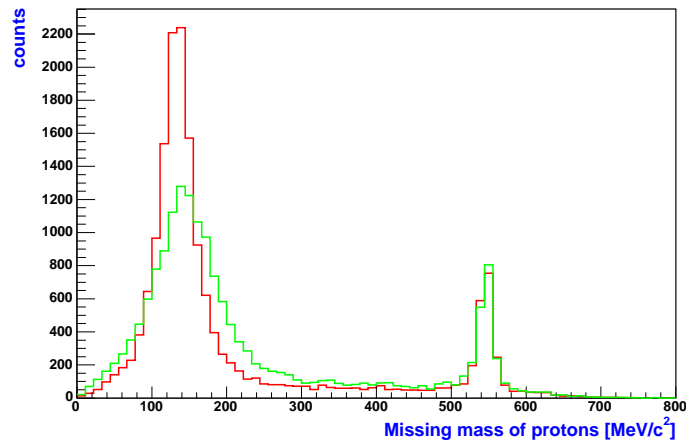
Only one constraint for each decay channels has been used:

- missing mass of $pp\pi^+\pi^- = m_{\pi^0}$ for the 3- pion final state
- missing mass of $ppe^+e^- = m_{\gamma} = 0$ for the Dalitz decay

The comparison of missing-mass distributions of two protons before and after the kinematic fit for the simulation in case of 3-pion final state and the Dalitz decay are shown in Figures 5.19(a) and 5.19(b) correspondingly. Similar distributions are shown for experimental data in Figures 5.20(a) and 5.20(b).



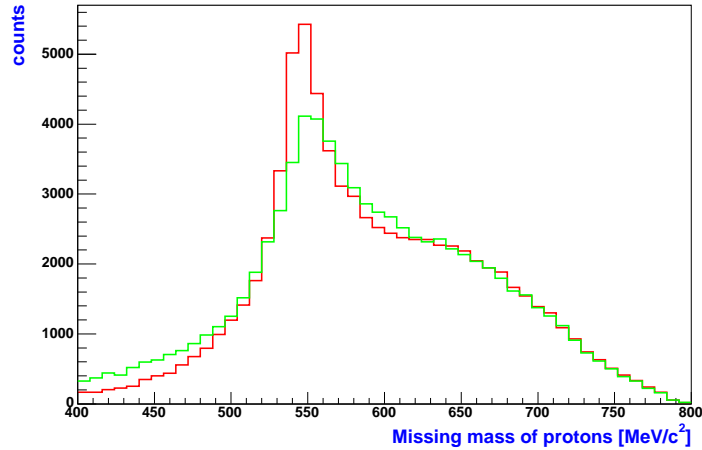
(a) 3-pion decay



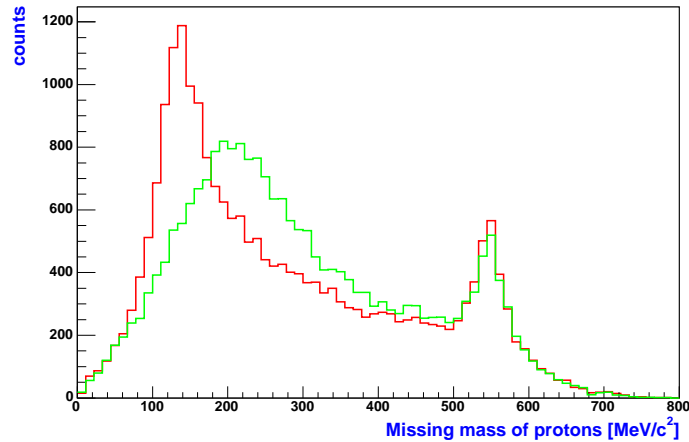
(b) Dalitz decay

Figure 5.19: Comparison of missing-mass distributions of two protons for simulation before (green) and after (red) the kinematic fit algorithm. (a) after selecting events with missing π^0 in missing mass distributions of $pp\pi^+\pi^-$ and (b) after selecting events with missing γ in missing-mass distributions of ppe^+e^- .

While there is no big improvement for simulation in the η region, connected to a quite good tracking resolution in this case, there is a significant improvement of the η mass resolution (almost factor of 1.5 for 3-pion decay and factor of 1.2 for the Dalitz decay) and signal to background ratio for experimental data.



(a) 3-pion decay



(b) Dalitz decay

Figure 5.20: Comparison of missing-mass distributions of two protons for experimental data before (green) and after (red) the kinematic fit algorithm. (a) after selecting events with missing π^0 in missing mass distributions of $pp\pi^+\pi^-$ and (b) after selecting events with missing γ in missing-mass distributions of ppe^+e^- .

Looking at the lower mass part of missing-mass distributions for 3-pion decay before and after the kinematic fit one can see the decrease of the contribution from the $pp\pi^+\pi^-$ channel (after applying a 5% significance level cut on χ^2 distribution of the kinematic fit) as well, moreover this decrease is more pronounced for experimental data. Furthermore

for the Dalitz decay, the pion mass both in simulation and experimental data is shifted into the correct place, and the background corresponding to the multi-pion production is more realistic.

Figures 5.21(a) and 5.21(b) show the kinematic fit χ^2 distributions compared with the theoretical one for the 3-pion final state and the Dalitz decay, correspondingly. One can see the nice agreement between the two distributions indicating the fact that the parameters were changed inside the errors.

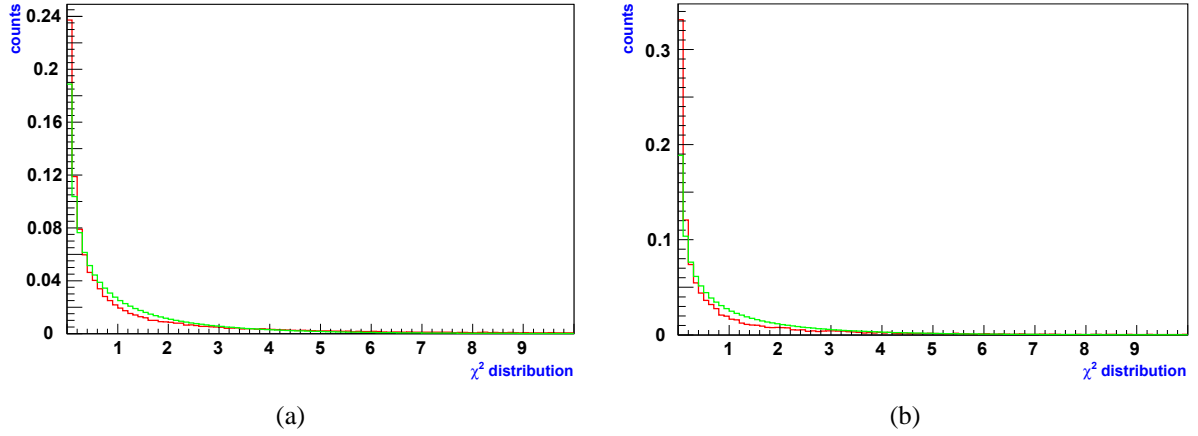


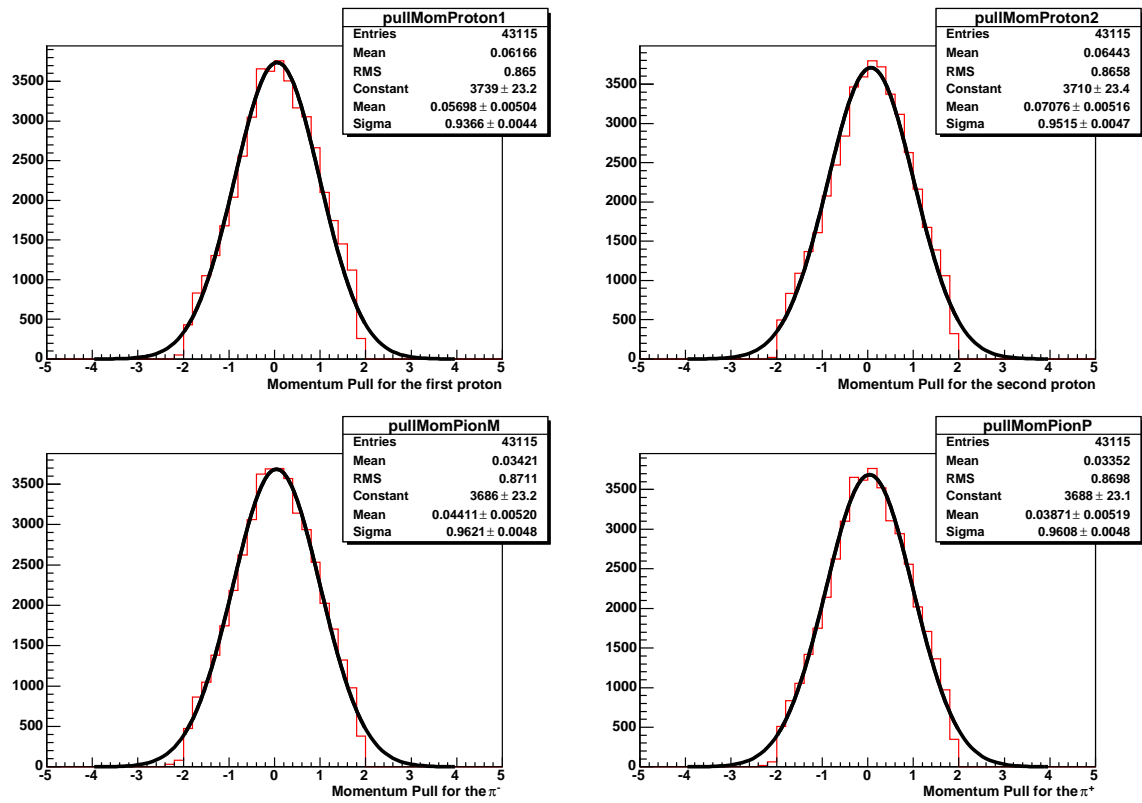
Figure 5.21: χ^2 distribution of the kinematic fit for 3-pion final state (a) and the Dalitz decay (b) for experimental data. The green distributions correspond to the calculated χ^2 function, while red distributions are obtained from the data.

One should keep in mind that it is possible to parameterize the errors incorrectly, but still have a consistent χ^2 distribution or a flat Confidence Level distributions. The pull distributions provide a way to guard against this.

The pull of the i^{th} fit quantity is defined as,

$$pull_i = \frac{\alpha_i - \tilde{\alpha}_i}{\sqrt{\sigma^2(\alpha_i) - \sigma^2(\tilde{\alpha}_i)}} \quad (5.13)$$

The pulls should be normally distributed about zero with a $\sigma = 1$. A systematic error in one of the measured quantities, α_i , can be seen as an overall shift in the distribution of the corresponding $pull_i$ away from zero. Similarly, if the error of α_i has been (over-estimated) underestimated, then the corresponding pull distribution will be too (narrow) broad. Figures 5.22, 5.23 and 5.24 show the pull distributions of all parameters used in the kinematic fit for the 3-pion final state fitted by the Gauss distributions. The width of the pull distributions are equal to 1 only after re-scaling (increasing by a factor of 1.5) of the angular errors provided by a track fitter (Which are propagated from the errors of the drift times generated by the GARFIELD simulation). Similar distributions are obtained for the Dalitz decay as well.

Figure 5.22: Pull distributions for inverse momenta of p, p, π^- and π^+ .

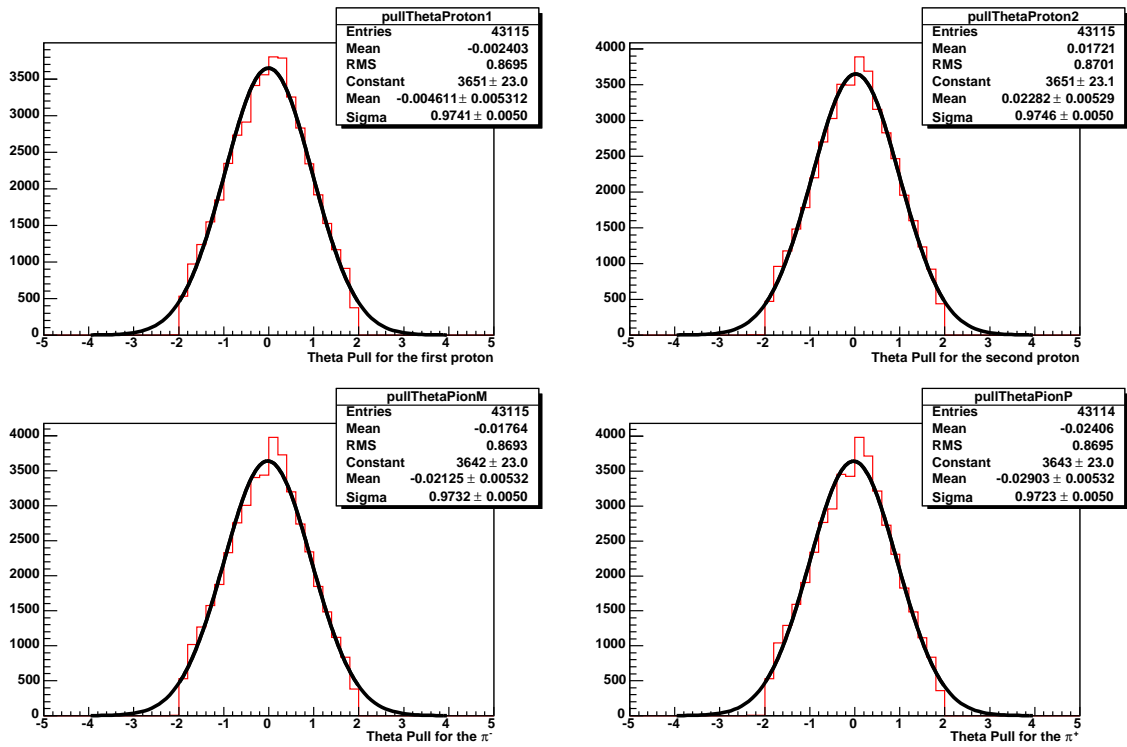
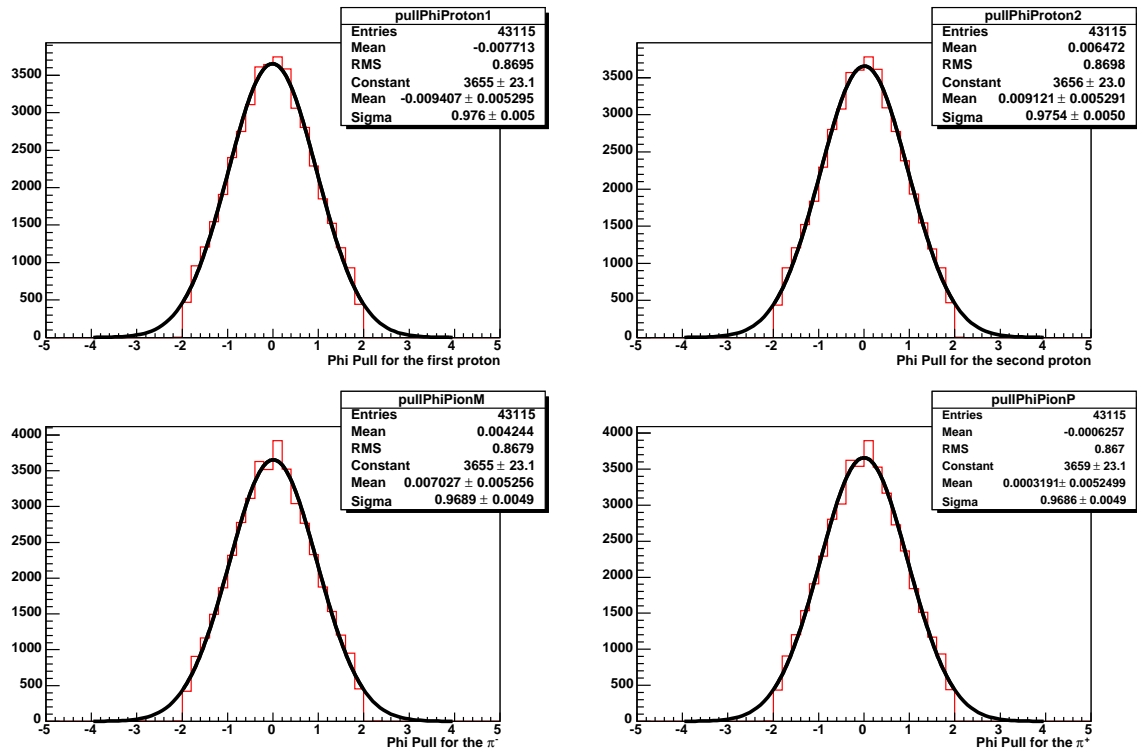


Figure 5.23: Pull distributions for polar angles of p, p, π^- and π^+ .

Figure 5.24: Pull distributions for azimuthal angles of p, p, π^- and π^+ .

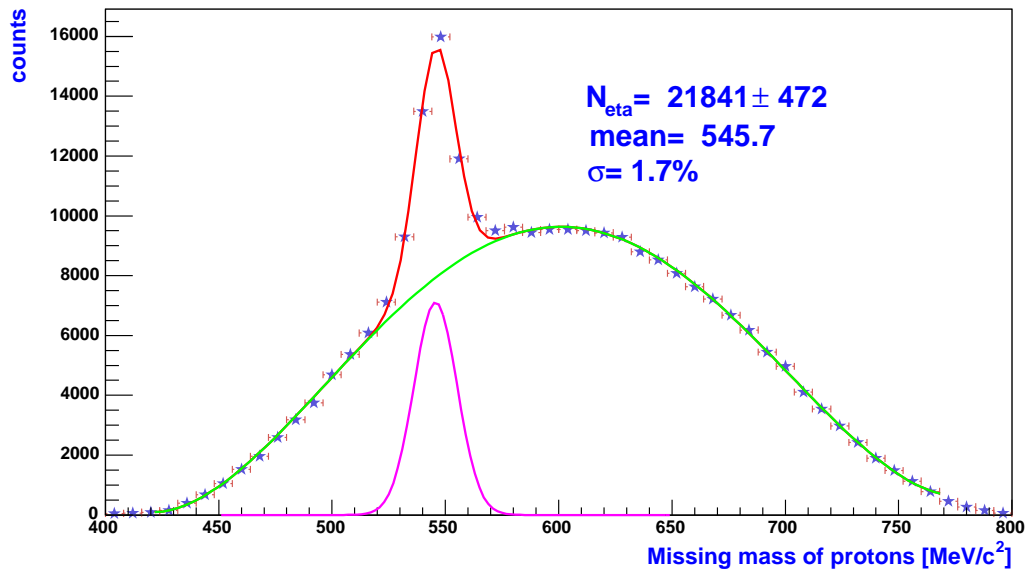


Figure 5.25: Missing mass distributions of two protons after selecting events with missing π^0 for simulation after the kinematic fit.

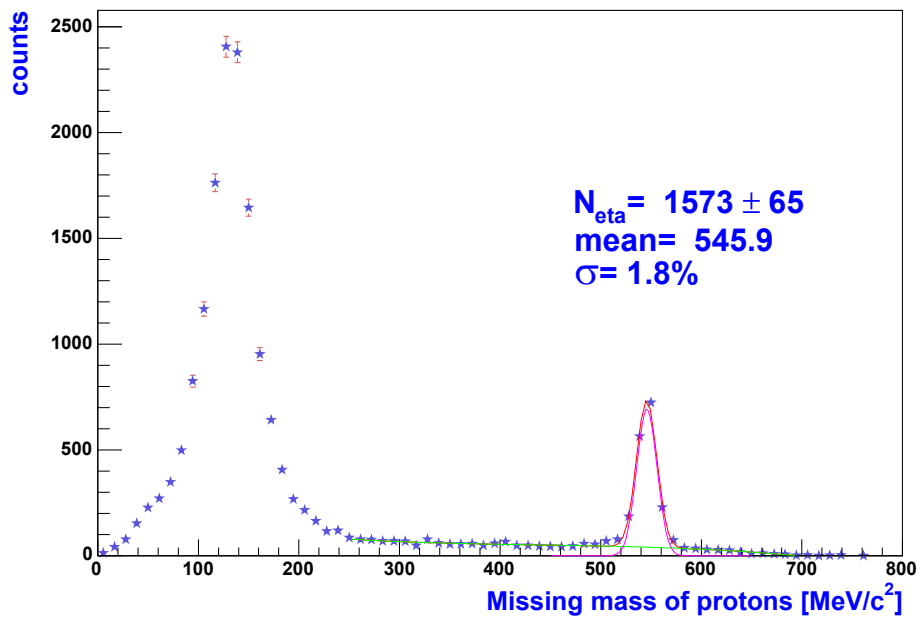


Figure 5.26: Missing mass distributions of two protons after selecting events with missing γ for simulation after the kinematic fit.

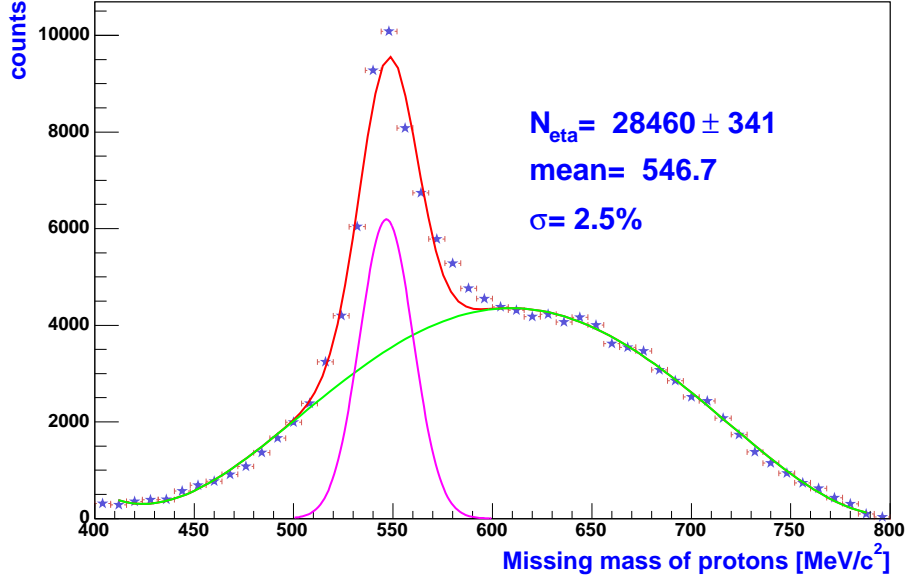


Figure 5.27: Missing-mass distributions of two protons after selecting events with missing π^0 for experimental data after the kinematic fit.

The missing-mass distributions of two protons for the 3-pion final state after application of the kinematic fit algorithm is shown in Figure 5.25 for the simulation. The η peak was fitted with a Gauss function plus a polynomial fit for the background. The reconstructed number of η mesons is equal to 21841 ± 472 . The peak is centered around $546 \text{ MeV}/c^2$ with the resolution of 1.7%. The missing mass distribution of two protons for the Dalitz decay of the η mesons is shown in Figure 5.26. As it is seen from the Figure the pion mass is shifted to the correct position with much narrow width. The number of reconstructed η mesons is equal to 1573 ± 65 . The η peak is centered around $546 \text{ MeV}/c^2$ with the resolution of 1.8 %.

Similar distributions for the experimental data are shown in Figures 5.27 and 5.28 for the 3-pion and the Dalitz decays the η meson, correspondingly. The number of reconstructed η mesons from the 3-pion final state, which was obtained by counting a histogram counts above the background in Figure 5.27 due to the small structure in the η yield, is equal to 28460 ± 341 . The η peak is centered around $547 \text{ MeV}/c^2$ with the resolution of 2.5%. We get a factor of 1.5 improvement in the mass resolution of the reconstructed η mesons after application of the kinematic fit algorithm. The reason for increasing of the reconstructed η meson yield from its 3-pion decay is partly connected to the background approximation accuracy. The systematic shift on the level of 5% can easily be obtained by changing the range and shape of the background function. The reconstructed number of η mesons after application of the kinematic fit from its Dalitz decay is equal to 1034 ± 64 . The η peak is centered around $548 \text{ MeV}/c^2$ with the resolution of 2.8 %. In this case we

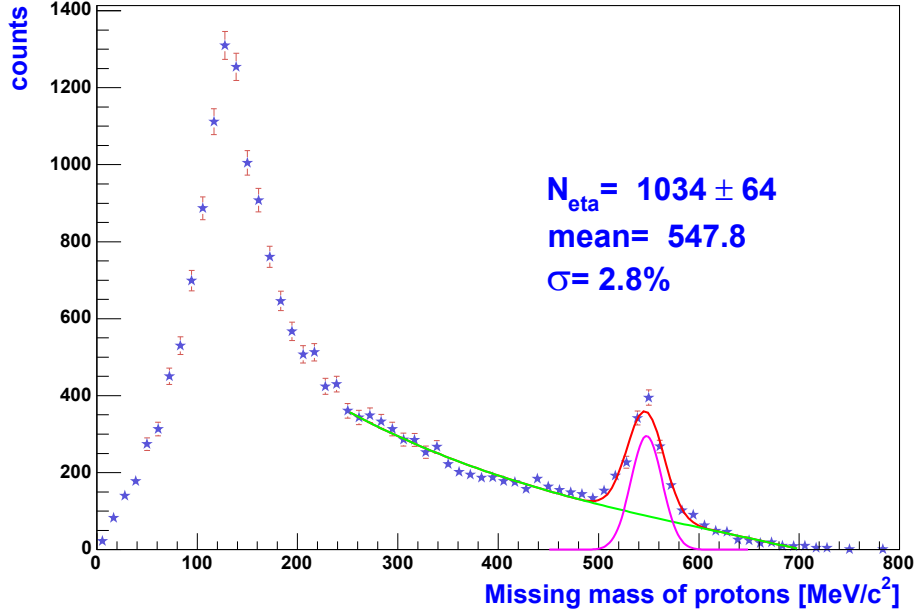


Figure 5.28: Missing-mass distributions of two protons after selecting events with missing γ for experimental data after the kinematic fit.

get an improvement by a factor of 1.2 in the mass resolution of the reconstructed η mesons compared with the results obtained without application of the kinematic fit algorithm. Furthermore as it is seen from Figure 5.28 the pion mass is shifted into its correct position with much improved width. The background corresponding to multi-pion production is also more realistic after application of the kinematic fit. The decrease in the number of η mesons from its Dalitz decay after application of the kinematic fit has several reasons. One of them is connected to the fact that before the kinematic fit the background is shifted as it is seen from Figure 5.18. As a consequence the background approximation is also wrong. Another reason is as in case of 3-pion final state the systematic shift in the background approximation.

5.4.4 Contribution from $\eta \rightarrow \gamma\gamma$

Besides the $\eta \rightarrow e^+ e^- \gamma$ decay there is a contribution from $\eta \rightarrow \gamma\gamma$ as well to the number of reconstructed η mesons. One of the photons may convert into $e^+ e^-$ pairs by hitting some detector part⁸.

⁸Pair production from a γ is not possible in vacuum due to the energy conservation law. Indeed if one assumes this decay to happen in e.g. the LAB system then there is an infinite number of frames moving with respect to LAB frame where this process can happen as well. In each of these systems the photon will be

Figure 5.29(a) shows the missing mass of two protons for all pairs (black) for the case where one of the leptons is coming from conversion (green) and whose both particles are coming either from pions or eta mesons (red) (Dalitz decay).

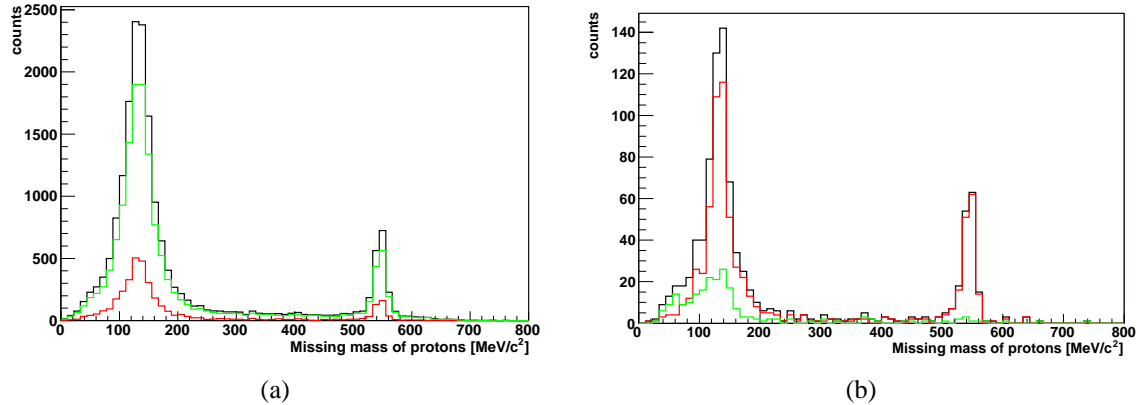


Figure 5.29: Missing-mass distribution of two protons for the Dalitz decay for all pairs (black), when at least one of the dileptons is coming from γ conversion (green) and when both leptons are parent particles (red), before applying the cuts (a) and after applying the cuts (b).

One can easily see that the main contribution is due to the conversion pairs. The characteristic feature of the conversion pairs is that the opening angle between leptons is very small. As a consequence these tracks will be close to each other in the Drift chambers thus will not be fitted by the track fitter. This will increase the number of fake tracks created. Therefore, in order to get rid of these events, several cuts described below have been applied:

- a) Removing fake track contributions
- b) Opening angle cut
- c) Using segment's χ^2 cut

After applying these cuts the distribution is plotted again in Figure 5.29(b); one has much smaller contribution from the conversion decay.

seen with a shift of its frequency ν due to the Doppler effect. One can choose a reference system where it is less than E_0/h , where E_0 is equal to $2m_e c^2$; therefore the energy of the photon $h\nu$ will not be enough for pair creation in this frame. Consequently this process can not happen in the LAB frame. On the other hand, in the presence of a nucleus or an electron this process can happen because the energy and momentum of the photon will be shared between 3 particles in this case.

5.5 Estimation of the dilepton identification efficiency

At this point we can estimate the dilepton identification efficiency of the HADES spectrometer by calculating a ratio (R) (See Section 5.0.1):

$$R = \frac{R_{exp}}{R_{sim}} \quad (5.14)$$

where R_{exp} and R_{sim} are the ratio of reconstructed η mesons from its 3-pion and Dalitz decays correspondingly for experimental data and simulation.

For estimation of R_{exp} two things should be taken into account. For the 3-pion final state only downscaled events have been analyzed. Therefore the downscaling factor should be taken into account for normalization (See section 2.5). The downscaling factor was taken into account on event-by-event basis⁹, therefore each bin of the missing mass distribution in case of 3-pion final state was filled downscaling factor times. For the Dalitz decay only the events with positive second level trigger decision have been taken. Therefore the efficiency of the second level trigger should be taken into account as well. This efficiency can be calculated using only downscaled events by evaluating the ratio of reconstructed η mesons with positive decision of the second level trigger to the reconstructed η mesons from the whole sample which amounts to almost 82%. Thus the ratio should be calculated with:

$$R_{exp} = \frac{N_{had}}{N_{Dalitz}/\varepsilon_{LVL2}} \quad (5.15)$$

where $\varepsilon_{LVL2} = 0.82$ is the efficiency of the second level trigger.

The obtained results are discussed in Chapter 6.

In simulation no downscaling were applied. The LVL2 trigger decision was not used as well in simulation.

5.6 η meson production

In order to investigate the production mechanism of the η mesons their angular distributions were reconstructed in the center- of-mass system of two protons. For this investigation only the 3- pion final state has been used because of the high statistics available in this case. In order to subtract a background the missing-mass distribution was plotted for 10 bins of the reconstructed angle thus allowing us to see how background changes as a function of the angle. The signal in each bin was fitted from a shape of the η mesons taken from simulation while for the background the polynomial fit has been used. After subtracting the

⁹Because of the fact that the downscaling factor was changing from file to file, this correction has been made on the event level.

background the one-dimensional picture for angular distributions is compared to the corresponding distribution obtained from simulation of pure η mesons by nucleon excitation to the $N^*(1535)$ state, as illustrated in Figure 5.30. As the orbital momentum of this excited state is equal to 0, the angular distributions should be flat (s wave decay). The nice agreement of the experimental distribution with simulated one (blue line in the Figure) confirms the s wave production of the η meson. This illustrates that the assumption of production of the η mesons through $N^*(1535)$ in simulation are in good agreement with the experimental data.

One should note that the discrepancy of the obtained distribution, as it is seen in Figure 5.30, from an isotropic one is due to the acceptance of the HADES spectrometer. After acceptance correction for the phase space we should have again the s wave distribution as it is assumed in event generation (before going to the HADES acceptance).

Obtained angular distributions of the η mesons is compared with the simulation where the anisotropy observed by the DISTO experiment was included (green line in Figure 5.30). On can see from the Figure that both simulations (with isotropic (blue) and anisotropic (green) angular distributions) describes the data quite well within error bars.

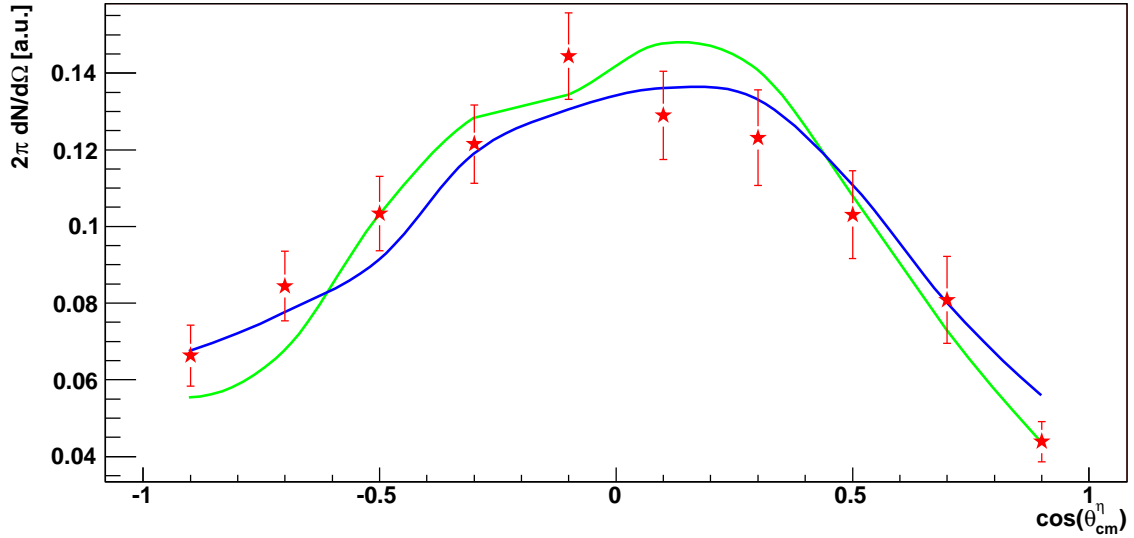


Figure 5.30: Angular distributions of the η mesons after background subtraction in the center-of-mass system of protons from experimental data (red points) compared with those obtained from simulation (blue line) generated isotropically through the N_{1535}^* resonance. The green line corresponds to the simulation where the anisotropy observed by the DISTO experiment has been included.

5.7 η meson decay

The Dalitz decay of the type $\eta \rightarrow e^+e^-\gamma$ can be reduced to a decay into a real photon plus a virtual photon and a subsequent decay of the virtual photon to e^+e^- pair [2, 6]. If there is a structure around the η meson, which is characterized by a transition form factor, this will affect the probability of emitting the virtual photon with a given momentum, consequently the invariant-mass distribution of e^+e^- pairs will be affected as well because the square of momentum of the photon is just equal to the invariant mass of the lepton pairs it decays to. The distribution will look different for a pure QED calculations where no structure around the meson is taken into account. In the Vector Dominance Model this effect is taken into account by the coupling of the virtual photon to a virtual vector mesons like ρ, ω or ϕ . Thus the virtual photon can interact with the hadron also after a transition to the virtual vector meson state. In order to investigate the validity of the Vector Dominance Model in describing this decay the experimentally reconstructed e^+e^- invariant mass distribution after background subtraction is compared to the VDM model calculation.

As the background in the pp missing-mass spectrum can nicely be described by a straight line one can construct 3 trapezoids as shown in Figure 5.31. The number of events inside the middle trapezoid will be equal to the arithmetic mean of the left and right ones (because the middle line of any trapezoid is defined as the arithmetic mean of its bases, the sum of the entries in each bin of the middle trapezoid will be equal to the averaged sum of the corresponding bins from the side trapezoids); therefore, in order to subtract a background, first three distributions of invariant masses are created corresponding to the region of missing masses covered by the corresponding trapezoids. The averaged mean of the invariant-mass distributions corresponding to the left and right side bands were subtracted from the central one. The distribution obtained in this way is plotted in Figure 5.32. The red solid line in the Figure corresponds to the calculations done with the Vector Dominance Model, while the blue line corresponds to pure QED calculations. Except the last bin the model describes the data quite well within error bars.

There can be several reasons responsible for the discrepancy of the last bin from the VDM calculations in the invariant-mass distribution of e^+e^- pairs, as shown in Figure 5.32:

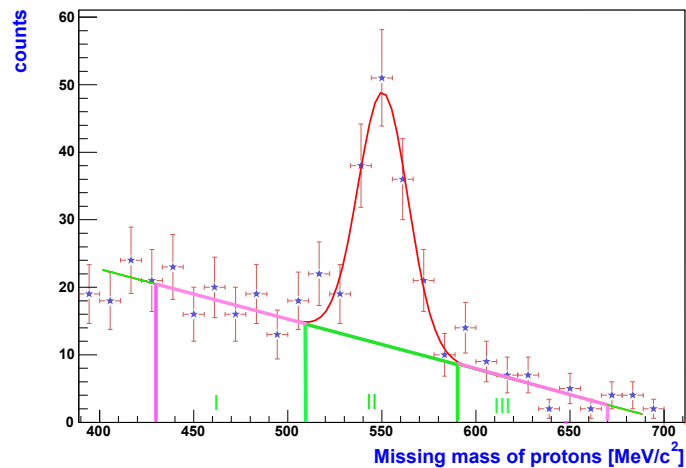


Figure 5.31: Illustration of the background subtraction. The background is estimated as the averaged mean from side bands.

this may come from physics, the method for background subtraction can be not applicable for this bin or this might be attributed by other processes, like contribution from multi-pion production, or contribution from fake combinations.

In order to test the background subtraction method, another method was tried, like in case of background subtraction for angular distributions. The missing mass distributions of two protons were plotted for several slices of e^+e^- invariant mass distribution. In this way it is possible to investigate the background behavior as a function of the invariant mass of e^+e^- pairs. The results of this method shows similar behavior for the last bin in the invariant mass distribution of e^+e^- pairs. It is not clear how the background behaves in this bin. The background can be estimated using simulated data with realistic physics processes.

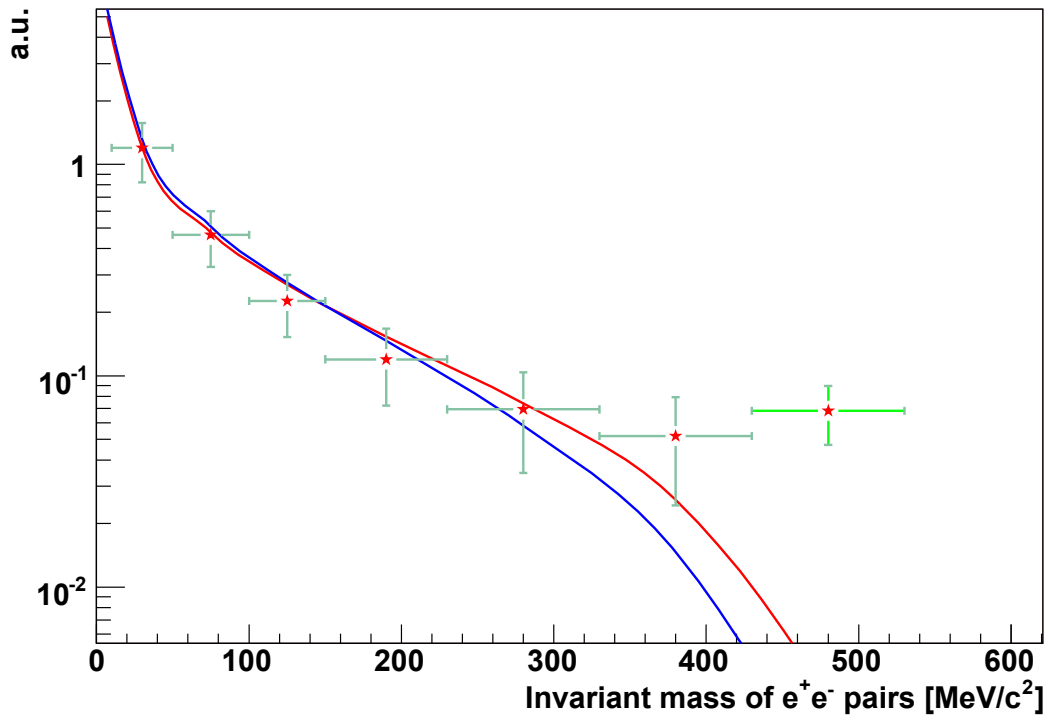


Figure 5.32: Invariant mass distributions of e^+e^- pairs, from experimental data, after acceptance correction compared with Vector Dominance Model calculations (red) and QED calculations (blue).

Since in our simulation the VDM model was used for the η meson Dalitz decay, it was obvious to reconstruct the invariant mass distributions of the e^+e^- pairs from simulation and compare with the VDM model calculations. The results of this analysis is shown in Figure 5.33. As it is seen from the Figure the problem exists also in simulation, but less pronounced. Therefore this might be connected to the estimation of the background in this

bin, and not to the VDM model itself. This might also be connected to the created fake combinations. We expect that fake track contributions from simulation is smaller, due to the better reconstruction resolutions in this case.

Another important thing can be seen by comparing the invariant mass distributions from simulation and experimental data. In case of simulation one can see entries in the e^+e^- distribution at the pole mass of the η meson, while this is not the case for the experimental data, the direct decay of the η meson to e^+e^- pairs. There exists a lower limit on branching ratio of this decay channel in [76], which was used in our simulation. On the other hand, as it is shown in the Table 5.2, the analyzed statistics is more for experimental data compared to the simulation. Therefore we can conclude that the lower limit presented in [76] for this decay channel is larger than it should be.

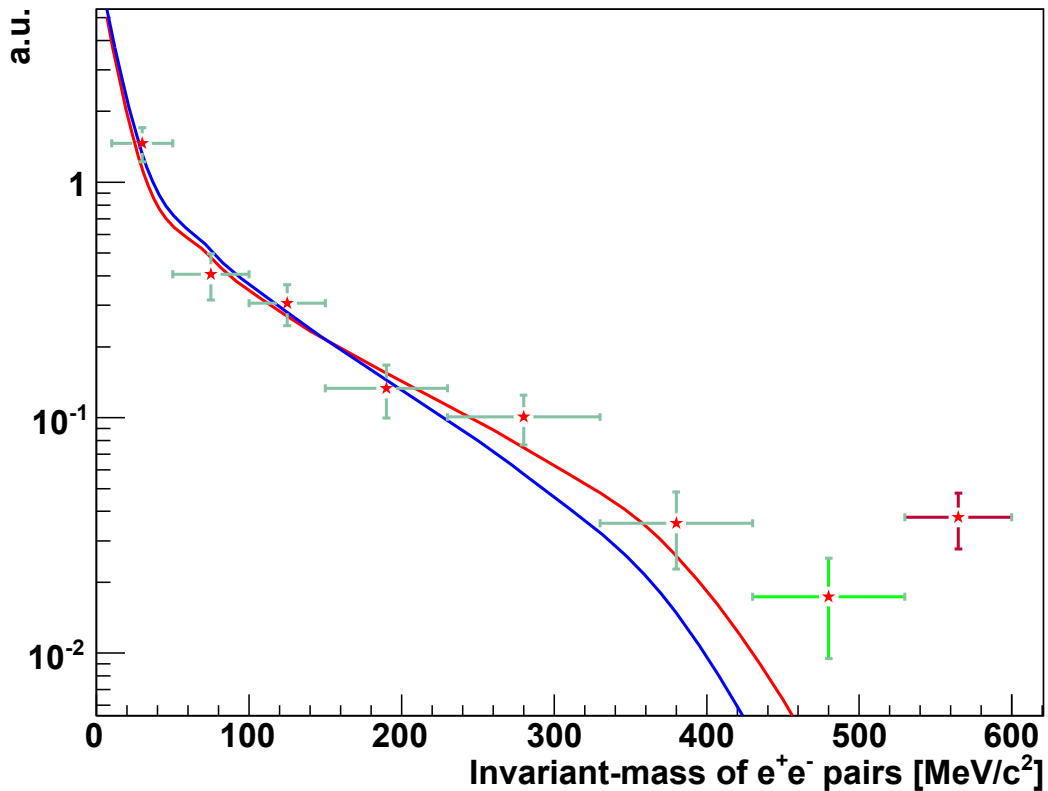


Figure 5.33: Invariant mass distributions of e^+e^- pairs, from simulation, after acceptance correction compared with Vector Dominance Model calculations (red) and QED calculations (blue).

Chapter 6

Discussion and Outlook

In this chapter the main obtained results are presented:

- Section 6.0.1: Estimation of the dilepton identification efficiency of the HADES spectrometer
- Section 6.0.2: Investigation of the η meson production
- Section 6.0.3: Test of the VDM model in describing the η meson decay

The first proton-proton production run at 2.2 GeV kinetic energy of incident proton beam was conducted successfully in January 2004. It was the first time when the spectrometer was fully set up in four sectors out of the six. The remaining two sectors had one missing MDC chamber; therefore it was necessary to develop a new algorithm for momentum reconstruction which uses information from all four (or three) MDC chambers in the setup in order to achieve high momentum resolution. Basically, one needs either the input momentum or some reference points inside the magnetic field on the trajectory of the particle. As this information is not available, the reconstruction procedure was based on assuming a cubic spline model for the track with the objective of estimating points from the model and derivatives at those points inside the magnetic field. In the next step the field equations were solved by imposing a particle to go through the points taken from the track model by fitting the momentum which satisfies this condition. As the method uses a model which sometimes differs from the real trajectory of the particle, especially in the low-momentum region and the regions close to the magnet coils, a correction table was created in order to take into account this effect. The obtained resolution of the method is in the order of 1 – 2%. The spline method provides the sign of the charge of the particle as well. The momentum reconstructed with the spline method, together with its sign, is then taken as an initial value for tracing the particle through the spectrometer by solving the equation of motion for the particle. The obtained second-order differential equations are solved using Runge Kutta methods where all initial conditions are fixed from track fitting

and an initial momentum is taken from the spline method. As there is a residual magnetic field inside the MDC chambers, the real trajectory of the particle differs from the straight line assumption made on track segments before and after the magnetic field in the track fitting; therefore in the method of Runge Kutta, not only the momentum, but also the angles are varied during the minimization procedure. However there are still some problems, especially for momenta below 70 MeV/c, due to the straight segment assumption.

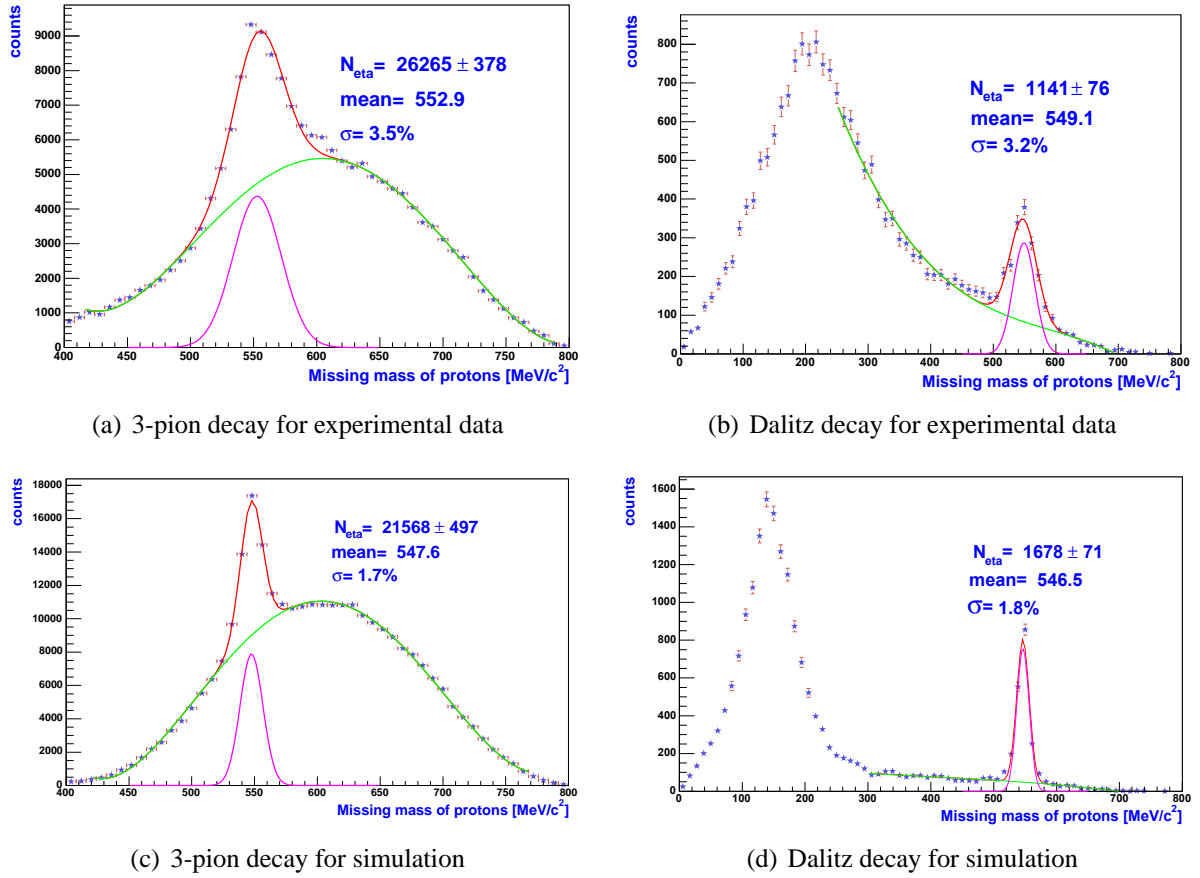


Figure 6.1: Missing-mass distributions of two protons before applying the kinematic fit algorithm; (a) for experimental data after applying a cut around π^0 peak in the missing-mass distributions of four particles, (b) for experimental data after applying a cut around γ peak in the missing mass distributions of four particles, (c) for simulation corresponding to the 3-pion decay of the η meson, and (d) for simulation corresponding to the Dalitz decay of the η meson.

The main goal of collecting these data was to investigate the spectrometer performance in terms of resolution, alignment and exclusively reconstruct the η mesons created well above the production threshold, in order to estimate the dilepton identification efficiency

of the HADES spectrometer. Besides these studies, the production mechanism of the eta mesons and its Dalitz decay were investigated as well.

6.0.1 Dilepton identification efficiency of the HADES spectrometer

The dilepton identification efficiency has been estimated by exclusive reconstruction of two decay channels of the η meson. In order to estimate the relative branching ratios of investigated decay channels inside the HADES acceptance a simulation has been done by taking into account all known processes at his energy. Furthermore different kinds of simulations containing pure η signal were performed in order to investigate the production mechanism of the η meson. In the simulation, we assumed resonant production of the η meson via $pp \rightarrow N^*(1535)p \rightarrow pp\eta$. For the Dalitz decay, the Vector Dominance Model (VDM) was assumed, while for the 3-pion decay phase space production has been assumed. In addition, a full cocktail of reaction channels based on measured proton-proton cross sections was produced.

Tables 6.1 and 6.2 summarizes the reconstructed numbers of η mesons for simulation and experimental data from its two decay channels, before and after the kinematic fit.

before kinematic fit		
	$N_{\eta \rightarrow \pi^+ \pi^- \pi^0}$	$N_{\eta \rightarrow e^+ e^- \gamma}$
Sim	21568 ± 497	1678 ± 71
Exp	26265 ± 378	1141 ± 76

Table 6.1: Number of reconstructed η mesons before the kinematic fit.

after kinematic fit		
	$N_{\eta \rightarrow \pi^+ \pi^- \pi^0}$	$N_{\eta \rightarrow e^+ e^- \gamma}$
Sim	21841 ± 472	1573 ± 65
Exp	28460 ± 341	1034 ± 64

Table 6.2: Number of reconstructed η mesons after the kinematic fit.

Using the results from table 6.2 we can estimate the relative ratio of reconstructed η mesons from its two decay channels for simulation and experimental data:

$$R_{sim} = 13.9 \pm 0.65 \quad (6.1)$$

and

$$R_{exp} = 22.6 \pm 1.44 \quad (6.2)$$

where R_{exp} was calculated using formula 5.15.

If we would reconstruct the dileptons with 100% efficiency from experimental data compared to the simulation the numbers in expressions 6.1 and 6.2 would be the same; therefore the relative ratio of these numbers can be an estimation of the dilepton identification efficiency of the spectrometer in the η region. From numbers in expressions 6.1 and 6.2 one can conclude that in experimental data we can reconstruct only 62% of the η mesons compared to simulation.

Similarly using the numbers from table 6.1 we obtain:

$$R_{sim} = 12.8 \pm 0.62 \quad (6.3)$$

and

$$R_{exp} = 18.9 \pm 1.3 \quad (6.4)$$

Using these numbers we obtain that in experimental data we can reconstruct only 68% of the η mesons compared to the simulation. The systematic shift of 6% between the results before and after the kinematic fit algorithm is partly connected to the accuracy of background estimation. Another reason is the systematic shift of the pion mass as well as the background in the missing-mass distributions of two protons for the η Dalitz decay before the kinematic fit (See Figure 6.1(b)). Finally we can conclude that in the η region we can reconstruct only 62% of dileptons with a systematic shift of +6%.

The η meson reconstruction procedure is briefly discussed below (for more details see chapter 5).

The analysis has started with the selection of events with at least 3 positively charged particles and one negatively charged particle. During this step the candidates containing 3 positive and one negative particles were created by taking each time one of the positively charged particles to be e^+ if there was a matching with the RICH detector or π^+ in the other case. During this procedure the negative particle was assumed to be an electron or negative pion depending on the matching with the RICH detector (See for details section 5.3.1). For the reaction selection the missing-mass distributions of four particles were investigated. The missing-mass distribution of $pp\pi^+\pi^-$ shows an evident peak for π^0 corresponding to $\eta \rightarrow \pi^+\pi^-\pi^0$, as shown in Figure 5.11(a). After imposing a cut around the pion peak the events corresponding to the 3-pion decay of the η were selected. By imposing this cut we get rid of the events where no missing particle is present, corresponding to the reaction $pp \rightarrow pp\pi^+\pi^-$, in which we are not interested.

In a similar way, by plotting a missing-mass distribution of ppe^+e^- events one can see an evident peak for the missing photon centered at 0 (See Figure 5.11(b)); by putting a cut around the γ peak the events corresponding to the Dalitz decay of the η meson were selected.

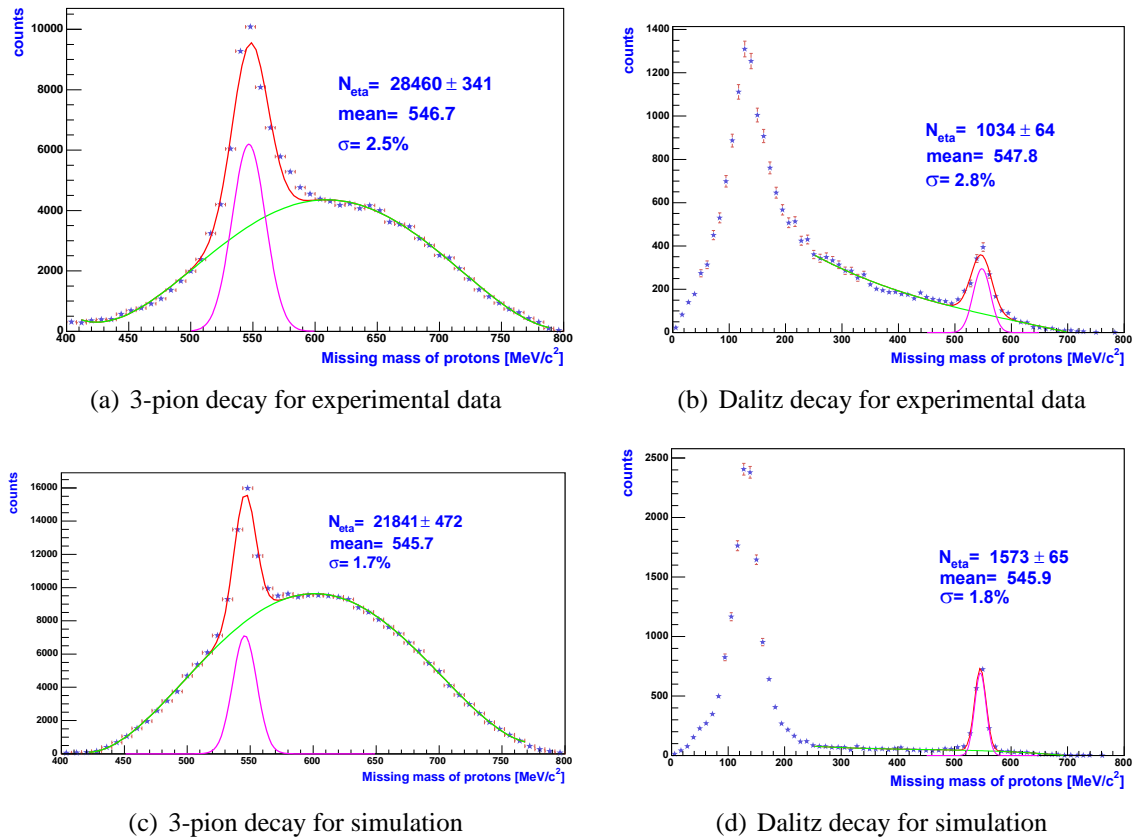


Figure 6.2: Missing-mass distributions of two protons after applying the kinematic fit algorithm; (a) for experimental data after applying a cut around π^0 peak in the missing-mass distributions of four particles, (b) for experimental data after applying a cut around γ peak in the missing mass distributions of four particles, (c) for simulation corresponding to the 3-pion decay of the η meson, and (d) for simulation corresponding to the Dalitz decay of the η meson.

After selecting the events corresponding to the above-mentioned two decay channels one can reconstruct the η mesons by plotting the missing-mass distributions of two protons. Figure 6.1(a) shows the missing mass distributions of two protons, after imposing a cut around π^0 peak in the missing-mass distribution of $pp\pi^+\pi^-$, corresponding to the 3-pion decay of the η meson. A prominent η peak, centered at the expected position, is clearly visible on top of a background coming mainly from non-resonant and resonant pion production. The η peak was fitted with a Gauss distribution plus a polynomial fit for the background. The number of reconstructed η mesons was estimated from the histogram counts above the background in Figure 6.1(a) due to the structure of the signal which can not be described by a Gauss function. This structure is due to the fact that the spectrometer was not fully set up at that time, and hence the reconstruction resolutions from the sectors with four and three MDC chambers are different. The reconstructed number of η mesons is equal to 26265 ± 378 . The η peak is centered around $553 \text{ MeV}/c^2$ with a resolution of 3.5%. In a similar way Figure 6.1(b) shows a missing-mass distribution of two protons after imposing a cut around the γ peak in the missing-mass distribution of ppe^+e^- , corresponding to the Dalitz decay of the η meson. The prominent peak centered around $549 \text{ MeV}/c^2$ corresponds to the reconstructed η mesons on top of the background coming mainly from multi-pion production. The reconstructed yield stems from two main mesons decays: the Dalitz decay of the type $X \rightarrow e^+e^-\gamma$ and two-photon decays $X \rightarrow \gamma\gamma$ followed by pair conversion of one of the decay photons (or both) in the target or by hitting some detector part. The yield was fitted with a Gauss distribution plus a polynomial fit for the background. The reconstructed number of η mesons from its Dalitz decay is equal to 1141 ± 76 . The η peak is centered around $549 \text{ MeV}/c^2$ with a resolution of 3.2%.

Figures 6.1(c) and 6.1(d) show the distributions of two-proton missing masses for 3-pion and the Dalitz decays of the η meson for simulation. The cuts imposed around the pion and photon peaks are the same in the simulation and experimental data. The reconstructed number of η mesons from the simulation is equal to 21568 ± 497 and 1678 ± 71 for its 3-pion and Dalitz decays, correspondingly. The width of the η signal is about 1.8%, both for the 3-pion and the Dalitz decays of the η meson for simulation.

In order to improve the tracking resolution and signal-to-background ratio, an algorithm of kinematic fit was developed using different constraints governing the decay processes. From a mathematical point of view the method varies the measured track parameters inside the corresponding error bars, until the required conditions are fulfilled. Only one condition was used for each decay channels: missing mass of four particles, $pp\pi^+\pi^-$, being equal to the π^0 mass for the 3-pion decay, and missing mass of ppe^+e^- being equal to 0 (photon mass). The method gives an improvement of the reconstructed mass resolution by a factor of 1.5 for the 3-pion and by a factor of 1.2 for the Dalitz decays of the η meson.

The obtained missing-mass distribution of two-protons for experimental data after the kinematic fit algorithm is shown in Figure 6.2(a) for 3-pion decay of the η meson. The η yield is fitted by a Gauss function plus a polynomial fit for a background. The reconstructed number of η mesons, performed by counting histogram counts above the background, is

equal to 28460 ± 341 . The η signal is centered around $547 \text{ MeV}/c^2$ with a resolution of 2.5%. Figure 6.2(b) shows the missing-mass distributions of two-protons for experimental data after the kinematic fit algorithm for the Dalitz decay of the η meson. The reconstructed number of the η mesons is equal to 1034 ± 64 . The η signal is centered around $547 \text{ MeV}/c^2$ with a resolution of 2.8%. The peak around $140 \text{ MeV}/c^2$ corresponds to the reconstructed π^0 mesons. As it is seen from Figure 6.2(b) the shift of the reconstructed π^0 mass observed in the two-proton missing-mass distributions before the kinematic fit algorithm (See Figure 6.1(b)) is gone after application of the kinematic fit algorithm. The corresponding two-proton missing-mass distributions for simulation are shown in Figures 6.2(c) and 6.2(d) for the 3-pion and the Dalitz decays of the η meson. The reconstructed numbers of the η mesons are equal to 21841 ± 472 and 1573 ± 65 for its 3-pion and the Dalitz decays, correspondingly.

6.0.2 η meson production

By fitting the pp missing-mass peak in various $\cos(\theta_{cm}^\eta)$ slices, the angular distribution of the η meson emission has been evaluated.

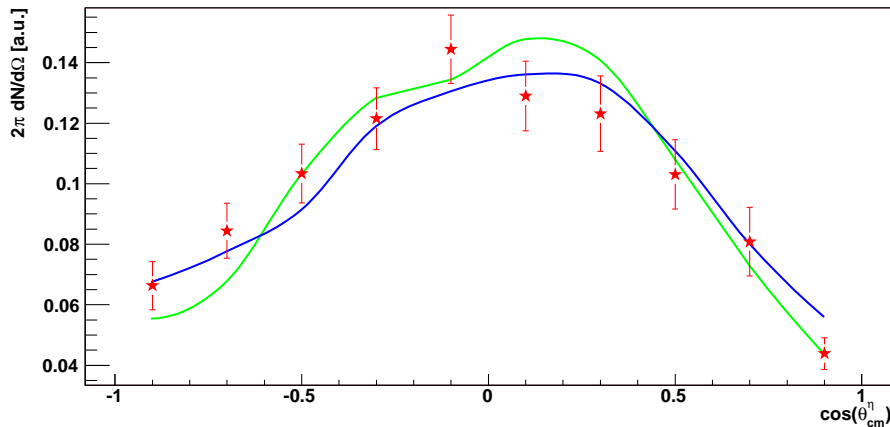


Figure 6.3: Angular distributions of η mesons in the center-of-mass system of the 2 protons. Red points are obtained from data, while blue and green lines are obtained from simulations through N_{1535}^* resonance with isotropic (blue) and anisotropic (green) angular distributions observed by the DISTO experiment.

In our simulations most of the parameters describing the η production and decay (matrix elements) have been fixed by information taken from other experiments. Therefore most of the degrees of freedom describing the $pp\eta$ final state are fixed (See section 5.2.1). Together with the fact that the beam axis has a rotational symmetry, only two angles are left for the alignment of the $pp\eta$ plane (See Figure 5.6). It was tested in simulations that

these parameters are not correlated, thus allowing us to compare directly 1-dimensional angular distributions without any multi-dimensional acceptance corrections.

The reconstructed angular distributions of the η mesons after the background subtraction is shown in Figure 6.3 (red points) together with two different model assumptions. Both models assume a production of the η meson through nucleon excitation $N^*(1535)$. In the first model (blue line) the isotropic η decay, while in the second model (green line) an anisotropic η decay observed by the DISTO experiment has been included. The results are consistent within the error bars with both models. The nice agreement between simulation and experimental distributions shows that the η mesons are mainly produced via $N^*(1535)$, as predicted by other experiments as well.

6.0.3 η meson decay

The Dalitz decay of the η meson was investigated by reconstructing the invariant-mass distribution of dileptons coming from the $\eta \rightarrow e^+e^-\gamma$ decay. To the η peak in the missing-mass distribution of two protons, besides the Dalitz decay of the η meson, the $\eta \rightarrow \gamma\gamma$ decay channel contributes as well. In order to suppress these events, several cuts have been used described in Section 5.4.4.

The matrix element of the Dalitz decay of the type $A \rightarrow Be^+e^-$ can be written as:

$$|M|^2 = |M(A \rightarrow B\gamma^*)|^2 \frac{1}{M^4} |M(\gamma^* \rightarrow e^+e^-)|^2. \quad (6.5)$$

This reflects in the differential decay rate, which can be written as a product of the conversion rate of the virtual gamma and the decay width $\Gamma_{A \rightarrow B\gamma^*}$ of A into a massive photon:

$$\frac{d\Gamma_{A \rightarrow Be^+e^-}}{dM} = \frac{2\alpha}{3\pi M} \sqrt{1 - \frac{4m_e^2}{M^2}} \left(1 + \frac{2m_e^2}{M^2}\right) \Gamma_{A \rightarrow B\gamma^*}. \quad (6.6)$$

the $A \rightarrow B\gamma^*$ width is given by

$$\Gamma_{A \rightarrow B\gamma^*} = \frac{|\vec{p}_{cm}|}{8\pi m_A^2} |M_{A \rightarrow B\gamma^*}|^2. \quad (6.7)$$

Here $|\vec{p}_{cm}|$ is the decay momentum

$$|\vec{p}_{cm}| = \frac{\lambda^{\frac{1}{2}}(m_A^2, m_B^2, M^2)}{2m_A} \quad (6.8)$$

with the kinematic function

$$\lambda(x^2, y^2, z^2) = (x^2 - (y+z)^2)(x^2 - (y-z)^2). \quad (6.9)$$

The matrix element $|M_{A \rightarrow B\gamma^*}|$ can be calculated as:

$$|M_{A \rightarrow B\gamma^*}|^2 = \frac{1}{2} |f_{AB}(M^2)|^2 \lambda(m_A^2, m_B^2, M^2). \quad (6.10)$$

The form factor $f_{AB}(M^2)$ is introduced to account for the strong interaction part of the vertex. It is common to normalize to the decay width into real photons:

$$\Gamma_{A \rightarrow B\gamma} = \frac{(m_A^2 - m_B^2)^3}{32\pi m_A^3} |f_{AB(0)}|^2, \quad (6.11)$$

which re-expresses the form factor to

$$F_{AB}(M^2) = \frac{f_{AB}(M^2)}{f_{AB(0)}} \quad (6.12)$$

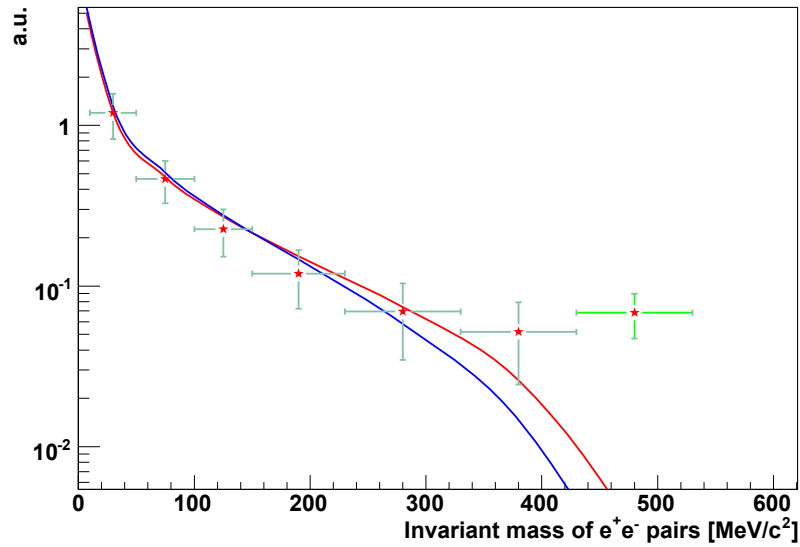
The form factor can be obtained from the vector meson dominance model (VDM). The following parametrization of the form factor of the η meson is commonly used:

$$F_\eta(M^2) = \left(1 - \frac{M^2}{\Lambda_\eta^2}\right)^{-1} \quad (6.13)$$

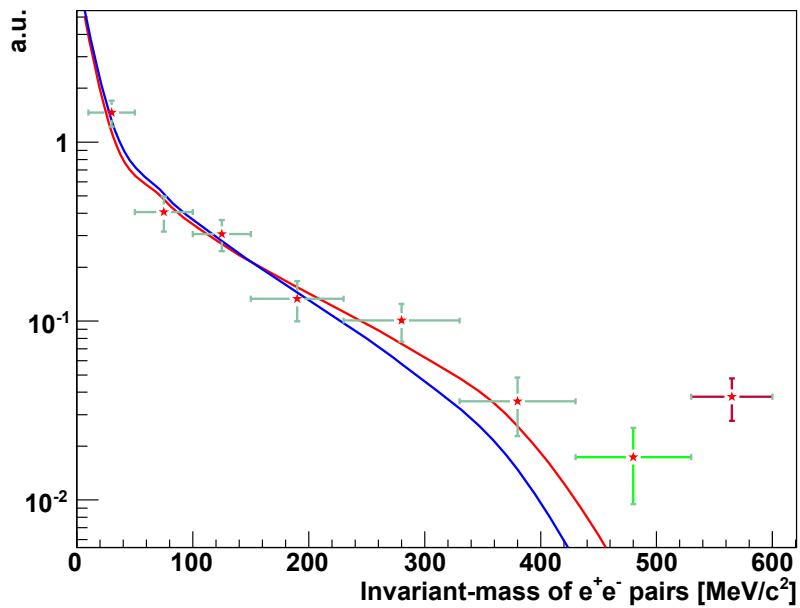
with $\Lambda_\eta=0.72$ GeV.

Figure 6.4(a) shows the reconstructed invariant-mass distribution of e^+e^- pairs from η Dalitz decay after background subtraction. The red line corresponds to the calculations with Equation 6.6 with the form factor parameterized by formula 6.13. The blue line corresponds to the pure QED calculations which is obtained also from formula 6.6 by putting the form factor equal to 1.

As it is seen from the Figure, within error bars, the VDM model describes the decay quite well. The discrepancy of the last bin from the VDM calculations was investigated using different methods for background subtraction. These investigations have shown that two different methods are giving similar results. It was shown that the background behavior in this bin can not be easily described. Therefore the discrepancy is coming from the inaccuracy of the background estimation in this bin. By reconstructing the e^+e^- invariant-mass distribution from the simulation (See Figure 6.4(b)), it was found that this bin has a similar behavior. As in the simulation we assumed the decay with VDM hypothesis the discrepancy may come only from the background estimation or fake track contributions.



(a) real data



(b) simulation

Figure 6.4: Invariant-mass distribution of e^+e^- pairs from the Dalitz decay of the η meson for real data (a) and for simulation (b). Red line corresponds to the VDM model calculations, while the blue line represents the pure QED calculations.

By comparing the e^+e^- invariant-mass distributions from simulation and experimental data, it was realized that in case of simulation there are pairs with invariant masses around the pole mass of the η meson (See Figure 6.4(b))¹. These pairs correspond to the direct decays of the η meson which is suppressed. The fact that these counts do not exist in the e^+e^- invariant-mass distribution from experimental data (See Figure 6.4(a)), together with the fact that the analyzed statistics is more for experimental data shows that the lower limit on the branching ratio of the $\eta \rightarrow e^+e^-$ decay channel is lower, than presented in [76]. One should mention that in simulation for the direct decay of the η mesons into e^+e^- pairs the branching ratio was taken from [76].

In 2007 a proton-proton run at 3.5 GeV will be taken with much more statistics. During this run the main emphasis will be put to the investigation of the ω meson decay. Furthermore the investigation of the η Dalitz decay will be repeated with high statistics as well with that data.

This investigation has shown that the HADES spectrometer can be used to investigate elementary collisions as well. The high resolution tracking which uses information from all four MDCs, is working properly. However, there are still some problems especially concerning the alignment of the magnetic field which are under investigation.

6.0.4 Investigation of the spectrometer performance using elastic scattering

The elastic proton-proton scattering was investigated to understand the spectrometer performance in terms of alignment and reconstruction resolution. The reaction selection is based on the kinematics of the elastic scattering (See section 4.2). As the kinematics of the elastic scattering is fully characterized by two parameters (See section 4.1), it was possible to estimate the momentum reconstruction resolution of the spectrometer in each sector separately by measuring the polar angle of the track and comparing the reconstructed momentum with the calculated one from kinematical relations (See Appendix B). The elastic scattering is also used to investigate the alignment of the magnetic coils with respect to MDC chambers. For the sectors equipped with all four MDC chambers the momentum resolution obtained from these analyzes is about 4% on average (See Figures 4.6). For the sector with 3 MDC chambers, the obtained momentum resolution is about 7%. However these resolutions are also affected by angular resolution as well, because for calculation of the momentum using elastic scattering kinematics the angular information is used (See appendix B). Furthermore the resolutions are obtained for the momentum range between 600MeV/c to 2500 MeV/c. The obtained resolution distributions have shown systematic shifts as a function of sector numbers as shown in Figures 4.7. This indicates that the alignment procedure must still be improved.

¹For details see section 5.7.

Appendix A

Lorentz transformations

A relativistic particle is fully characterized by its mass m and velocity β . The energy E and momentum \mathbf{p} are defined as:

$$E = \frac{m}{\sqrt{1 - \beta^2}} = m\gamma \quad (\text{A.1})$$

$$\mathbf{p} = \frac{m\beta}{\sqrt{1 - \beta^2}} = m\beta\gamma \quad (\text{A.2})$$

where $\gamma = \frac{1}{\sqrt{1 - \beta^2}}$

There is another representation of β , γ and η with hyperbolic functions:

$$\begin{aligned} \beta &= \tanh y \\ \gamma &= \cosh y \\ \eta &= \sinh y \end{aligned} \quad (\text{A.3})$$

with $\eta = \gamma\beta$

Let us define a 4-vector as

$$p = \begin{pmatrix} E \\ p_x \\ p_y \\ p_z \end{pmatrix} \quad (\text{A.4})$$

where E and \vec{p} are the energy and 3-momentum of a particle in the LAB frame.

The energy and momentum (E^*, \vec{p}^*) viewed from the CM frame which is moving with a velocity β_{cm} in z direction are given by

$$\begin{pmatrix} E^* \\ p_x^* \\ p_y^* \\ p_z^* \end{pmatrix} = \begin{pmatrix} \gamma & 0 & 0 & -\gamma\beta \\ 0 & 1 & 0 & 0 \\ 0 & 0 & 1 & 0 \\ -\gamma\beta & 0 & 0 & \gamma \end{pmatrix} \begin{pmatrix} E \\ p_x \\ p_y \\ p_z \end{pmatrix} \quad (\text{A.5})$$

For the backward transformation, i.e from CM frame to LAB, one should use instead of β_{cm} a $-\beta_{cm}$ in A.5

$$\begin{pmatrix} E \\ p_x \\ p_y \\ p_z \end{pmatrix} = \begin{pmatrix} \gamma & 0 & 0 & \gamma\beta \\ 0 & 1 & 0 & 0 \\ 0 & 0 & 1 & 0 \\ \gamma\beta & 0 & 0 & \gamma \end{pmatrix} \begin{pmatrix} E^* \\ p_x^* \\ p_y^* \\ p_z^* \end{pmatrix} \quad (\text{A.6})$$

Taking into account relations A.3 one can write the above transformation as:

$$\begin{pmatrix} E \\ p_x \\ p_y \\ p_z \end{pmatrix} = \begin{pmatrix} \cosh y & 0 & 0 & \sinh y \\ 0 & 1 & 0 & 0 \\ 0 & 0 & 1 & 0 \\ \sinh y & 0 & 0 & \cosh y \end{pmatrix} \begin{pmatrix} E^* \\ p_x^* \\ p_y^* \\ p_z^* \end{pmatrix} \quad (\text{A.7})$$

From a geometrical point of view Lorentz transformations are rotations in Ep_x , Ep_y , Ep_z planes. In our particular case, when the CM frame moves in z direction, the Lorentz transformation can be represented by a rotation in the Ep_z plane by an angle χ defined as:

$$\tanh \chi = i\beta \quad (\text{A.8})$$

Since $\tanh y = \beta$, an angle χ is related to rapidity as: $\chi = iy$

In practice it is sometimes useful to decompose momentum into two components: longitudinal p_{\parallel} (along β direction) and transverse p_{\perp} (perpendicular to β direction).

$$\begin{aligned} p &= p_{\parallel} + p_{\perp} \\ p^* &= p_{\parallel}^* + p_{\perp}^* \end{aligned} \quad (\text{A.9})$$

In these notations 4-momenta are written as:

$$\begin{pmatrix} E \\ 0 \\ p_{\perp} \\ p_{\parallel} \end{pmatrix} = \begin{pmatrix} E \\ 0 \\ p \sin \theta \\ p \cos \theta \end{pmatrix} \quad (\text{A.10})$$

where θ is the angle between the momentum vector and β in corresponding reference system. In other words, we did a transformation into spherical coordinates (p, θ, ϕ) .

The azimuthal angle under Lorentz transformation is not changing.

$$\phi = \phi^* \quad (\text{A.11})$$

From A.6 we have

$$\begin{pmatrix} E \\ 0 \\ p_{\perp} \\ p_{\parallel} \end{pmatrix} = \begin{pmatrix} \gamma & 0 & 0 & \gamma\beta \\ 0 & 1 & 0 & 0 \\ 0 & 0 & 1 & 0 \\ \gamma\beta & 0 & 0 & \gamma \end{pmatrix} \begin{pmatrix} E^* \\ 0 \\ p_{\perp}^* \\ p_{\parallel}^* \end{pmatrix} \quad (\text{A.12})$$

Appendix B

Kinematics of elastic scattering

Here we will derive some important kinematical relations for elastic scattering in both laboratory (LAB) and center-of-mass frames (CM).

The reference system attached to the laboratory of the user is called LAB system. Sometimes in the experiment the beam of particles is directed onto the target at rest, therefore the LAB system will be just the rest system of a target particle.

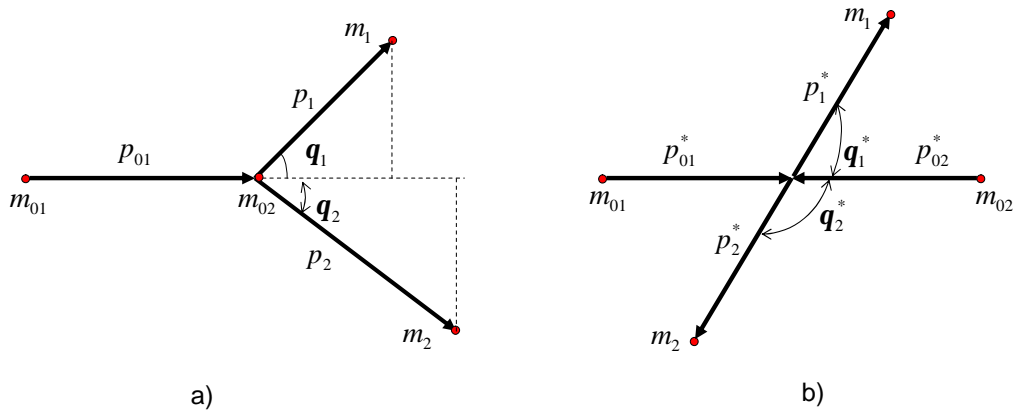


Figure B.1: Kinematics of elastic scattering in (a) LAB and (b) center of mass system of two protons.

The second most often used system is the center-of-mass system where the vector sum of all momenta particles taking part in a reaction equals 0.

The motion of the center of mass system of particles is equivalent to the motion of some quasi particle with an energy:

$$E = \sum E_i \tag{B.1}$$

and momentum

$$p = \sum p_i \quad (\text{B.2})$$

with the mass being equal to the total center-of-mass energy

$$M = S = \sqrt{\left(\sum E_i\right)^2 - \left(\sum p_i\right)^2} \quad (\text{B.3})$$

giving

$$\beta_{cm} = \frac{p}{E} = \frac{\sum p_i}{\sum E_i} \quad (\text{B.4})$$

Let us derive some kinematic relations for the reaction

$$a_{01} + a_{02} = a_1 + a_2 \quad (\text{B.5})$$

with four momentum being p_{01}, p_{02}, p_1 , and p_2 respectively. In addition we will assume that in B.5 that all particles are identical with mass m .

In the CM frame, from momentum conservation law we have:

$$\begin{aligned} E_1^* + E_2^* &= M \\ \vec{p}_1^* + \vec{p}_2^* &= 0 \end{aligned} \quad (\text{B.6})$$

with M defined in B.3. The second line of B.6 tells us that in CM frame the outgoing particles have the same momentum moving in opposite directions.

from B.1,B.2,B.3,B.4 one can easily get

$$\begin{aligned} S &= \sqrt{2m(E_{01} + m)} \\ \beta_{cm} &= \frac{p_{01}}{E_{01} + m} = \sqrt{\frac{\gamma_{01} - 1}{\gamma_{01} + 1}} \\ \gamma_{cm} &= \sqrt{\frac{E_{01} + m}{2m}} = \sqrt{\frac{\gamma_{01} + 1}{2}} \end{aligned} \quad (\text{B.7})$$

The relation between momenta and energies of the particles in these two reference systems are:

$$\begin{aligned} E_{01}^* = E_{02}^* &= \frac{\sqrt{s}}{2} = \sqrt{\frac{m(E_{01} + m)}{2}} = m * \gamma_{cm} \\ p_{01}^* = p_{02}^* &= \sqrt{\frac{m(E_{01} - m)}{2}} = m \sqrt{\frac{\gamma_{01} - 1}{2}} \end{aligned} \quad (\text{B.8})$$

From A.6 and A.9 we have

$$\begin{aligned} p_{\parallel} &= p \cos(\theta) = \gamma p^* \cos \theta^* + \gamma \beta E^* \\ p_{\perp} &= p \sin \theta = p^* \sin \theta^* \end{aligned} \quad (\text{B.9})$$

It is clear from the definitions of p_{\parallel} and p_{\perp} that

$$\tan \theta = \frac{p_{\perp}}{p_{\parallel}} \quad (\text{B.10})$$

Taking into account B.9 in B.10 we have

$$\tan \theta = \frac{p^* \sin \theta^*}{\gamma_{cm}(p^* \cos \theta^* + \beta_{cm} E^*)} = \frac{1}{\gamma_{cm}} \frac{\sin \theta^*}{\cos \theta^* + \frac{\beta_{cm}}{\beta^*}} \quad (\text{B.11})$$

In elastic scattering of identical particles $\frac{\beta_{cm}}{\beta^*} = 1$ therefore we can rewrite B.11 as:

$$\tan \theta_1 = \frac{1}{\gamma_{cm}} \frac{\sin \theta^*}{1 + \cos \theta^*} = \frac{1}{\gamma_{cm}} \tan \frac{\theta_1^*}{2} \quad (\text{B.12})$$

$$\tan \theta_2 = \frac{1}{\gamma_{cm}} \tan\left(\frac{\pi}{2} - \frac{\theta_1^*}{2}\right) = \frac{1}{\gamma_{cm}} \coth \frac{\theta_1^*}{2}$$

In B.12 the relation $\theta_1^* + \theta_2^* = \pi$ was taken into account (See Figure B.1)
Multiplication of the two lines in B.12 gives

$$\tan \theta_1 * \tan \theta_2 = \frac{1}{\gamma_{cm}^2} \quad (\text{B.13})$$

One can write the momentum conservation law for the reaction B.5 as :

$$\begin{aligned} p_1 \sin(\theta_1) - p_2 \sin(\theta_2) &= 0 \\ p_1 \cos(\theta_1) + p_2 \cos(\theta_2) &= p_{01} \end{aligned} \quad (\text{B.14})$$

solving this equations against p_1 yields:

$$p_1 = \frac{p_{01}}{\cos \theta_1} - \frac{p_1 \tan^2 \theta_1}{\tan \theta_2 \tan \theta_1} \quad (\text{B.15})$$

Finally taking into account B.13 in B.15 we can express the momentum of the outgoing particle as a function of its polar angle:

$$p_1 = \frac{p_{01}}{\cos(\theta_1) [1 + \tan^2(\theta_1) \gamma_{cm}^2]} \quad (\text{B.16})$$

Appendix C

Formulas for kinematic fit

From a mathematical point of view the kinematic fit means finding of a parameters $\tilde{\alpha}$ which gives a minimum of the function:

$$F_1 = \sum_{i=1}^n (\alpha_i - \tilde{\alpha}_i)^T W^{-1} (\alpha_j - \tilde{\alpha}_j) + \sum_{k=1}^s \lambda_k H_k \quad (\text{C.1})$$

where W^{-1} is the inverse of the measured covariance matrix, sometimes referred to as a weight matrix, α and $\tilde{\alpha}$ are track parameters before and after the kinematic fit algorithm, H_k are constraint equations and λ_k are Lagrange multipliers.

The minimization procedure consists of two steps:

- Finding of a first approximation for parameters
- Using least squares fit with constraints to minimize the function C.1

In order to find a first approximation for the track parameters we use so called helper function defined as:

$$F_2 = \sum_{i=1}^n \left(\frac{\alpha_i - \alpha_i(T)}{\sigma_{\alpha_i}} \right)^2 + T \sum_{k=1}^s \frac{H_k^2}{(\Delta H_k)^2} \quad (\text{C.2})$$

where $(\Delta H_k)^2$ is:

$$(\Delta H_k)^2 = \sum_{i=1}^{i=N} \left(\frac{\partial H_k}{\partial \alpha_i} \sigma_{\alpha_i} \right)^2 \quad (\text{C.3})$$

and parameter T is fixed according to the reaction channel under investigation.

When $T \rightarrow \infty$ the minimum of functions C.1 and C.2 can be described by the same set of parameters α_i . That is why it is assumed that the parameters corresponding to the

minimum of function C.1 will be in close vicinity of the parameters found by minimization of the helper function C.2.

The minimization procedure is based on least squares fitting with constraints, according to which the minimum of the function C.1 can be found by equating of all the partial derivatives of the function C.1 with respect to each parameter to 0:

$$\frac{\partial F_1}{\partial \alpha_i} = 0 \quad (\text{C.4})$$

We will derive the formulas by taking into account only diagonal elements of a covariance matrix.

We can write the conditions C.4 in a matrix form as:

$$\begin{pmatrix} \frac{1}{(\sigma_{\alpha_1})^2} & 0 & \dots & 0 & 0 \\ 0 & \frac{1}{(\sigma_{\alpha_2})^2} & \dots & 0 & 0 \\ \dots & \dots & \dots & \dots & \dots \\ \dots & \dots & \dots & \dots & \dots \\ \dots & \dots & \dots & \dots & \dots \\ 0 & 0 & \dots & \frac{1}{(\sigma_{\alpha_{n-1}})^2} & 0 \\ 0 & 0 & \dots & 0 & \frac{1}{(\sigma_{\alpha_n})^2} \end{pmatrix} \begin{pmatrix} \alpha_1 - \tilde{\alpha}_1 \\ \alpha_2 - \tilde{\alpha}_2 \\ \dots \\ \dots \\ \dots \\ \alpha_{n-1} - \tilde{\alpha}_{n-1} \\ \alpha_n - \tilde{\alpha}_n \end{pmatrix} = \begin{pmatrix} \lambda_k \frac{\partial H_k}{\partial \alpha_1} \\ \lambda_k \frac{\partial H_k}{\partial \alpha_2} \\ \dots \\ \dots \\ \dots \\ \lambda_k \frac{\partial H_k}{\partial \alpha_{n-1}} \\ \lambda_k \frac{\partial H_k}{\partial \alpha_n} \end{pmatrix} \quad (\text{C.5})$$

Let us denote by $\alpha_i(T)$ the values of the parameters giving the minimum of the helper function C.2. As it was stated before these parameters can be considered as a first approximation for the minimum of the function C.1. Therefore we can use a Taylor expansion for the constraints around these parameters:

$$H_k(\tilde{\alpha}_1, \tilde{\alpha}_1, \dots, \tilde{\alpha}_n) = H_k(T) + \sum_{i=1}^n \frac{\partial H_k}{\partial \alpha_i} (\tilde{\alpha}_i - \alpha_i(T)) \quad (\text{C.6})$$

by definition we have

$$H_k(\tilde{\alpha}_1, \tilde{\alpha}_1, \dots, \tilde{\alpha}_n) = 0 \quad (\text{C.7})$$

hence,

$$H_k(T) = - \sum_{i=1}^n \frac{\partial H_k}{\partial \alpha_i} (\tilde{\alpha}_i - \alpha_i(T)) \quad (\text{C.8})$$

from Equations C.5 we have

$$\tilde{\alpha}_i = \alpha_i - \sum_{k=1}^{k=s} \lambda_k \frac{\partial H_k}{\partial \alpha_i} \sigma_i^2 \quad (\text{C.9})$$

Taking into account C.9 in C.8 we have

$$\sum_{i=1}^n \frac{\partial H_k}{\partial \alpha_i} \sum_{k=1}^s \lambda_k \frac{\partial H_k}{\partial \alpha_i} \sigma_i^2 = H_k(T) + \sum_{i=1}^n \frac{\partial H_k}{\partial \alpha_i} (\alpha_i - \alpha_i(T)) \quad (\text{C.10})$$

The last equation can be written as a set of linear equations, which can be solved with Cramer's determinants method against λ_k :

$$\lambda_k = \frac{|X(k)|}{|X|} \quad (\text{C.11})$$

where X is the matrix of coefficients of λ_k 's
and X(k) is obtained from X by substituting column number k with

$$H_k(T) + \sum_{i=1}^n \frac{\partial H_k}{\partial \alpha_i} (\alpha_i - \alpha_i(T)) \quad (\text{C.12})$$

By substituting found λ_k 's from C.11 into C.9 we define the parameters from kinematic fit.

Obtaining a solution is not enough: we also want to know the errors of the parameters. In order to find the uncertainty in the estimation of the parameters $\tilde{\alpha}$ in our fitting procedure, we use error propagation method. Each of our data points α has been used in the determination of the parameters and each has contributed some fraction of its own uncertainty to the uncertainty in our final determination.

$$\sigma_{\tilde{\alpha}_j}^2 = \sum_{i=1}^n \sigma_{\alpha_i}^2 \left(\frac{\partial \tilde{\alpha}_j}{\partial \alpha_i} \right) \quad (\text{C.13})$$

Appendix D

Data levels

The main goal of HADES software framework, is to reconstruct the events ¹ recorded by the HADES spectrometer which means an application of various algorithms to transform the *row* data delivered by the HADES into elaborated data, ready for the analysis steps.

The reconstruction proceeds in steps; each algorithm reads some input data may be the output from another algorithm, and takes it to a new level. In this sense we speak of different data levels. The first data level is the so called *raw* data, corresponding directly to the electronic signals recorded by the spectrometer. The next level is called calibrated data. The algorithm going from row data to calibrated data is detector specific and generally known as a *calibrator*.

The information obtained from MDCs are hardware addresses where the signal was generated and TDC counts. After the *unpacking*, a data level called *row* is filled. The next data level is called *MDCall* and is obtained from *raw* data level through a calibration procedure. The first calibration step translates the hardware addresses into module and cell numbers. The information from TDCs are transformed to drift times in nanoseconds using a linear function interpolation for extraction of a TDC gain from special calibration events. Besides of this in the calibration procedure the time offsets are also determined in order to remove from the measured time the part that does not correspond to the drift time (the part corresponding to time of flight of the particle) [77]. This offset subtraction was done in a global way for each TDC channel by fitting with the linear function the edge of the integrated time spectrum the crossing point of which with the integrated background as shown in Figure D.1 defines the global time offset; therefore the global offset correction removes from the measured drift time the time corresponding to the fastest particle which passes the cell closest to the wire.

During the track finding and fitting two things should be taken into account:

¹The event holds all the information collected by the different detectors in the spectrometer regarding one interaction between beam particle and the target; moreover it also stores the totally or partially reconstructed data which are derived from the original signal; there can be different kind of events: real events, simulated events, calibration events.

- propagation of the signal through wire
- the fact that all drift times are measured with respect to the fastest particle drift time

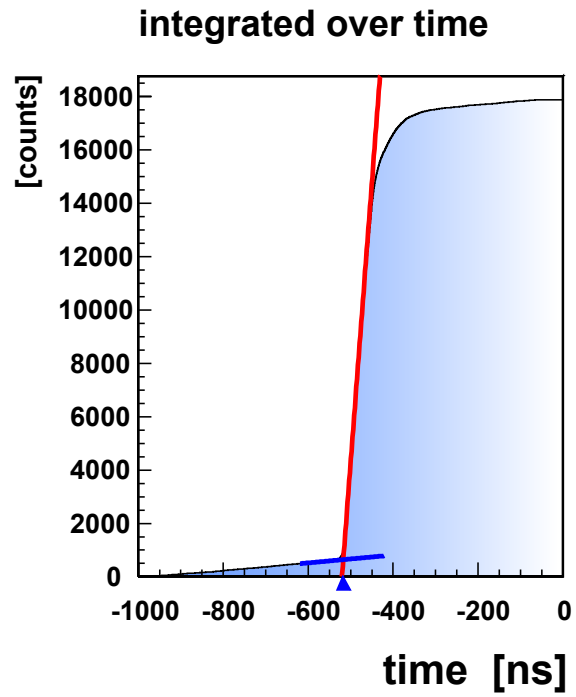


Figure D.1: Global time offset determination

Appendix E

Spline interpolation

As described in Section 3.8 we assume a cubic spline model for the track's second derivative, and as an input we take the following function

$$\frac{d^2Y}{dz^2} \equiv A(z)$$

with conditions

$$Y(z_0) = Y'(z_0) = 0$$

The Taylor series for a cubic polynomial $A(z)$ for interval $[z_i, z_{i+1}]$ expanded around the point z_i can be written as:

$$A(z) = A_i + (z - z_i) \frac{dA_i}{dz} + \frac{1}{2!} (z - z_i)^2 \frac{d^2A_i}{dz^2} + \frac{1}{3!} (z - z_i)^3 \frac{d^3A_i}{dz^3} \quad (\text{E.1})$$

where the function and derivatives are evaluated at z_i . The expression E.1 can be written in more concise way as

$$A(z) = A_i + (z - z_i)A'_i + \frac{1}{2}(z - z_i)^2A''_i + \frac{1}{6}(z - z_i)^3 \frac{(A''_{i+1} - A''_i)}{D_i} \quad (\text{E.2})$$

where A' and A'' stand for the first and second derivatives evaluated at $z = z_i$ and the third derivative has been replaced by its divided difference form, which is exact for a cubic function and $D_i = z_{i+1} - z_i$.

For $A(z)$ to be continuous we want

$$A_{i+1} = A_i + D_iA'_i + \frac{1}{2}D_i^2A''_i + \frac{1}{6}D_i^2(A''_{i+1} - A''_i) \quad (\text{E.3})$$

From the last equation we have

$$A'_i = \frac{A_{i+1} - A_i}{D_i} - \frac{1}{2}D_i A''_i - \frac{1}{6}D_i A''_{i+1} + \frac{1}{6}D_i A''_i \quad (\text{E.4})$$

And after some simplification of the last equation

$$A'_i = \frac{(A_{i+1} - A_i)}{D_i} - \frac{1}{3}D_i A''_i - \frac{1}{6}D_i A''_{i+1} \quad (\text{E.5})$$

Let us differentiate the equation E.2 at z_{i+1} (substitute z by z_{i+1} after differentiation)

$$A'_{i+1} = A'_i + \frac{1}{2}D_i A''_i + \frac{1}{2}D_i A''_{i+1} \quad (\text{E.6})$$

In the last equation we substitute an expression for A'_i from E.5 giving

$$A'_{i+1} = \frac{A_{i+1} - A_i}{D_i} - \frac{1}{3}D_i A''_i - \frac{1}{6}D_i A''_{i+1} + \frac{1}{2}D_i A''_i + \frac{1}{2}D_i A''_{i+1} \quad (\text{E.7})$$

On the other hand if we evaluate an expression E.5 at $i+1$ we have

$$A'_{i+1} = \frac{(A_{i+2} - A_{i+1})}{D_{i+1}} - \frac{1}{3}D_{i+1} A''_{i+1} - \frac{1}{6}D_{i+1} A''_{i+2} \quad (\text{E.8})$$

The left hand sides of E.7 and E.8 being equal we equate the write hand sides of them and take all differentials to one side

$$\frac{1}{6}D_i A''_i + A''_{i+1} \left(\frac{1}{3}D_i + \frac{1}{3}D_{i+1} \right) + \frac{1}{6}D_{i+1} A''_{i+2} = \left(\frac{A_{i+2} - A_{i+1}}{D_{i+1}} - \frac{A_{i+1} - A_i}{D_i} \right) \quad (\text{E.9})$$

Multiplication of the last equation by 3 and division by $(D_i + D_{i+1})$ yields

$$\frac{D_i}{2(D_i + D_{i+1})} A''_i + A''_{i+1} + \frac{D_{i+1}}{2(D_{i+1} + D_i)} A''_{i+2} = 3 \left(\frac{A_{i+2} - A_{i+1}}{D_{i+1}} - \frac{A_{i+1} - A_i}{D_i} \right) (D_i + D_{i+1})^{-1} \quad (\text{E.10})$$

The obtained equations E.10 are system of linear equations with the unknown second derivatives. As it can be seen from the expression we have $N-2$ equations and N second derivatives (unknowns). The equations can be solved as soon as we now the values of A''_1 and A''_N . One possibility is to set the second derivatives to 0 to obtain *natural splines*.

We choose for $A(x)$ the third order cubic spline so that we assume $A''_1 = A''_2$ and $A''_{N-1} = A''_N$. After this conditions we have N equations and N unknowns which can be solved by using Cramers Determinants method. The first derivatives are evaluated then using E.5. After substituting the found first and second derivatives into E.3 we have fully defined spline curve.

To evaluate the determinant each time may be time consuming therefore by taking $A''_i = P_i A''_{i+1} + Q_i$ we get the recursive relations from E.10

$$P_{i+1} = -t_2/(1 + t_1 P_i) \quad (\text{E.11})$$

$$Q_{i+1} = (R_i - t_1 Q_i)/(1 + t_1 P_i)$$

where

$$\begin{aligned} t_1 &= D_i [2(D_i + D_{i+1})]^{-1} \\ t_2 &= D_{i+1} [2(D_i + D_{i+1})]^{-1} \end{aligned} \quad (\text{E.12})$$

and R_i the right hand side of E.10. Starting with $P_1 = 1, Q_1 = 0$ and the equations E.10 can now be solved and then A_i'' can be determined from E.11 starting with $A_N'' = Q_{N-1}(1 - P_{N-1})^{-1}$.

E.1 Solution of field equations using cubic spline

To solve the field equations

$$p \frac{d^2 y}{dz^2} = k(z) \left[B_x \left(1 + \left(\frac{dy}{dz} \right)^2 \right) - B_y \frac{dx}{dz} \frac{dy}{dz} - B_z \frac{dx}{dz} \right] \quad (\text{E.13})$$

$$p \frac{d^2 x}{dz^2} = k(z) \left[B_x \frac{dy}{dz} \frac{dx}{dz} - B_y \left(1 + \left(\frac{dx}{dz} \right)^2 \right) + B_z \frac{dy}{dz} \right]$$

we perform a cubic spline fit on the evaluated right hand sides of E.13 as in E.2 with the aim to calculate the double integrals

$$Y(z_i) = \int_{u=z_0}^{u=z_i} \left[\int_{v=z_0}^{v=u} A(v) dv \right] du \quad (\text{E.14})$$

$$X(z_i) = \int_{u=z_0}^{u=z_i} \left[\int_{v=z_0}^{v=u} C(v) dv \right] du$$

Here we will show the solution only for the first integral of E.14. The second one is obtained in analogous way.

To get the first integrals $\int A(z) dz = Y'(z)$ integrate E.2 for corresponding functions $A(z)$ and after elimination of A' using E.5 we get

$$Y'_{i+1} = Y'_i + \frac{1}{2} D_i (A_{i+1} + A_i) - \frac{1}{24} D_i^3 (A_i'' + A_{i+1}'') \quad (\text{E.15})$$

with $Y'_1 = 0$.

To get the double integral we integrate E.2 for corresponding functions twice and after eliminations of A' according to E.5 we get

$$Y_{i+1} = Y_i + Y'_i D_i + \frac{1}{6} D_i^2 (2A_i + A_{i+1}) - \frac{1}{36} D_i^4 (0.8A_i'' + 0.7A_{i+1}'') \quad (\text{E.16})$$

with $Y_1 = 0$.

Appendix F

Software implementation

The software framework of the HADES spectrometer is called HYDRA. It is developed using the Object Oriented C++ programming language. The central class of the Hydra framework is the HADES class which encapsulates the whole reconstruction program, coordinating all Hydra subsystems. There must be one and only one instance of this class active at the same time. There are two ways to access this object, either by the *gHADES* global pointer or the *HADES::instance()* method¹. This class contains objects of different classes which it uses to implement the different subsystems. Since the reconstruction process is done event per event, the basic data structure is the event. An event is represented by an *HEvent* object. Within the *HEvent* data are organized in categories which are containers of objects. In this sense the *HEvent* is the container of categories. When we speak about a category of a given class, we mean the container holding the instances of that class. The interface for accessing the data inside categories is defined by the *HCategory* abstract class, all the other categories being inherited from this class. The *HCategory* interface provides different functions to access the data inside the categories

- Random access
- Sequential access

The random access means that one can access one particular object inside the category. Each object in the category is identified by an array of integers which are presented as an object inheriting from *HLocation* class. The corresponding function in the interface is *HCategory::getObject(HLocation & loc)*. It is also possible to access one object in the category giving only one index with the function *HCategory::getObject(int index)*.

Sequential access means to loop over a set of objects in the category and is performed using iterators. Iterators are objects created from the categories themselves by invoking the *HCategory::makeIterator()* method. The method *HIterator::Next()* keeps returning one

¹The second one is recommended.

object after the other in the container, until no objects are left and from there on it returns NULL.

For each event certain algorithm is performed (e.g. track finding, track fitting, momentum reconstruction and so on) which will be given a common name, task, represented by an *HTask* object. *HReconstructor* and *HTaskset* are two particular subclasses inheriting from *HTask*. The first one is meant for reconstruction algorithms, while the second one allows to group several tasks into one.

From a software point of view the main task for the track finder is *HMdcTrackFinder* which inherits from *HReconstructor* and takes an input information from category of *HMdcCall* class as it is shown in Figure F.1. The constructor of the *HMdcTrackFinder* class allows to set the mode of the track finder. In addition to that one more parameter can be set depending on whether the magnetic field was switched on or not. The task calculates the level of cluster finder as well, which can also be changed externally using corresponding methods provided by the class. The information about found clusters is stored in the *cat-MdcClus* category which stores instances of the *HMdcClus* class. The *HMdcClusterToHit* task fills the categories of the *HMdcSeg* and *HMdcHit* classes. The object of the *HMdcSeg* class contains all information about the track position in space. Using this information the intersection points with the mid planes of each chamber together with the hit directions (if the chamber is existing in the setup) are calculated and stored in the *HMdcHit* category, therefore, in some sense, these categories store the same information in different formats.

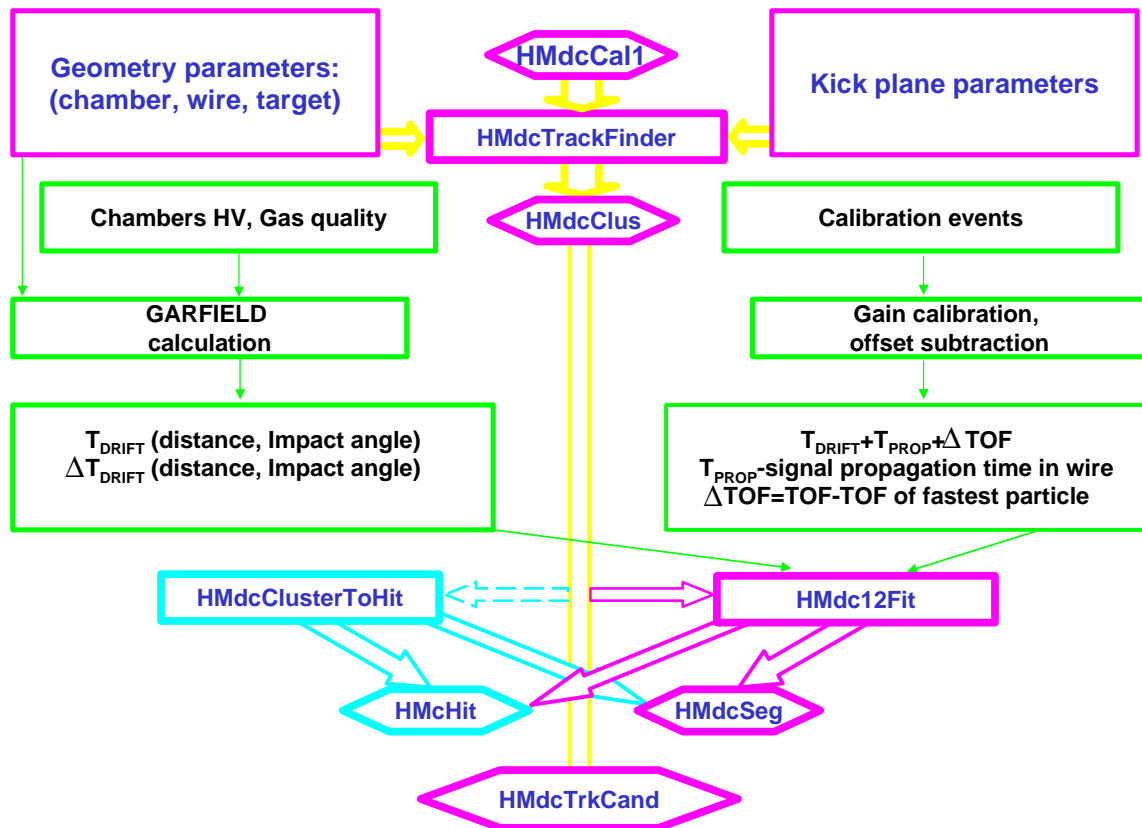


Figure F.1: Block diagram for track finder and fitter.

The track segment fitting is done with the task *HMdc12Fit* which takes the input from *HMdcClus* and fills the categories of *HMdcSeg* and *HMdcHit* classes. If the track was fitted the information in *HMdcSeg* and *HMdcHit* is updated with the fitted values, otherwise the information is left from cluster finder. The corresponding quality parameter of the track fitter, the χ^2 of the fit, is also a data member of the *HMdcSeg* class, whose value is set to -1 if it was decided that the fitting procedure has failed.

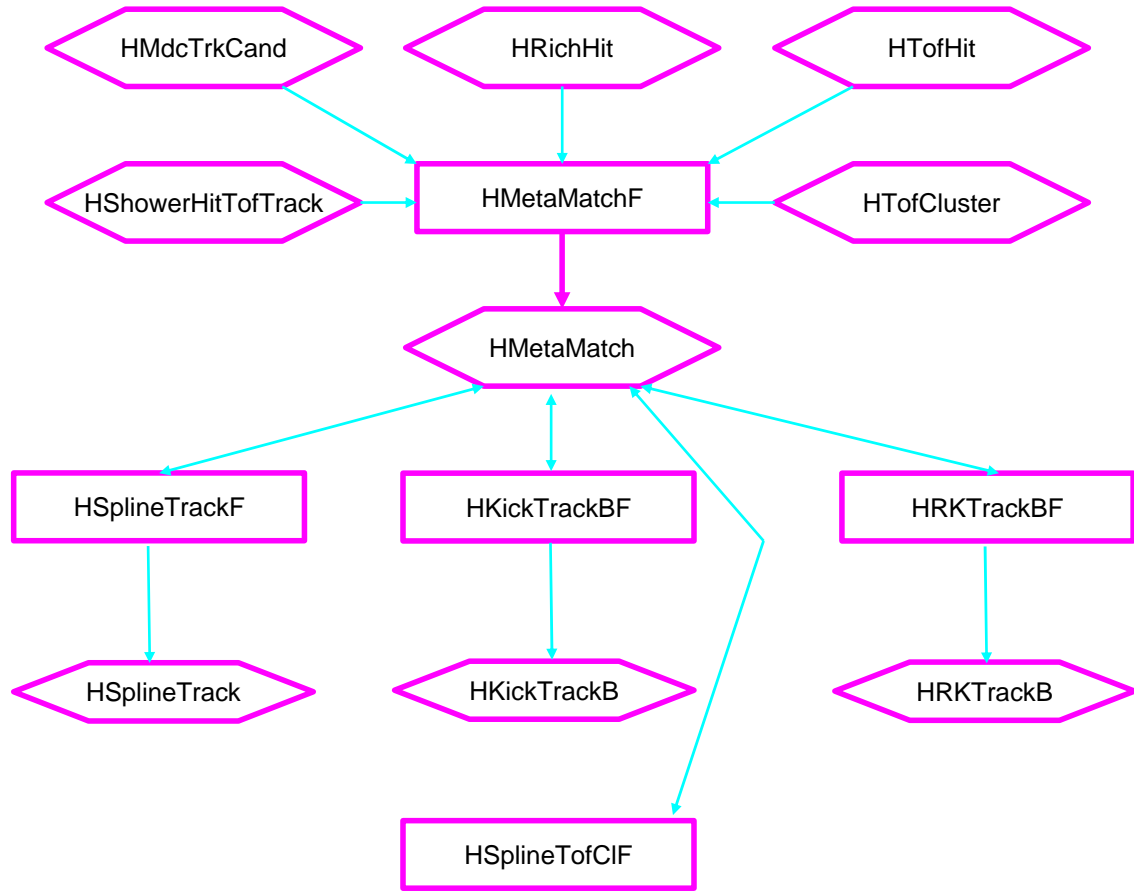


Figure F.2: Block diagram of matching code.

The matching code takes input information from the categories of *HMdcTrackCand* class which stores the indices of matched inner and outer segments in the category of *HMdcSeg* class, *HRichHit*, *HTofHit*, *HShowerHitTofTrack* storing the reconstructed hits from corresponding detector systems. The information about the tof clusters it takes from the category of *HTofCluster* class (See Figure F.2).

The main task for matching is called *HMetaMatchF* which performs an algorithm discussed in section 3.6 and creates the objects on *HMetaMatch* class.

As was explained before, e.g. in case of matching of track candidates with the META hits, one track candidate can match with several META hits as shown in Figure 3.8(a). In this case several instances of the *HMetaMatch* class will be created having the same track candidate (same inner and outer segments). Each instance of *HMetaMatch* object (yellow and green one in the Figure 3.8(a)) has a method for getting the first created object. (*HMetaMatch::getFirstTrackCand()* method). From the first object (green in Figure 3.8(a))

it is possible to obtain the next object by *HMetaMatch::getNextTrackCand()* method (the yellow in Figure 3.8(a)). For the last object the *HMetaMatch::getNextTrackCand()* returns -1. Furthermore, using the method *HMetaMatch::getNtrackCand()* it is possible to see how many times the given track candidate was matched with different META hits. The usefulness of this approach is that if, for example, one wants to calculate the momentum of the track for the *HMetaMatch* objects created in Figure 3.8(a) it is enough to calculate the momentum only for the first of them, as they have the same inner and outer segments. For the next objects it is enough only to recalculate the beta and path length of the track.

There are also methods giving a possibility to check how many times a given META hit was used with different track candidates and the corresponding methods for getting the next one.

If the matching with the META hit is done, the corresponding method *HMetaMatch::getSystem()* returns the value of 0 or 1 depending on whether the matching was done with SHOWER or TOF detectors correspondingly. In case of not matched META hits this method returns a value of -1.

The object of *HMetaMatch* keeps indices of all hits from different detector systems belonging to a given track. Furthermore it keeps matching qualities described in section 3.6.

The reconstruction of momentum starts taking an input information from the category of *HMetaMatch* class.

As there are several objects created from different momentum reconstruction methods and having the same data members the base class called *HBaseTrack* was created from which all the classes keeping an information about reconstructed momentum are inheriting.

The method of spline takes its input from the category of *HMetaMatch* class. The task which performs the momentum reconstruction is called *HSplineTrackF*. It calculates the momentum of the particle and the sign of the charge from inner and outer segments. If there is a matching with the META detectors the method calculates the path length and the velocity of the particle as well. The output is written to the category of *HSplineTrack* class which keeps the created objects of *HSplineTrack* class. The algorithm puts back into the *HMetaMatch* object (from which it has started) the index of the spline object in the category. If the object was created the corresponding method *HMetaMatch::isSplineAccepted()* is activated.

The algorithm of Runge Kutta is executed after the spline task. It starts from *HMetaMatch* objects which already have an index to the category of *HSplineTrack* from where the initial momentum and the polarity information can be taken. The angular information it takes using the index of *HMdcTrackCand* object which in turn keeps an index of *HMdcSeg* object. The output is written to *HRKtrackB* objects which are kept in the category of *HRKtrackB* class. The corresponding index of the created object in the category is written to the *HMetaMatch* object and the flag *HMetaMatch::isRungeAccepted()* is activated.

After the momentum reconstruction methods, the tof clustering task is running. This task takes care of Tof clusters and overlap between TOF and Shower detectors. In its

current design the task deactivates the corresponding *HMetaMatch::isAccepted()* flags for different methods for Tof hits entering the cluster and for SHOWER hits which are overlapping with Tof hits.

In order to keep compatibility with the kick plane algorithm, which works in case if there are no outer MDC chambers in the sector, the *HMetaMatch* objects are created even for the inner segments only (without outer segment). The kick plane algorithm has its own method of matching of segments with the *META* hits. The created objects from the kick plane method are compared with the objects of *HMetaMatch* class until the corresponding object is found. The index of the created *HKickTrackB* object is written to the *HMetaMatch* object. The corresponding flag of *HMetaMatch::isKickAccepted()* is set to true.

From a final user point of view the *HMetaMatch* object contains all necessary information for further analysis. By iteration over the category of the *HMetaMatch* class it is possible to obtain all necessary information for analysis. The example below shows how to obtain the momentum of the particle reconstructed by the spline method from *HMetaMatch* objects.

```

\\Retrieve a pointer to the categories
HEvent *event=HADES::instance()->GetCurrentEvent();
HCategory *cat=event->GetCategory(catMetaMatch);
HCategory *catSpline=event->GetCategory(catSpline);
Int_t splineInd=-1;
HSplineTrack *pSpline=NULL;
\\iterate over whole category
HIterator *iter=cat->MakeIterator();
iter->Reset();
HMetaMatch *temp=NULL;
while((temp=(HMetaMatch*)iter->Next())!=NULL)
{
    if(pMetaMatch->getSystem()==-1) continue; \\if there is
        matching with the META hit
    if(!(pMetaMatch->isSplineAccepted())) continue; \\if the
        spline objects exist?. Overlap and tof cluster checking.
    splineInd=pMetaMatch->GetSplineInd(); \\get an index of
    HSplineTrack object in the category
    pSpline=(HSplineTrack*)catSpline->GetObject(splineInd);\\get a
        pointer to the corresponding HSplineTrack object
    if(!pSpline) continue; \\check the pointer
    pSpline->getP(); \\get the momentum
}

```

Bibliography

- [1] K.N. Mukhin. *Experimental Nuclear Physics*. Moscow, 1993. In Russian. v, 3, 4, 77
- [2] L.G. Landsberg. Electromagnetic decays of light mesons. *Phys. Rep.*, 128,6:301–376, 1985. v, 4, 8, 9, 10, 108
- [3] R.P. Feynman. *Photon-Hadron Interactions*. W. A. Benjamin, Inc., 1972. 4, 6
- [4] J.J Sakurai. *Currents and Mesons*. THE UNIVERSITY OF CHICAGO PRESS, 1972. 4
- [5] Peter Koch. Low mass lepton pair production and pion dynamics in ultrarelativistic heavy ion collisions. *Z. Phys.*, C57:283–304, 1993. 6
- [6] C. Ernst, S. A. Bass, M. Belkacem, Horst Stoecker, and W. Greiner. Intermediate mass excess of dilepton production in heavy ion collisions at BEVALAC energies. *Phys. Rev.*, C58:447–456, 1998. 7, 108
- [7] M. R. Jane et al. *Phys. Lett.*, 59B:103, 1975. 9
- [8] H. Calen et al. Higher partial waves in $pp \rightarrow pp\eta$ near threshold. *Phys. Lett.*, B458:190–196, 1999. 10
- [9] M. Abdel-Bary et al. Measurement of the η production in proton proton collisions with the COSY time of flight spectrometer. *Eur. Phys. J.*, A16:127–137, 2003. 10
- [10] F. Balestra et al. Exclusive η production in proton-proton reactions. *Phys. Rev.*, C69:064003, 2004. 11, 81
- [11] I.Froelich. Hades internal report. 11, 81
- [12] D. Miśkowiec for the CERES collaboration. Recent results from CERES. *Quark Matter, Budapest*, 2005. 11
- [13] R. J. Porter et al. Dielectron cross section measurements in nucleus nucleus reactions at 1.0-A-GeV. *Phys. Rev. Lett.*, 79:1229–1232, 1997. 11, 14

- [14] J. Stroth for the HADES collaboration. Dielectrons as probes for the in-medium structure of hadrons. *DPG 2004, Koln*, Vortrag 2004. 11
- [15] P.Salabura for the HADES collaboration. Probing of in-medium hadron structure with HADES. *Nucl. Phys.*, A749:150–159, 2005. 11
- [16] R. Holzmann for the HADES collaboration. Di-electron mass spectrum in $^{12}\text{C}+^{12}\text{C}$ collisions at 2 AGeV by HADES. *Quark Matter, Budapest*, 2005. 11
- [17] Hendrik van Hees and Ralf Rapp. Medium modifications of vector mesons and NA60. 2006. 11
- [18] R. Rapp and J. Wambach. Chiral symmetry restoration and dileptons in relativistic heavy-ion collisions. *Adv. Nucl. Phys.*, 25:1, 2000. 11
- [19] Ralf Rapp and Jochen Wambach. Vector mesons in medium and dileptons in heavy-ion collisions. 1999. 11
- [20] J. Wambach and R. Rapp. Theoretical interpretations of low-mass dileptons. *Nucl. Phys.*, A638:171–182, 1998. 11
- [21] Tetsuo Hatsuda and Su Houng Lee. QCD sum rules for vector mesons in nuclear medium. *Phys. Rev.*, C46:34–38, 1992. 11
- [22] HADES collaboration. Proposal for High-Acceptance DiElectron Spectrometer. 1994. 14
- [23] P.Salabura et.al. HADES: High Acceptance DiElectron Spectrometer. *Nucl. Phys. Proc. Suppl*, 44:701–707, 1995. 14
- [24] R. Schicker et. al. Acceptance and resolution simulation studies for the dielectron spectrometer HADES at GSI. *Nucl. Instrum. Meth.*, A380:586–596, 1996. 14
- [25] E. Berdermann et. al. *Nucl. Phys. (Proc. Suppl.)*, B78:533–539, 1999. 15
- [26] P. A. Cherenkov. *Physical Review*, 52:378, 1937. 16
- [27] William R. Leo. *Techniques for Nuclear and Particle Physics Experiments*. Springer Verlag Berlin, 1994. 16
- [28] J. D. Jackson. *Classical Electrodynamics*. John Wiley and Sons, Inc., 1962. 16, 19
- [29] K. Zeitelhack et. al. The HADES RICH detector. *Nucl. Instrum. Meth.*, A433:201–206, 1999. 17

- [30] A. Toia. *Performance of the HADES Spectrometer for Dilepton Identification in the Reaction $C + C$ at 1 – 2 AGeV*. Dissertation, Justus-Liebig-Universität Gießen, 2004. 17
- [31] K. Hagiwara et al. *Physical Review*, D 66, 2002. 19
- [32] W. Blum and L. Rolandi. *Particle Detection with Drift Chambers*. Springer Verlag, CERN; European Organization For Nuclear Research, Geneva, 1993. 19, 20
- [33] H. Bokemeyer et al. Development of low-mass drift chambers for the HADES spectrometer. *Nucl. Instrum. Meth.*, A 477:397–400, 2002. 21
- [34] C. Müntz. The HADES Tracking System. *Nucl. Instrum. Meth.*, A535:242–246, 2004. 21
- [35] GARFIELD 7.02. Simulation of gaseous detectors; <http://www.cern.ch/garfield>; Online User Guide, 2000. 21
- [36] C. Garabatos et al. Optimisation of low-mass drift chambers for HADES. *Nucl. Instrum. Meth.*, A 412:38–46, 1998. 22
- [37] A. Godi et al. The HADES time-of-flight wall. *Nucl. Instrum. Meth.*, A494:14–25, 2002. 24
- [38] A. Balanda et al. The HADES Pre-Shower detector. *Nucl. Instrum. Meth.*, A531:445–458, 2004. 26
- [39] M. Atac, A. V. Tollestrup, and D. Potter. Selfquenching streamers. *Nucl. Instr. Meth.*, 200:345, 1982. 27
- [40] HADES Trigger Homepage in Gießen. <http://pcpig.physik.uni-giessen.de/hades/hades.htm>, 2000. Internetangebot der HADES Kollaboration in Gießen. 28
- [41] G. Agakichiev and V. Pechenov et.al. Fast method for track searching in multilayer drift chambers of the HADES experiment. *Particle and Nuclei, Letters*, 4,1001, 2000. 35
- [42] V. Pechenov, Private communications. 35, 39
- [43] G. Agakichiev, Private communications. 35, 39
- [44] A. Ierusalimov, Private communications. 39
- [45] A. Ierusalimov. Hades internal report. 2002. 39

- [46] I.A. Golutvin et.al. Optimal choice of track fitting procedure for contaminated data in high-accuracy cathode strip chambers. *Joint Institute for Nuclear Research, Preprint*. 39
- [47] A. Schmah. Alignment of the HADES spectrometer. *HADES internal report*, 2006. 43
- [48] M. Sánchez-García. *Momentum reconstruction and pion production analysis in the HADES spectrometer at GSI*. Dissertation, Universidade de Santiago de Compostela, 2003. 48, 49
- [49] Philip R. Bevington and D. Keith Robinson. *Data Reduction and Error Analysis*. McGraw-Hill, 2003. 51
- [50] H.Wind. Momentum analysis by using a quintic spline model for the track. *Nucl.Instrum.Meth.*, 115:431–434, 1974. 51
- [51] K. Kurek et al. An algorithm for track reconstruction in the large angle spectrometer of the COMPASS experiment. *Nucl. Instrum. Meth.*, A485:720–738, 2002. 51
- [52] R.K. Bock et.al. *Data Analysis Techniques for High-Energy Physics Experiments*. CAMBRIDGE UNIVERSITY PRESS, 2003. 51
- [53] N.S. Bakhvalov et.al. *Numerical Methods*. MIR, 2000. In Russian. 56
- [54] F. Halzen and Alan D. Martin. *Quarks and Leptons*. John Wiley and Sons, Inc., 1984. 75
- [55] H.Perkins. *Introduction to high energy physics*. Addison-Wesley Company, 1987. 75
- [56] L.F. Li T.P Cheng. *Gauge theory of elementary particle physics*. Oxford University Press, 1991. 75, 76
- [57] M.I Petrashen and E.D Trifonov. *Application of group theory to the quantum mechanics*. Moscow, 2002. In Russian. 75
- [58] Frederick J. Gilman and Russel Kauffman. The η η' mixing angle. *Phys. Rev.*, D36:2761, 1987. 77
- [59] A. Bramon, R. Escribano, and M. D. Scadron. The η η' mixing angle revisited. *Eur. Phys. J.*, C7:271–278, 1999. 77
- [60] M. Bardadin-Otwinowska et al. Six-prong interactions of π^+ mesons with protons at 8 gev/c. *Phys. Rev.*, D4:2711–2739, 1971. 77

- [61] A. Rustamov for the HADES coll. Meson production in pp collisions. *XLIV International Winter Meeting on Nuclear Physics, BORMIO, ITALY, 2006*. 77
- [62] C. Caso and A. Gurtu. The Z boson: in review of particle physics (rpp 1998). *Eur. Phys. J.*, C3:227–231, 1998. 79
- [63] E. Gedalin, A. Moalem, and L. Razdolskaja. A covariant OBE model for eta production in NN collisions. *Nucl. Phys.*, A634:368–392, 1998. 79
- [64] K. Nakayama, J. Speth, and T. S. H. Lee. η meson production in NN collisions. *Phys. Rev.*, C65:045210, 2002. 79
- [65] M. T. Pena, H. Garcilazo, and D. O. Riska. The reaction $pp \rightarrow pp\eta$ and the η nucleon and nucleon nucleon interactions. *Nucl. Phys.*, A683:322–338, 2001. 79
- [66] V. Baru et al. Production of η mesons in nucleon nucleon collisions. *Phys. Rev.*, C67:024002, 2003. 79
- [67] J. F. Germond and C. Wilkin. The $pp \rightarrow pp\eta$ reaction near threshold. *Nucl. Phys.*, A518:308–316, 1990. 80
- [68] Goran Faldt and Colin Wilkin. The production of η mesons in nucleon nucleon collisions near threshold. *Phys. Scripta*, 64:427–438, 2001. 80
- [69] K. Nakayama. Pseudoscalar and vector meson production in NN collisions. 2001. 80
- [70] M. A. Kagarlis. Pluto++. *GSI Report*, 2000-2003. 80
- [71] PLUTO. Pluto++, A Monte Carlo simulation tool for hadronic physics; <http://www-hades.gsi.de/>;, 2004. 80
- [72] HGEANT. HADES Simulation Package; <http://www-hades.gsi.de/>;, 2004. 80, 81
- [73] GEANT. Detector Description and Simulation Tool; <http://consult.cern.ch/writeup/geant/>; Online User Guide, 2004. 81
- [74] G.I. Kopilov. *Basics of Resonance Kinematics*. NAUKA, 1970. in Russian. 82
- [75] V.I. Moroz. Kinematic fit. *Preprint JINR, Dubna*, 1968. 94
- [76] S. Eidelman et al. *Phys. Lett.*, B 592(1), 2004. 110, 121
- [77] J. Markert. *Untersuchung zum Ansprechverhalten der Vieldraht-Driftkammern niedriger Massenbelegung des HADES Experimentes*. Dissertation, Fachbereich Physik der Johann Wolfgang Goethe-Universität der Johann Wolfgang Goethe-Universität, 2005. 135

Acknowledgments

I would like to thank:

- My supervisor, Prof. Dr. Peter Braun-Munzinger for inviting me to the HADES collaboration, for useful discussions, and for encouraging me in pursuing the goal.
- Dr. Ingo Froelich, Dr. Piotr Salabura, Prof. Dr. Joachim Stroth for a nice and useful discussions, "fresh" ideas during my data analysis.
- Prof. Dr. Herbert Ströbele, Dr. Jens Söeren Lang, Prof. Dr. Volker Metag.
- Dr. Heydar Agakishiyev, Mr. Alexander Ierusalimov and Dr. V. Pechenov for a help and discussions concerning both a technical and physics part, for a discussion about deep "secrets" of the HADES tracking.
- Dr. Romain Holzmann, for a lot of discussions about physics, software framework, "secrets" of Geant, and so on. I thank him also for reading first complete version of this thesis, and making valuable remarks.
- Dr. Christian Sturm for reading some parts of this thesis and making nice remarks.
- My roommates: Alexander Schmah, Dr. Jochen Markert, Yvonne Pachmayer, Khaled Teilab, Dr. Jörn Wüstenfeld and Dr. Peter Zumbruch for nice working atmosphere. I thank them also for their help especially with the German language.
- Tetyana Galatyuk, Dr. Burkhard Kolb, Dr Wolfgang König, Dr. Ilse König, Simon Lang, Dr. Christian Müntz, Dr. Jerzy Pietraszko, Dr. Mateusz Ploskon, Malgorzata Sudol for their help and friendship.
- Dr. Mohammad Al-Turany, Dr. Denis Bertini and A. Manafov for a nice discussions concerning especially software.
- My parents for they care and a lot of help

- My wife, without her help it would be impossible to finish this work, at least in time. I also thank our 1 year old daughter, in spite of the fact that she several times destroyed parts of this thesis, computer and my books. Of course all this brought only beauty to that parts.

Resume

Name: Anar Rustamov

Date of Birth: April 16, 1977 Shamakhi, Azerbaijan

Address: Gesellschaft für Schwerionenforschung mbH Planckstrasse 1 D-64291, Darmstadt, Germany

Tel: +49 6159 711303

Email: A.Rustamov@gsi.de

Education :

1983-1994 School

1994-1998 Baku State University, Physics Department, Bachelor degree

1998-2000 Baku State University, Physics Department, Master degree

2000-2002 Scientific researcher, Joint Institute for Nuclear Research, Laboratory of Particle Physics, Moscow region, Dubna

2002-2003 Guest Scientist, Gesellschaft für Schwerionenforschung mbH, Darmstadt, Germany

2003-2006 Technical University of Darmstadt Ph.D in Physics supervised by Prof. Dr. Peter Braun-Munzinger